REPUBLIC OF TURKEY
YILDIZ TECHNICAL UNIVERSITY
GRADUATE SCHOOL OF SCIENCE AND ENGINEERING

PARAMETER ESTIMATION OF LFM SIGNALS USING THE FRACTIONAL FOURIER TRANSFORM

Omair ALDIMASHKI

DOCTOR OF PHILOSOPHY THESIS
Electronics and Communications Engineering Department
Program of Telecommunication Engineering

Supervisor
Assoc. Prof. Dr. Ahmet Serbes

August, 2023

REPUBLIC OF TURKEY
YILDIZ TECHNICAL UNIVERSITY
GRADUATE SCHOOL OF SCIENCE AND ENGINEERING

PARAMETER ESTIMATION OF LFM SIGNALS USING THE FRACTIONAL FOURIER TRANSFORM

A thesis submitted by Omair ALDIMASHKI in partial fulfillment of the requirements for the degree of **DOCTOR OF PHILOSOPHY** is approved by the committee on 22.08.2023 in Electronics and Communications Engineering Department , Program of Telecommunication Engineering.

Assoc. Prof. Dr. Ahmet Serbes
Yildiz Technical University
Supervisor

Approved By the Examining Committee

Assoc. Prof. Dr. Ahmet Serbes, Supervisor
Yildiz Technical University _____

Prof. Dr. Lutfiye Durak Ata, Member
Istanbul Technical University _____

Prof. Dr. Tansal Güçlüoğlu, Member
Yildiz Technical University _____

Prof. Dr. HACI İLHAN, Member
Yildiz Technical University _____

Assoc. Prof. Dr. ERDOĞAN AYDIN , Member
Istanbul Medeniyet University _____

I hereby declare that I have obtained the required legal permissions during data collection and exploitation procedures, that I have made the in-text citations and cited the references properly, that I haven't falsified and/or fabricated research data and results of the study and that I have abided by the principles of the scientific research and ethics during my Thesis Study under the title of Parameter Estimation of LFM Signals Using the Fractional Fourier Transform supervised by my supervisor, Assoc. Prof. Dr. Ahmet Serbes. In the case of a discovery of false statement, I am to acknowledge any legal consequence.

Omair ALDIMASHKI

Signature

Dedicated to my parent
and my wife

ACKNOWLEDGEMENTS

I would like to take this opportunity to express my sincere gratitude and appreciation to several people who have contributed significantly to my academic and personal development throughout my university journey. First and foremost, I extend my heartfelt thanks to my advisor, Prof. Dr. Ahmet Serbes, for his exceptional guidance, support, and encouragement throughout the research work leading up to this thesis. His vast knowledge and expertise have been instrumental in shaping my skills and understanding of the subject matter. I am deeply grateful for his invaluable contributions to my education and professional growth.

In addition, I would like to express my gratitude to my parents, whose unwavering support and encouragement have been a constant source of motivation for me. Their love, care, and sacrifices have made it possible for me to pursue my academic goals and dreams. I owe them an immeasurable debt of gratitude for their unending supportiveness.

I would like to extend my thanks to everyone who has contributed in any way to my academic and personal growth. It is through their collective efforts and support that I have achieved this milestone in my academic journey.

Omair ALDIMASHKI

TABLE OF CONTENTS

LIST OF SYMBOLS

A	Amplitude
m	Chirp rate
f_0	Initial frequency
s(t)	Mono chirp signal
$s_k(t)$	k-component chirp signal
α	Rotation angle
t	Time variable
T	Signal length
N	Signal samples
u	Fractional frequency
T_s	Sampling frequency
Ω	Model

LIST OF ABBREVIATIONS

AME	Aboutanios and Mulgrew estimator
AWGN	Additive White Gaussian Noise
AF	Ambiguity function
CS	Compressed sensing
CRLB	Cramer-Rao lower bound
CPF	Cubic phase function
FT	Fourier transform
FrFT	Fractional Fourier Transform
GSS	Golden section search
HAQSE	High-Accuracy Quadratic Sine Estimator
HAF	High-order ambiguity function
IID	Independent identically distributed
ICPF	Integrated cubic phase function
LM	Levenberg-Marquardt
LFM	Linear Frequency Modulated
MLE	Maximum Likelihood Estimator
MSE	Mean squared error
MAP	method of alternating projections
MVUE	Minimum variance unbiased estimator
PCFCRD	parameterized centroid frequency-chirp rate distribution
PFM	peak FrFT magnitude
PHAF	Product high-order ambiguity function
RWT	Radon-Wigner transform

STFT	Short-Time Fourier Transform
SNR	Signal-to-Noise Ratio
TCR	Time chirp-rate representation
TF	Time-frequency
TFR	Time-Frequency Representation
WHT	Wigner-Hough transform
WVD	Wigner-Ville distribution

LIST OF FIGURES

LIST OF TABLES

ABSTRACT

Parameter Estimation of LFM Signals Using the Fractional Fourier Transform

Omair ALDIMASHKI

Electronics and Communications Engineering Department
Doctor of Philosophy Thesis

Supervisor: Assoc. Prof. Dr. Ahmet Serbes

Linear frequency modulated (LFM) signals are the type of signal that are commonly encountered in many areas, including telecommunications, radar, sonar, and medical imaging. These signals are characterized by their changing frequency over time, with the frequency increasing or decreasing linearly over time. Since the parameters of LFM signals can carry useful information that can be used in many applications, such as detecting objects or measuring distances, accurately estimating these parameters is important.

However, estimating the parameters of LFM signals can be challenging, especially in the presence of noise. Many studies have focused on developing techniques that can estimate LFM signal parameters accurately under noisy conditions. Despite the efforts of researchers, the current algorithms for LFM parameter estimation suffer from some drawbacks, such as poor performance with multi-component LFM signals or high computational complexity.

Therefore, there is a significant need for a reliable alternative that can accurately and efficiently estimate the parameters of LFM signals for both mono-component and multi-component cases, in the presence of noise. The main objective of our research is to address this need by developing algorithms that utilizes the fractional Fourier transform to estimate the LFM signal parameters. The proposed algorithms aim to provide a fast and accurate estimation of LFM parameters, with the ability to handle noisy environments and multi-component signals.

Keywords: Chirp signals, fractional Fourier transform, LFM parameter estimation, chirp rate.

ÖZET

Kesirli Fourier Dönüşümü Kullanılarak DFM İşaretlerinin Parametre Tahmini

Omair ALDIMASHKI

Elektronik ve Haberleşme Mühendisliği Bölümü
Doktora Tezi

Danışman: Assoc. Prof. Dr. Ahmet Serbes

Doğrusal frekans modülasyonlu (DFM) işaretler, telekomünikasyon, radar, sonar ve tıbbi görüntüleme gibi birçok alanda yaygın olarak karşılaşılan işaret türleridir. Bu işaretler, frekanslarının zaman ile değişmesi ile karakterize edilirler ve zamanla doğrusal olarak artan veya azalan frekansa sahiptirler. DFM işaretlerinin parametreleri, nesnelerin tespiti veya mesafelerin ölçülmesi gibi birçok uygulamada kullanılabilecek faydalı bilgiler taşıdığından, bu parametrelerin doğru bir şekilde tahmin edilmesi önemlidir.

Ancak, DFM işaretlerinin parametrelerini ölçmek, özellikle gürültülü ortamlarda, zorlu olabilir. Birçok çalışma, gürültülü koşullar altında DFM parametrelerini doğru bir şekilde tahmin edebilecek teknikler geliştirmeye odaklanmıştır. Ancak, araştırmacıların çabalarına rağmen, DFM parametre tahmininde kullanılan mevcut algoritmalar bazı dezavantajlara sahiptir . Örneğin, çok bileşenli DFM işaretlerinde kötü performans veya yüksek hesaplama karmaşıklığı gibi.

Bu nedenle, gürültülü ortamlarda tekli ve çoklu bileşen durumlarında DFM işaret parametrelerini doğru ve verimli bir şekilde tahmin edebilecek güvenilir bir alternatif önemli bir ihtiyaçtır. Çalışmamızın temel amacı, DFM işaret parametrelerini tahmin etmek için kesirli Fourier dönüşümünden yararlanan algoritmalar geliştirerek bu ihtiyacı karşılamaktır. Önerilen algoritmalar, gürültülü ortamları ve çok bileşenli işaretleri ele alabilen hızlı ve doğru bir DFM parametre tahmini sağlamayı amaçlamaktadır.

Anahtar Kelimeler: Doğrusal frekans modülasyonlu işaretler, Kesirli Fourier Dönüşümü, DFM İşaretlerinin Parametre Tahmini, chirp oranı.

1
Introduction

1.1 The Significance of the Problem

The LFM signals hold great significance in diverse fields and applications due to its robustness against interference, its role in radar and communication systems, its range resolution capabilities in imaging, and its versatility in signal processing and spectral analysis. The LFM signal's unique characteristics, including its ability to distinguish desired signals from interference, make it valuable for target detection, localization, and tracking in radar applications. In communication systems, the LFM signal enables efficient utilization of bandwidth, resistance to narrowband interference, and improved signal privacy and security. Its range resolution capabilities are beneficial in medical ultrasound imaging and remote sensing, offering precise measurements and high-quality imaging. Additionally, the LFM signal finds applications in signal processing and spectral analysis, facilitating tasks such as modulation classification, target recognition, and signal separation. Therefore, we can say that the LFM signal's robustness, versatility, and unique properties make it an essential tool in various domains, enhancing performance, reliability, and accuracy in numerous applications. The estimation of LFM parameters also holds significant importance in various fields and applications. In radar and sonar systems, LFM parameter estimation is vital for target detection, localization, and tracking. By accurately estimating the parameters, such as the carrier frequency and chirp rate, the range, velocity, and direction of moving targets can be determined with high precision. This information is essential for applications ranging from air traffic control and maritime navigation to object recognition and surveillance. LFM parameter estimation is also crucial in communication systems, especially in frequency-modulated continuous wave radar and spread spectrum communication. Estimating the LFM parameters allows for efficient signal demodulation, synchronization, and interference mitigation. It enables reliable data transmission and reception, leading to improved communication performance and higher data rates. Furthermore, in medical imaging and remote sensing, accurate LFM parameter estimation plays a vital role. In medical ultrasound

imaging, for example, estimating the parameters of LFM pulses helps enhance the quality of image reconstruction and improves the visualization of anatomical structures. In remote sensing applications, LFM parameter estimation aids in the analysis of radar and lidar signals, enabling precise mapping, target identification, and environmental monitoring. Moreover, LFM parameter estimation has applications in signal processing, spectrum analysis, and signal classification. It provides insights into signal modulation characteristics, facilitates signal separation and denoising, and assists in identifying different types of signals within a complex environment. Therefore, it is important to develop algorithms that can estimate the LFM parameters quickly and accurately. Several algorithms have been developed to estimate the parameters of LFM signals, and these algorithms are distinguished from each other based on the following factors.

- Noise immunity: Since practical applications involve noisy environments, the ability of an estimator to provide accurate results even in the presence of high levels of noise is an important advantage. Estimators with a smaller signal-to-noise ratio (SNR) breakdown threshold are considered better.
- Multi-component LFM signals: While many estimators work well with mono-component LFM signals, their performance significantly deteriorates in the case of multi-component LFM signals. It is also important to assess an estimator's ability to distinguish between closely separated components and to determine the threshold beyond which the estimator fails to distinguish between two closely spaced components. Estimators with a smaller threshold are considered better.
- Computational efficiency: In radar systems, particularly in military radar, the received signal length can be large, so the estimator should aim to minimize the computations required to process these signals to reduce the processing time.
- Accuracy: Accuracy is one of the most important features of the estimator, as failure to provide accurate results can lead to major problems, particularly in military applications. Accuracy is measured by calculating the mean squared error (MSE) of the parameters and then comparing it to theoretical Cramer-Rao lower bound (CRLB). Estimators that yield an MSE closer to the CRLB are considered better.

Estimators used for LFM signal parameter estimation differ from each other based on various criteria. Among these estimators, the maximum likelihood estimator (MLE) is the statistically ideal estimator that achieves the CRLB. However, the MLE

is computationally inefficient since it requires searching across multiple dimensions, making it practically useless for large signal lengths. On the other hand, product high-order ambiguity function (PHAF) is an example of a computationally efficient estimator. But its performance is incomparable to that of the MLE.

As a result, there is a clear need to develop an estimation algorithm that can fulfill the aforementioned criteria while being practical for real-world applications. In this section, we will provide a detailed review of the most important LFM parameter estimation algorithms. We will evaluate their advantages and disadvantages based on the criteria mentioned earlier. However, it is crucial to provide an overview of estimation theory and explain its key concepts beforehand.

1.2 Introduction to Estimation Theory

1.2.1 Motivation

Estimation theory is a branch of statistics that focuses on inferring unknown parameters or quantities from data that we observe or measure. The goal is to use statistical methods to estimate the values of these unknown parameters with a certain level of confidence and to quantify the uncertainty associated with these estimates. There are three important concepts in estimation theory. The first concept involves studying the estimation algorithms, which are mathematical methods used to infer unknown variables based on a given set of data. Estimation algorithms can take into account uncertainties in the data and other sources of information to produce estimates that are as accurate as possible. The second concept in estimation theory involves methods for assessing the goodness of these estimation algorithms. This includes evaluating the accuracy and precision of the estimates, as well as assessing the bias and variance of the estimation algorithms. Finally, estimation theory provides methods for making confidence statements about the estimated parameters. Confidence statements involve defining a region or interval around the estimated value, which is expected to contain the true value of the parameter with a certain level of confidence. Overall, estimation theory provides a systematic approach to inferring unknown parameters from data. By taking into account the uncertainties in the data and other sources of information, estimation theory enables us to produce accurate and reliable estimates of these parameters and to quantify the uncertainty associated with these estimates [1].

1.2.2 Estimation Theory Components

According to [2, 3], any estimation process should consist of the following elements:

- **Known information set.** This refers to any information that is known about the parameters or the process being estimated. It can include data, as well as any other prior information that is available. The known information set serves as the foundation for the estimation process and is essential for producing accurate estimates.

- **Estimator.** The estimator is the mathematical method used to calculate the estimated parameters based on the known information set, the model, and the objective function. The goal of the estimator is to produce estimates that are as accurate and reliable as possible.

- **Objective function**. The objective function is used as a guide to help the estimator find the correct parameter values as closely as possible. It specifies the goals that the estimator needs to achieve and serves as an optimizer to search for the optimal solution in the parameter space. The objective function can take the form of a distance measure or a loss function that needs to be minimized.

- **Model or Constraints**. The model or constraints define the relationship between the known information set and the unknown parameter space. It can take the form of an equation, a probability density function, or an approximation, and may also include constraints such as bounds or ranges. The model serves as a bridge between the knowns (i.e., the data) and the unknowns (i.e., the parameters).

- **Interval Estimation**. Interval estimation involves constructing a confidence interval around the point estimate. The confidence interval provides a range of values within which the population parameter is expected to lie with a certain level of confidence. Interval estimation is important for quantifying the uncertainty associated with the estimated parameters and provides a measure of the reliability of the estimation process.

By incorporating these elements into the estimation process, it is possible to produce accurate and reliable estimates of the parameters or quantities of interest, while also quantifying the uncertainty associated with these estimates. Estimators can have various characteristics such as implementation, ease of analysis, robustness, consistency, and efficiency. However, in estimation theory, it is not feasible to find an estimator that is efficient, consistent, robust, easy to implement, and provides an optimal estimate all at the same time. Thus, there is always a trade-off among these properties. The primary objective of an estimator is to ensure that the estimated values are as close as possible to the correct value. The minimum variance unbiased estimator

(MVUE) guarantees achieving this objective, which will be discussed in more detail later. Therefore, the MVUE is the desired property for an estimator to have.

1.2.3 Estimator Properties

There are certain properties that allow us to evaluate the performance of any estimator, and these properties can be classified into two groups [4].

1.2.3.1 Statistical properties.

These properties are used to examine how the estimator responds to changes in data, and the most important properties are as follows:

- **Bias.** The property of bias measures the average accuracy of the estimator. It can be calculated by taking the difference between the true value of the parameter to be estimated and the expected value of the estimate. For example, when estimating the chirp rate parameter ,m, the bias can be mathematically expressed as follows.

$$Bias = |m - E\{\widehat{m}\}|. \tag{1.1}$$

- **Variance.** This property measures the extent of variation of the estimator when the data changes. For instance, in the estimation of the chirp rate parameter, the variance can be expressed mathematically as follows.

$$var\{\widehat{m}\} = E\{(\widehat{m} - E\{\widehat{m}\})^2\}. \tag{1.2}$$

- **Efficiency.** Efficiency is a measure that indicates the estimator's ability to decrease the data's uncertainty without transforming it into the estimates. The most efficient estimator is the one that can minimize the uncertainty or variability to the greatest extent. In other words, efficiency shows the distance between the variance of the estimator and the minimum variance estimator, which is the most efficient estimator. Mathematically, for the case of chirp rate estimation, efficiency can be expressed as follows.

$$Efficiency(\widehat{m}) = \frac{var\{\widehat{m}\}_{MVUE}}{var\{\widehat{m}\}}. \tag{1.3}$$

  Where, $var\{\widehat{m}\}_{MVUE}$ is the lowest achievable variance among all the estimators.

- **Consistency**. Consistency refers to the property of an estimator that it converges to the true value of the parameter as the sample size increases. An estimator

is said to be consistent if it converges in probability to the true value of the parameter as the sample size increases.

- **Mean square error.** Measures how variable the estimator is when changing the data but this time with respect to the correct value. Mathematically it can be expressed be

$$MSE\{\widehat{m}\} = E\{(\widehat{m} - m\})^2\}. \tag{1.4}$$

1.2.3.2 Asymptotic properties.

These properties investigate how the estimator responds to changes in sample size. As the sample size increases, it is important to evaluate the statistical properties of the estimator and the quality of the estimate to determine if they are improving or not. The ideal estimator is one that demonstrates better performance and statistical properties as the sample size increases. Another crucial property in asymptotic analysis is consistency, which examines how the estimator converges to the correct value of the parameter. There are three topics in convergence: the convergence level, which determines how close the estimated value is to the correct value; the convergence rate, which determines how quickly the estimator converges to the correct value; and the conditions that ensure convergence, if any.

1.2.4 The Ideal or Optimal Estimator

The ideal estimator, also known as the optimal estimator or the most efficient estimator, or the MVUE, is characterized by two important properties, as described in [3]:

- The estimator should be unbiased, which means that the estimator produces correct estimates on average. Mathematically, for the case of the chirp rate estimation problem, this can be expressed as follows:

$$E\{\widehat{m}\} = m, \tag{1.5}$$

then, The chirp rate estimator is considered unbiased if the expected value of the estimates equals the correct value of m. It is worth noting that $\widehat{m}$ is a random variable, hence, m cannot be compared to $\widehat{m}$ directly but rather to its expected value. Unbiasedness is a measure of proximity, and thus, it is related to accuracy. Even if the aforementioned condition is satisfied, the estimator is not necessarily ideal. This is because if the data record is changed, the estimated value will also

change. However, it should not change significantly. This leads us to the second condition.

- The second condition is to have the least variability or the minimum variance. While the estimator uses the information set to produce an estimate for the parameter, it also lets the uncertainty of the data propagate to the estimates. Therefore, we want the estimator to reduce that uncertainty. When the data change from one experiment to another, the estimate will also change, but we do not want it to change in the same way as the data changes. To achieve the least variability, we need the variance of the estimate to be as minimum as possible. This second condition is a measure of precision, and the minimum variance estimator is the highest precision estimator.

1.3 Literature Review

In our literature review, we have meticulously structured our analysis into eight distinct sections, each dedicated to exploring and evaluating different aspects of parameter estimation in LFM. This systematic organization enables us to provide a comprehensive understanding of the topic. The first section focuses on statistical estimation methods, where we thoroughly examine various statistical techniques commonly employed for estimating LFM signal parameters. Moving on to the second section, we delve into time-frequency representations, exploring techniques that allow for the simultaneous analysis of signal properties in both the time and frequency domains. Continuing our exploration, the third section investigates integrated time-frequency representations, which involve algorithmic approaches that combine multiple time-frequency representations to enhance the accuracy and reliability of LFM parameter estimation. By leveraging the complementary strengths and mitigating the limitations of individual representations, these algorithms aim to improve overall estimation performance. In the fourth section, we delve into algorithms based on time chirp-rate representations, utilizing variations in chirp rates over time to estimate LFM signal parameters. The fifth section focuses on integrated time chirp-rate representations, aiming to enhance estimation performance and overcome potential limitations through the integration of multiple representations. Moving forward, the sixth section explores frequency chirp rate representations, investigating methods that represent LFM signals in the frequency and chirp rate domain. By analyzing the characteristics in the frequency domain and variations in chirp rate, we strive to extract the desired parameters with improved accuracy. In the seventh section, we delve into compressed sensing-based algorithms. These methods exploit the inherent sparsity or compressibility of LFM signals to achieve efficient and reliable parameter

estimation. By carefully selecting and acquiring a sparse set of measurements, we can effectively reconstruct and estimate the parameters. Lastly, in the eighth section, we explore linear integration-based algorithms. By organizing our literature review into these eight sections, we aim to provide a comprehensive analysis of the diverse approaches and techniques employed in LFM parameter estimation. This systematic exploration allows us to gain insights into the strengths, limitations, and potential areas of improvement for each method, fostering a deeper understanding of the field.

1.3.1 Statistical Estimation Techniques

1.3.1.1 Maximum Likelihood Estimator

The MLE is a powerful algorithm used in the estimation theory to estimate unknown parameters for a probability distribution model. Its objective is to estimate the values of the unknown parameters that make the observed data most likely to have occurred, given the probability distribution model.

In the case of mono-component LFM signals, the MLE is commonly used to estimate the initial frequency and chirp rate. For this purpose, the MLE maximizes a specific function that depends on the observed data and the probability distribution model. By finding the values of the initial frequency and chirp rate that maximize this function, the MLE produces estimates that are statistically optimal [5, 6].

The MLE estimates the parameters of the LFM signal based on both the LFM signal model and the statistical characteristics of the noise. MLE is considered statistically optimal because it has an unbiased mean and achieves the asymptotic CRLB [7, 8]. However, MLE has several drawbacks. First, the MLE is computationally expensive and thus impractical due to the need for a multidimensional search. Second, there are many local minima in the search space and the estimation for the initial parameter must be accurate enough for noisy signals. Otherwise, the algorithm may not converge to the global optimum. Many research studies have aimed to improve the MLE-based algorithms, but these improvements often come at the cost of reduced anti-noise performance or accuracy. In [5], the MLE was employed to estimate the initial frequency and the chirp-rate for LFM signals in two steps: A global search using the grid search method followed by a local search using Newton's algorithm to converge on the optimum values. While this method has reduced the computational cost, selection of the initial parameters significantly impacts its performance. Additionally, this algorithm is not suitable for multi-component LFM signals. In [7], a different MLE-based algorithm was proposed for estimating LFM parameters using global optimization and efficient importance sampling. However, the algorithm still has a high computational cost and the SNR breakdown threshold was as high as 3 dB.

In [9], an ML-based estimator with a lower computational cost has been proposed. However, this algorithm is complex and can only operate in high SNR conditions. Another improved algorithm has been proposed in [10] using a combination of ML and phase-unwrapping. However, the computational load is high. In [11], the CRLB for multi-component LFM signals has been derived. Additionally, an algorithm for estimating chirp rates and initial frequencies has been proposed based on tracking instantaneous frequencies using the global Hankel rank reduction method followed by a least-squares fitting technique. Finally, a Newton search for the MLE was used to estimate the chirp rates and initial frequencies accurately. The computational cost is high, and there is no guarantee of convergence to the global maximum.

1.3.1.2 Least Squares

Chirp parameter estimation based on least squares involves fitting a mathematical model to the observed signal. Specifically, the instantaneous frequency of an LFM signal can be modeled as a linear function of time, with the slope of this line corresponding to the chirp rate. Therefore, by estimating the slope of the line that best fits the observed instantaneous frequency over time, we can estimate the chirp rate. To do this, we can first estimate the instantaneous frequency of the signal using a method such as the Fourier transform (FT). We can then fit a line to these instantaneous frequency estimates using least squares. In other words, we find the slope of the line that minimizes the sum of the squared errors between the observed instantaneous frequency and the values predicted by the line. This slope corresponds to the chirp rate of the LFM signal. It's worth noting that this method is not guaranteed to produce the exact chirp rate, and the accuracy of the estimate can be greatly affected by the noise. However, it can be computationally efficient for estimating the chirp rate, particularly in cases when the SNR is high. In [12, 13], a non-linear least squares estimator was used to estimate the initial frequency and the chirp rate for LFM signals. A sliding window was utilized to reduce the impact of the many local optima on the global optimum. However, this method is limited to mono-component LFM signals.

Another approach was proposed in [14] for mono-component LFM chirp rate and initial frequency estimation, which uses signal reconstructing least-squares technique. However, this algorithm is also not suitable for multi-component LFM signals.

In [15], a sub-optimal estimation algorithm was suggested, which has two phases. In the first phase, a coarse estimation is performed using an initial guess followed by a fine estimation phase using a multistage least squares approach. However, the anti-noise performance of this algorithm is not satisfactory, and it requires a very high *SNR* threshold.

In [16], the Nelder-Mead algorithm was used in a nonlinear least squares algorithm to estimate the parameters of multi-component polynomial phase signals. However, this method incurs a high computational burden and the *SNR* threshold increases as the chirp rate increases.

[17] focuses on extracting the state-space model of the signal and utilizing various versions of the Kalman filter to estimate LFM signal parameters. The proposed methods demonstrate improved performance in estimation. However, it is important to note that the SNR breakdown threshold remains relatively high, and the consideration of the multi-component case is currently not addressed in this study.

1.3.2 Time-Frequency Representations

Time-frequency representation (TFR) is a widely used method for analyzing non-stationary signals such as LFM signals. TFR represents the signal as a function of both time and frequency, enabling more precise analysis of time-varying signals. By combining time and frequency information, TFR displays the presence of each spectral component of a signal at a specific time. In the time-frequency plane, the LFM signal is depicted as a straight line with an angle associated with its chirp rate. There are two primary subcategories of TFR: linear and bilinear.

1.3.2.1 Linear Time-Frequency Representations

The short-time Fourier transform (STFT) [18] and local polynomial Fourier transform [19] are examples of linear time-frequency representations. The STFT is a popular linear method due to its simplicity and its ability to perform well under low SNR conditions with lower computational complexity. However, the trade-off between time and frequency resolution can deteriorate its performance. Many STFT-based methods have attempted to deal with this trade-off at the expense of increasing computational complexity. In [20], three STFT-based representations were used to analyze LFM signals for local estimation of chirp rate and instantaneous frequency of multi-component signals. The first estimator uses the first derivative of the analysis window in the STFT domain. The second and third estimators employ the derivative of the STFT with respect to time and frequency, respectively. However, the main drawback of this approach is the high computational cost. In [21], a combination of STFT and least-square linear fitting based method was proposed. This method enjoys low computational complexity and can work in low SNR conditions. However, it suffers from picket fence effects.

1.3.2.2 Bilinear Time-Frequency Representations

Wigner-Ville distribution (WVD) [22–26] and methods based on the ambiguity function (AF) [27] are examples of the bilinear time-frequency representations that have been used to analyse the LFM signals. WVD is a popular method for time-frequency analysis of non-stationary signals, including LFM signals. The WVD is a bilinear time-frequency representation that provides very high time and frequency resolutions, which is especially useful for analyzing signals with rapidly changing frequencies. In the WVD, the signal is convolved with a time-reversed and time-shifted version of itself to generate a two-dimensional time-frequency representation. The diagonal ridges in the WVD correspond to the instantaneous frequency of the signal at a specific time. For LFM signals, the WVD produces a time-frequency plot that resembles a series of lines, with the slope of each line corresponding to the chirp rate of the LFM signal [28]. Chirp parameter estimation using the WVD involves identifying the slope of each line in the time-frequency plot and using it to estimate the chirp rate. This can be done using a variety of methods, including linear regression or peak detection. However, the WVD has some limitations including its sensitivity to noise and interference, high computational costs and the presence of cross-terms, which can make it difficult to distinguish between different components in the signal. Despite these limitations, the WVD remains a useful tool for analyzing LFM signals and other non-stationary signals. Several algorithms, including smoothed pseudo Wigner-Ville distribution and scaled L-Wigner distribution, have been proposed in the literature to address the issue of cross-terms. However, these methods can lead to a decrease in signal concentration [29, 30]. The AF is a well-known tool for analyzing and characterizing LFM signals. In the context of chirp parameter estimation, the ambiguity function can be used to estimate the instantaneous frequency and the chirp rate of a signal. One approach is to use the 2D cross AF to estimate the instantaneous frequency and chirp rate. The cross AF is computed by taking the cross-correlation between the signal and a set of delayed and Doppler-shifted replicas of itself. The resulting function has peaks that correspond to the time and frequency of the signal components. The instantaneous frequency can be estimated by computing the time derivative of the phase of the cross AF, and the chirp rate can be estimated by computing the frequency derivative of the phase. Another approach is to use the one dimensional cross AF along the time axis to estimate the chirp rate. This method involves computing the autocorrelation of the signal, followed by taking the magnitude square of the FT of the autocorrelation function. The result is a function that shows the degree of similarity between the signal and its delayed versions for different time lags. The position of the maximum of the function corresponds to the delay between the signal and its delayed version, which can be used to estimate the chirp rate. Discrete polynomial phase transform, which is also known as the high-order

AF (HAF), has been suggested to estimate the LFM parameters [31]. The HAF is a higher-order extension of the AF, which can provide more information about the signal compared to the conventional AF. In chirp parameter estimation, HAF has been used to estimate the parameters of polynomial-phase signals, which include chirp signals as a special case. The HAF can provide higher time and frequency resolutions than the conventional AF, which can help to estimate the chirp parameters more accurately. Additionally, HAF can provide more information about the phase characteristics of the signal, which can help to distinguish between different PPS signals. The HAF method involves applying a phase differentiation process to the LFM signal, which results in a complex sinusoid signal. The signal energy is then concentrated in a suitable frequency bin using the FT. Although HAF requires only one dimensional maximization and is relatively straightforward, its accuracy is compromised when dealing with multi-component chirp signals, as the presence of cross-terms can lead to deterioration in the estimation results. A modified version of HAF has been proposed in [32]. However, its performance was not efficient, especially when the amplitudes of different components are close to each other. In order to suppress the effect of cross-terms the PHAF has been used in [33], where the convenient scaling and the high-order multiple transform technique significantly increase the efficiency of the estimation process. The main advantage of PHAF is its ability to suppress cross-terms and improve the accuracy of parameter estimation for multi-component chirp signals. However, this method is biased and sensitive to noise in the signal. Additionally, the accuracy of the PHAF method may be limited in some cases where the signal's amplitude or phase characteristics change rapidly and has the propagation of estimation errors [34]. In order to address these limitations, [35] propose an alternative approach. However, this algorithm suffers from issues such as high computational cost, ambiguity in selecting lag values, low noise immunity, and error propagation effects. To overcome these drawbacks, several HAF-based algorithms have been developed. For example, the multi-delay HAF and its weighted combination have been utilized to estimate the chirp rates of LFM signals. In some recent studies [36–38], a combination of nonlinear least squares and random basis function methods have been applied to HAF-based algorithms for single component LFM parameter estimation, but the multi-component case has yet to be explored. Despite the promising characteristics of the generalized adjustable parameter correlation kernel method [39], such as low complexity and the ability to avoid coupling terms between time and lag, its performance in challenging SNR conditions is not satisfactory. Although TFR-based algorithms are highly capable of analyzing LFM signals, their drawbacks make them unsuitable for real-time applications. In response to this issue, integrated TF techniques have been proposed as a potential solution.

1.3.3 Integrated Time-Frequency Representations

These algorithms were developed to address the limitations of TFR-based methods, including the trade-off between frequency and time resolution, cross-terms in multi-component cases, and reduced performance in high noise environments. A novel algorithm for detecting and estimating parameters of frequency modulated continuous waveforms using the cross Wigner-Hough transform has been proposed in [40], which leverages the properties of cross-terms in WVD. However, the performance of the algorithm is affected by cross-terms. To mitigate cross-terms and improve the performance of low probability of intercept radar signals, an elliptical Gaussian filter has been used in the ambiguity domain with smoothed pseudo WVD in [41]. In [42], a combination of Teager-Huang transform and Hough transform has been utilized to eliminate cross terms in multi-component LFM signals with high time-frequency resolution. However, the performance in low SNR is diminished. Similarly, [43] utilized a combination of Radon transform and Hilbert-Huang transform for the same purpose. In [44], the keystone transformation of the WVD was used for detecting and estimating parameters of LFM signals with high signal energy concentration and almost free of the cross terms. The lag and time variables were separated using the scaling rule of the keystone transformation. However, the main drawbacks of this algorithm are the high computational cost and the propagation of estimation errors. Other integrated time-frequency methods have been used for analyzing LFM signals, including the Wigner-Hough transform (WHT) [25, 45, 46]. However, WHT has a high computational cost and may cause the initial phase to be lost. In [25], periodic WHT has been proposed for detecting and estimating the parameters of LFM continuous waves, but it requires prior information about the unknown parameters and has a very high computation load. Radon-Wigner transform (RWT) [47, 48] has a similar performance to FrFT, but the computational cost of RWT-based algorithms is very high, making them unsuitable for long record lengths. The Radon-ambiguity transform [49] requires a single dimensional search, so it has a lower computational cost. However, it can be used to estimate only the chirp rate. The LPP-Hough transform [50] has also been proposed. Although these algorithms apparently reduce the cross terms, most of them either increase the computational complexity or decrease the performance in noisy environments or have a negative impact on the time and frequency resolution.

1.3.4 Time Chirp Rate Representations

The evolution of chirp rate with respect to time can be described by the time chirp-rate representation (TCR). The first algorithm presented is the cubic phase function (CPF) [51], which is efficient in analyzing LFM signals. However, when dealing with multi-component LFM signals, spurious peaks and cross-terms appear

and the performance is degraded in noisy environments. The second algorithm is the high-resolution time-frequency rate representation [52], which achieves high resolution in both time and frequency domains while suppressing cross-terms, thus improving upon previous methods. This algorithm is suitable for chirp rate estimation with lower computational cost compared to CPF. However, in the case of multi-component signals, cross-terms limit its applicability due to a trade-off between resolution and cross-term suppression.

1.3.5 Integrated Chirp Rate Representations

Several integrated TCR techniques have been proposed to address the issues mentioned above. These include the integrated CPF (ICPF), the product CPF, and the coherent ICPF [53–55]. However, these methods have not completely eliminated the effects of cross-terms and their performance is degraded in low SNR environments.

1.3.6 Frequency Chirp Rate Representations

The frequency-chirp-rate representation is a method to represent the LFM signal in the frequency and chirp rate domain. Some examples of this representation include LVs distribution [56–58], and the parameterized centroid frequency-chirp rate distribution (PCFCRD). The LV's distribution algorithm is well-known for its high estimation performance and lack of cross-term problems in radar signal processing [56, 57]. However, it has limited frequency and chirp rate ranges, and its performance is significantly affected in the low SNR region. An improved version of LVs distribution was proposed in [59] to reduce the computational cost and improve the anti-noise performance. PCFCRD has been proposed for multi-component LFM signal analysis [60], and it achieves a higher estimation performance by eliminating the cross terms. However, its main drawback is its excessive computational cost.

1.3.7 Compressed Sensing

Compressed sensing (CS) is a novel signal processing framework that has been applied in MRI and radar imaging systems. This framework allows the reconstruction of sparse images or signals at a sub-Nyquist sampling rate provided certain conditions are met, such as sparsity and incoherency. In cases where sampling at the Nyquist rate is unattainable due to some limitations such as limited capabilities, bandwidth, resolution, or cost, CS can be a viable alternative. Unlike the Nyquist framework, which employs $sinc$ interpolation to recover the signal, CS reconstructs the signal from sub-Nyquist samples using iterative or optimization-based algorithms that have a higher computational cost.

The CS approach can be applied to various areas, such as estimation, detection, filtering, and classification. LFM signals with their large bandwidth and high-frequency sampling rate requirements are ideal examples to adopt the CS framework. Furthermore, LFM signals are sparse in its optimum FrFT domain.

Several algorithms for the parameter estimation of LFM signals based on CS have been proposed. The key to these algorithms is designing the measurement matrix, and then the estimation algorithm estimates the parameters by finding the best matching elements or atoms in the matrix. However, having more elements in the measurement matrix results in higher computational cost, even though it leads to better estimation accuracy [61–63]. In [64], an FrFT-based algorithm was proposed to estimate LFM signal parameters using CS, but it has a high computational cost.

The sparse signal representation has also been used in LFM parameter estimation problems [65, 66]. [66], after decomposing the chirp signal into Gabor atoms using the matching pursuit algorithm, the estimation is done directly using the Hough transform. However, the high computational cost is a significant drawback.

1.3.8 Linear Integration

The concept of brute-force searching is the common thing between the algorithms which belong to this category. Discrete chirp Fourier transform has been used in the detection and chirp rate estimation for LFM signals [67]. However, there are restrictions which limit this algorithm. The chirp rates should be integer and the number of samples should be prime. The FrFT based algorithms come here but we will explain about the FrFT properties and the estimation algorithms in a separate chapter.

1.4 Objectives and Contributions of the Thesis

The introduction highlights that in practical scenarios, it is difficult to achieve the optimal characteristics of the LFM parameter estimator due to various factors such as computational cost, noise immunity, and multi-component case challenges. Therefore, the primary objective of this thesis is to find a suitable compromise that can approach the optimal estimator as closely as possible. To accomplish this, the thesis aims to identify a powerful transform that can serve as the foundation of the solution. Since the FrFT is a natural environment for LFM signals, it is the most suitable choice for this purpose. Based on this premise, the main contributions of this thesis can be summarized as follows.

- We prove that the FrFT is an optimum domain for the problem of LFM signal

parameter estimation. We theoretically show that FrFT-based LFM parameter estimation can achieve the CRLB. The mathematical proof and perturbation analysis also provide valuable insights in the field of LFM parameter estimation. The theoretical formulations derived for continuous and discrete cases provide the asymptotic statistical characteristics (mean and variance) of the FrFT-based estimator, which we show to yield optimum results for chirp parameter estimation.

- We show that the FrFT-based chirp-rate estimator performance depends only on the actual chirp-rate and SNR, rather than the initial frequency. This allows for the estimation of chirp-rate in a simplified one-dimensional search space, which significantly reduces computational cost. Moreover, the derivations provide an insight to the threshold of signal time duration breakdown required for the mean and variance to be considered asymptotically efficient.

- We propose a new algorithm for estimating chirp rates for both mono and multi-component LFM signals. The algorithm is based on the FrFT and the golden section search algorithm and is faster and more accurate than previous search-based methods, even in noisy environments. The GSS algorithm is used to find the peak magnitude square of the FrFT domains, which allows for more accurate and efficient parameter estimation. Computer simulations demonstrate that the proposed method outperforms existing methods while incurring lower computing costs. Additionally, the optimum number of iterations required by the GSS to achieve CRLB is derived, and the initial version of the estimation algorithm has been extended to the multi-component case, showing superior performance with the lowest computational cost among similar algorithms.

- We perform a comprehensive analysis, including mathematical derivations, to establish approximate models for the peak FrFT magnitude (PFM) of both mono and multi-component LFM signals in noiseless and noisy environments. The statistical properties of the PFM were examined, revealing that under specific conditions, the statistics converge to an unbiased mean and zero variance asymptotically. This allows the expected value of the PFM to serve as a reliable approximation in the presence of noise.

- We propose a new algorithm for estimating the chirp-rates of noisy multi-component LFM signals based on our proposed models for PFM. We introduce a two-step process that begins with coarse estimates of the chirp-rates for each component. This is achieved by utilizing derived models specifically designed for this purpose. By leveraging these models, we are able to improve estimation accuracy compared to existing blind search algorithms.

Furthermore, our algorithm maintains computational efficiency, making it suitable for real-world applications. In the second step of our algorithm, we employ an estimate-and-subtract strategy to further refine the initial coarse estimates. Instead of directly removing components from the LFM signal, we utilize the derived model to identify and eliminate peaks in the PFM. This unique approach allows us to better distinguish between closely separated components and effectively eliminate error propagation and bias effects. By selectively removing the peaks while preserving the original signal, we achieve more accurate chirp-rate estimation. We evaluate our algorithm through simulations and compare it with other state-of-the-art methods. The results show that our algorithm achieves nearly the CRLB, has no error propagation, requires acceptable computational cost, has a lower SNR breakdown threshold, performs better in estimating closely spaced components, handles components with unequal powers, and eliminates the shading effect between components. Therefore, our algorithm outperforms other state-of-the-art algorithms without additional computational cost.

- Next, we propose a nonlinear least squares algorithm based on the Levenberg-Marquardt method to estimate the chirp rates of multi-component LFM signals. The algorithm uses an optimal α step size to ensure accurate modeling and detect all nearby components. The algorithm is able to accurately estimate chirp rates under very low SNR and solves the picket fence effect. The algorithm adopts the Levenberg-Marquardt curve fitting concept and uses our proposed analytical model as the model function. The algorithm works efficiently with acceptable computational cost and avoids the propagation of error problem introduced in other chirp rate estimation algorithms.

2
LFM Parameters Estimation Using The Fractional Fourier Transform Domains

2.1 Linear Frequency Modulated Signals

2.1.1 Introduction

LFM signals, also called chirp signals or second-order polynomial phase signals, have a continuously varying instantaneous frequency over time. Within a defined time interval, the linear chirp signal linearly sweeps frequencies. In some literature, chirp signals are referred to as Doppler signals because echoes from moving targets can be modeled as chirps whose frequency is shifted due to the Doppler effect [68]. A mono-component LFM signal, or a chirp signal, can be defined as follows:

$$s(t) = Ae^{j\pi\left(m(t-t_0)^2+2f(t-t_0)+\phi\right)}, \tag{2.1}$$

where, A, m, f, ϕ ,and t_0 are the amplitude, chirp-rate, and initial frequency, time shift and initial phase respectively. A noisy mono-component LFM signal, $\widetilde{s}(t)$, can be expressed in the time domain by

$$\widetilde{s}(t) = s(t) + w(t),\ t \in \left(-\frac{T}{2}, \frac{T}{2}\right), \tag{2.2}$$

in which $w(t)$ is the zero-mean additive white circular Gaussian noise with variance σ^2. $w(t)$ is uncorrelated with the signal and its real and imaginary parts are also independent, uncorrelated, and have a variance for both equal to $\sigma^2/2$. The chirp signal consists of a quadratic phase coefficient m, which makes it non-stationary with respect to time. However, this non-linearity results in a linear frequency over the duration of the signal. The instantaneous frequency (IF) of the signal, which represents the frequency at a specific time t, can be obtained by differentiating the instantaneous phase and setting $t_0 = 0$ in the equation mentioned above.

$$IF(t) = mt + f. \tag{2.3}$$

The direction of the frequency sweep can be determined by the sign of the quadratic phase coefficient, denoted by m. When $m > 0$, the frequency increases over time, resulting in an up chirp signal. An example of an up chirp signal in the time domain is shown in Fig. 2.1 and its spectrogram is plotted in Fig. 2.3. If $m < 0$, the frequency decreases over time and the signal is a down chirp. Fig. 2.2 shows a down chirp signal in time domain and Fig. 2.4 plots the spectrogram of the down chirp. It is worth noting that the previous definition was for mono-component LFM signals, whereas K-component LFM signals which have multiple chirps with different frequencies and chirp rates can be defined by

$$s_K(t) = \sum_{k=1}^{K} A_k e^{j\pi\left(m_k(t-t_k)^2 + 2f_k(t-t_k) + \phi_k\right)}, \tag{2.4}$$

where A_k, m_k, f_k, ϕ_k and t_k are amplitude, chirp rate, initial frequency, time shift and initial phase of the k-th individual LFM component, respectively. A K-component noisy LFM signal can be expressed in the time domain as

$$\widetilde{s}_K(t) = s_K(t) + w(t),\ t \in \left(-\frac{T}{2}, \frac{T}{2}\right). \tag{2.5}$$

Estimating chirp rate and initial frequency are crucial in most applications of chirp signals, as they provide valuable information such as the object's position and velocity. As a result, detection and parameter estimation of LFM signals have become a subject of significant interest due to their widespread use in various fields.

2.1.2 Chirp Signal Characteristics

LFM signals have a wide range of applications, including one of the most significant applications in radar technology. In radar, a brief pulse signal is emitted and the receiver gathers some of the energy that is reflected from objects. This process allows us to determine the position, size, direction, and speed of both stationary and moving objects. For example, the time difference between the transmitted and received signals provides information about the distance between the target and the radar. When there are multiple targets in close proximity to each other, the reflected signals become overlapped and difficult to separate. Therefore, the first crucial condition for the pulse is to be as short as possible, as this will improve the distance resolution. However, to detect objects at greater distances, more energy is required. Unfortunately, a short, high-power, and narrow-pulse burst is contradictory when using a conventional pulse. To overcome this limitation, chirp signals are utilized. Using chirp signals in radar technology can enhance performance by several hundred times, as reported by Skolnik [69]. Furthermore, when dealing with multiple

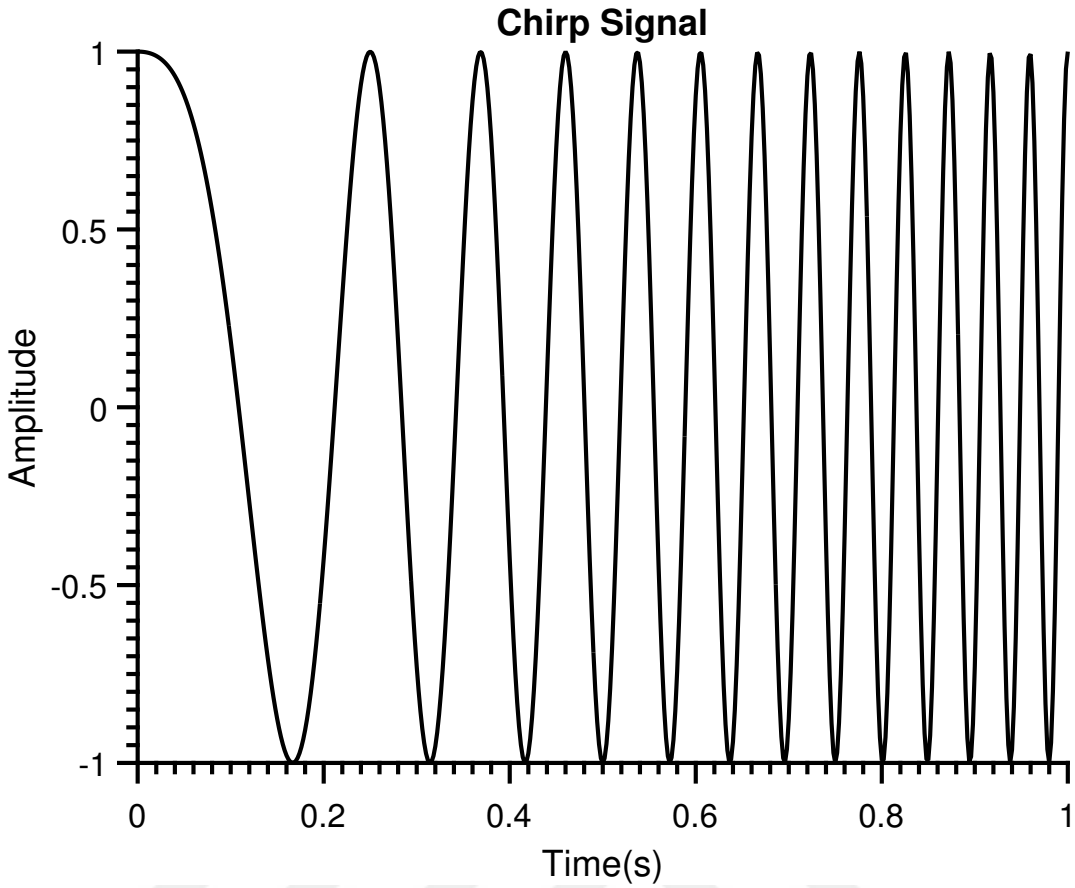

Figure 2.1 Up Chirp signal in time domain.

moving targets, identifying the parameters of multiple chirp signals allows us to obtain information about their position, speed, and acceleration. This importance is due to the following characteristics.

- Low probability of interception [70].
- Low-power transmission needs.
- High Doppler resolution.
- Large time-bandwidth product [71].
- Wide frequency band.
- Long time interval.
- Low probability of detection and identification [72]. Therefore, chirp spread spectrum uses an LFM signal to spread the signal in frequency.

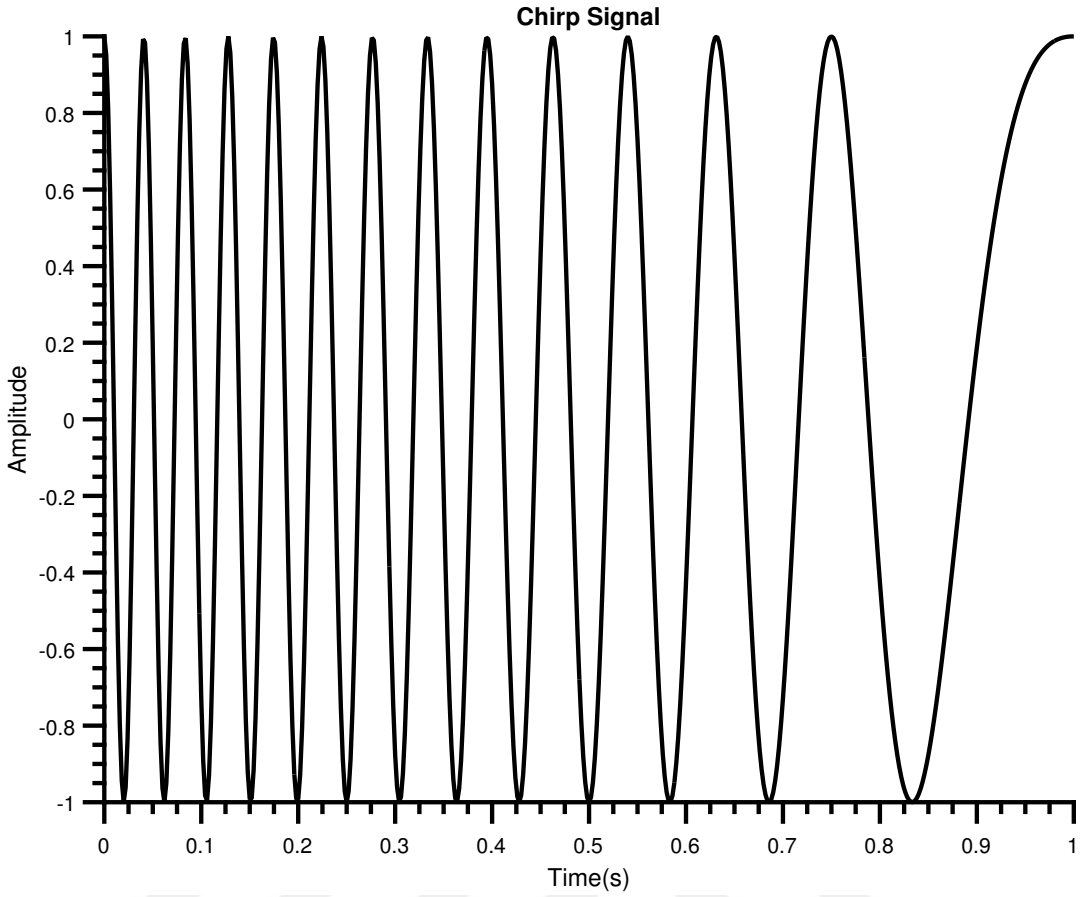

Figure 2.2 Down Chirp signal in time domain.

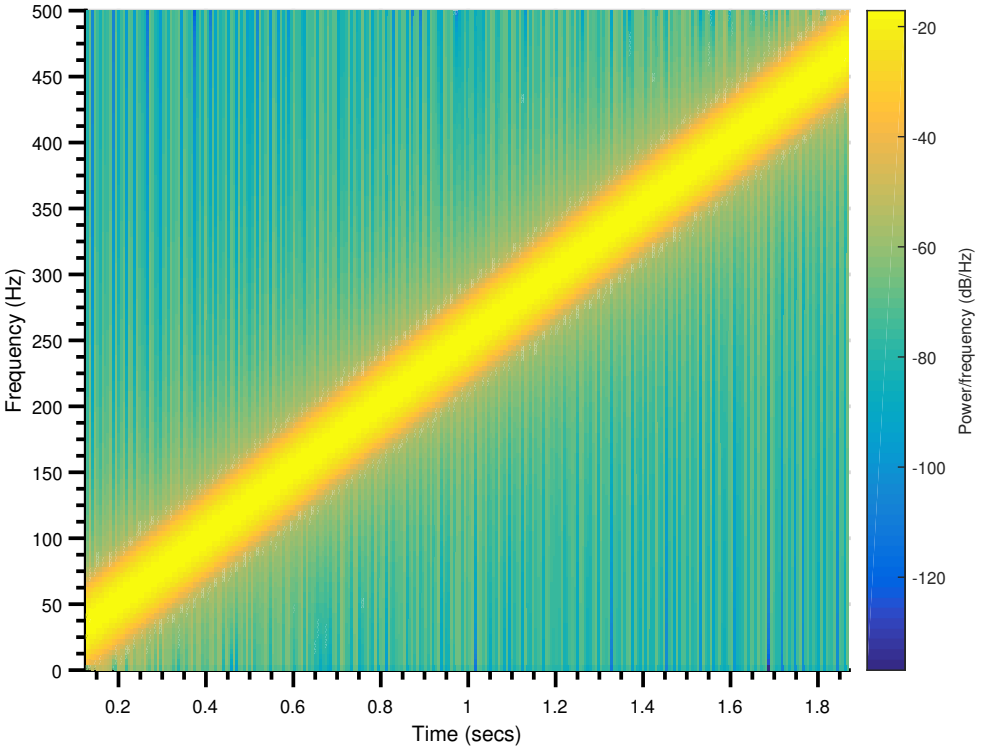

Figure 2.3 The spectrogram of an up chirp.

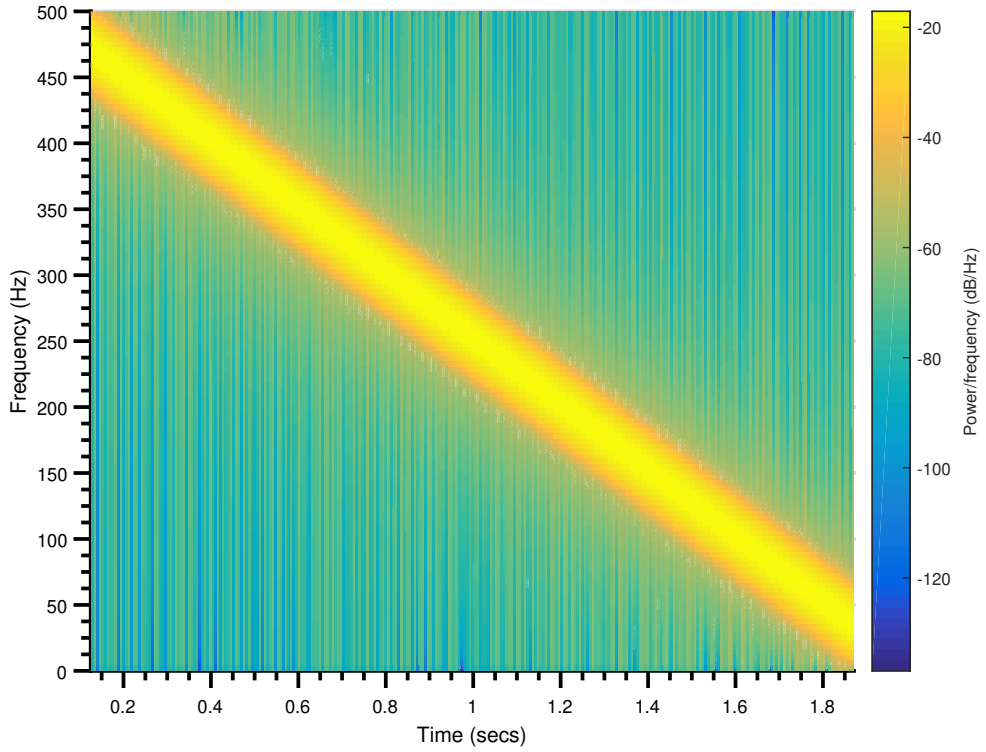

Figure 2.4 The spectrogram of a down chirp.

2.1.3 Applications

Chirp signals are prevalent in various domains, encompassing both natural phenomena and technological applications. In the realm of natural audio signals, chirps can be observed in the melodic calls of birds, the distinctive vocalizations of whales and frogs, as well as the echolocation systems employed by bats and dolphins [73, 74]. They also manifest in biomedical signals like EEG recordings, where they are associated with epileptic seizures [75], and uterine EMG signals, which reflect pregnancy contractions [76]. Furthermore, chirp signals find utility in ultrasound imaging techniques, particularly in the context of tissue harmonic imaging during active transmission [77].

Beyond the realm of biology and medicine, chirp signals have garnered attention and application in a wide range of disciplines. In the field of radar technology, they play a crucial role in radar systems [78], while in sonar systems, they aid in underwater sensing [79]. Aerospace ventures leverage chirp signals for various purposes [80], including probability of intercept radars [70]. In ultrasound applications, chirp signals are utilized for imaging tasks [81]. Synthetic aperture radars rely on chirp signals to enhance imaging capabilities [82]. Chirp signals also find use in wireless communications [83], seismic analysis, geophysics, electronic warfare, and electronic information systems [84–89]. Furthermore, in the realm of high-speed vehicles, such

as the Internet of Vehicles (IoV), chirp signals play a role in communication [90, 91], as well as in assisted driving systems [92, 93].

These examples illustrate the broad spectrum of applications where chirp signals are encountered, highlighting their significance in numerous fields of study and technological advancements.

2.2 Fractional Fourier Transform

2.2.1 Introduction

The FrFT is a highly effective signal processing tool that has found applications in various fields [94–96]. It has been used for time-variant filtering [96], applications of time-frequency (TF) distributions [97], optics [98], and many other areas [99, 100].

A stationary signal has statistically invariant properties over time, which can be represented as a linear combination of sinusoidal signals with different frequencies, amplitudes, and phases. Thus, the FT is an ideal tool for dealing with stationary signals. Likewise, the FrFT is also ideal for studying LFM signals, as they can be decomposed into orthonormal chirp basis functions. The FrFT is highly effective for this purpose due to its low computational cost, it can be implemented with the same computational cost with the FT, cross-term free implementation for the multi component LFM case, and effectiveness in concentrating the energy of an LFM signal. As a result, the FrFT is at the forefront of algorithms operating in the same field.

2.2.2 Definition and Properties

The FrFT is a linear and unitary transform acting on square integrable functions. The FrFT of a signal $f(t)$ is given by

$$F_\alpha(u) = \mathscr{F}^\alpha\{f(t)\}(u) = \int_{-\infty}^{+\infty} f(t) K_\alpha(t,u)\, dt, \tag{2.6}$$

where α is the rotation angle and $K_\alpha(t,u)$ is the kernel of the transform defined by

$$K_\alpha(t,u) = \begin{cases} A_\alpha e^{j\pi\left(t^2\cot\alpha + u^2\cot\alpha - 2tu\csc\alpha\right)}, & \alpha \neq n\pi \\ \delta(t-u), & \alpha = 2n\pi \\ \delta(t+u), & \alpha = (2n+1)\pi \end{cases}$$

where, $\delta(t-u)$ is the identity transform, n is any integer and $A_\alpha = \sqrt{1-j\cot\alpha}$. The FrFT offers greater flexibility in its applications compared to the FT, without incurring

any additional computational cost. As a result, the FrFT can provide additional value in any domain where the FT is used. As the FrFT is an energy-preserving transform, the energy preserved in the time domain signal is equivalent to the energy preserved in the signal following the transformation, without any loss. This can be written as

$$\int_{-\infty}^{+\infty} F_{\alpha}(u)^2\, du = \int_{-\infty}^{+\infty} f(t)^2\, dt. \tag{2.7}$$

The FrFT is characterized by two parameters. The first parameter is the rotation angle, denoted by α, which allows the FrFT to rotate the time-frequency plane counterclockwise around the origin of the coordinates. By analyzing the signal at different rotation angles, the FrFT can extrapolate more information about the signal compared to the FT, making it an ideal tool for signal processing in many applications. Moreover, the FrFT can be viewed as an interpolation between the time domain ($\alpha = 0$) and frequency domain ($\alpha = \pi/2$). The FT can be regarded as a rotation from time to frequency axis with $\alpha = \pi/2 + 2n\pi$. The kernel becomes the identity operator when $\alpha = 2n\pi$, while the FrFT becomes the inverse FT when $\alpha = -\pi/2 + 2n\pi$, and the kernel becomes the counteridentity operator when $\alpha = -\pi$. The second parameter of the FrFT is u, which is the variable of the transform in the new time-frequency plane rotated by α. The transformed domain u is sometimes referred to as the fractional Fourier domain frequency, which is similar to the frequency concept in FT. In this context, the FrFT maps the time domain signal to another domain, the u domain. Figure 2.5 illustrates an LFM signal in the time-frequency domain in the top-left part of the figure, and in the top-right part, it shows the rotated time-frequency domain where only the u domain is plotted.

The rotation property is considered as one of the most significant properties of the FrFT. Some studies even define FrFT using this property. As it is well-known, the WVD of an LFM signal, $W_s(t, f)$, can be visualized as a line in the time-frequency plane. Therefore, the FrFT can be seen as the operation that rotates $W_s(t, f)$ clockwise by a rotation angle α, as illustrated in Figure 2.6. It can be concluded that the FrFT can be viewed either as a rotation of the time-frequency plane counterclockwise around the origin of the coordinates or as the rotation of the signal clockwise around the origin of the coordinates. The WVD of the FrFT of $s(t)$ is

$$W_{s_\alpha}(t, f) = W_s(t\cos\alpha - f\sin\alpha, t\sin\alpha + f\cos\alpha). \tag{2.8}$$

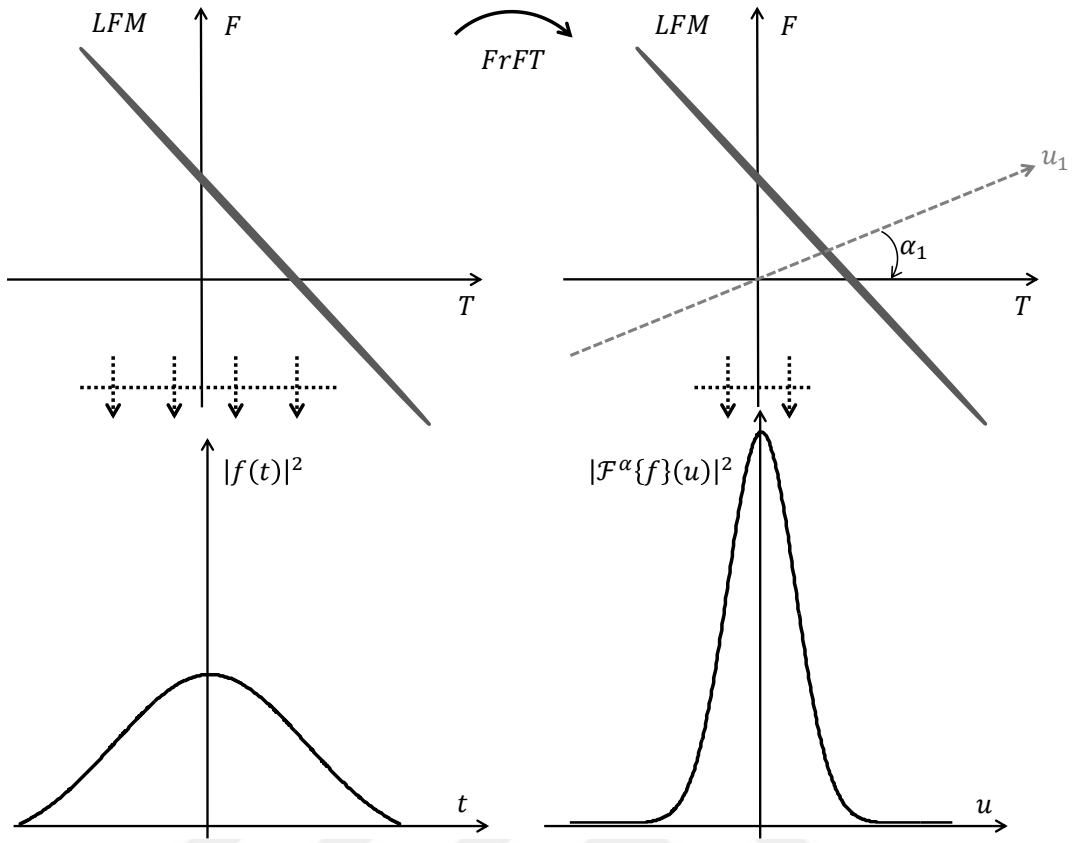

Figure 2.5 Rotation property of FrFT.

Then, $W_{s_\alpha}(t,f)$ is the rotation version of $W_s(t,f)$, the integral projection of the signal FrFT onto the transformed axes is squared magnitude of the FrFT-domain signal

$$\int_{-\infty}^{+\infty} W_{s_\alpha}(t,f)df = |F_\alpha(u)|^2. \tag{2.9}$$

Bottom part of Figure 2.5 illustrates this property, in which the energy of an LFM signal is concentrated in the FrFT domain as a result of the reduction in the support.

2.2.3 Energy Concentration in the FrFT Domains

The chirp signal exhibits a unique characteristic where it cannot be compact in either time or frequency domains; however, it can transform into a Dirac function in the fractional domain at the optimal rotation angle, concentrating the signal energy and turning the LFM into an impulse with maximum magnitude. The FrFT's rotation operation effectively concentrates the signal energy while dispersing noise energy in the u domain, making it invaluable for applications in low SNR environments. The FrFT's capability to operate effectively in the presence of high noise levels enhances its utility in such scenarios. By decomposing signals into chirp bases, the FrFT serves as a powerful tool for analyzing LFM signals, leveraging the computation process

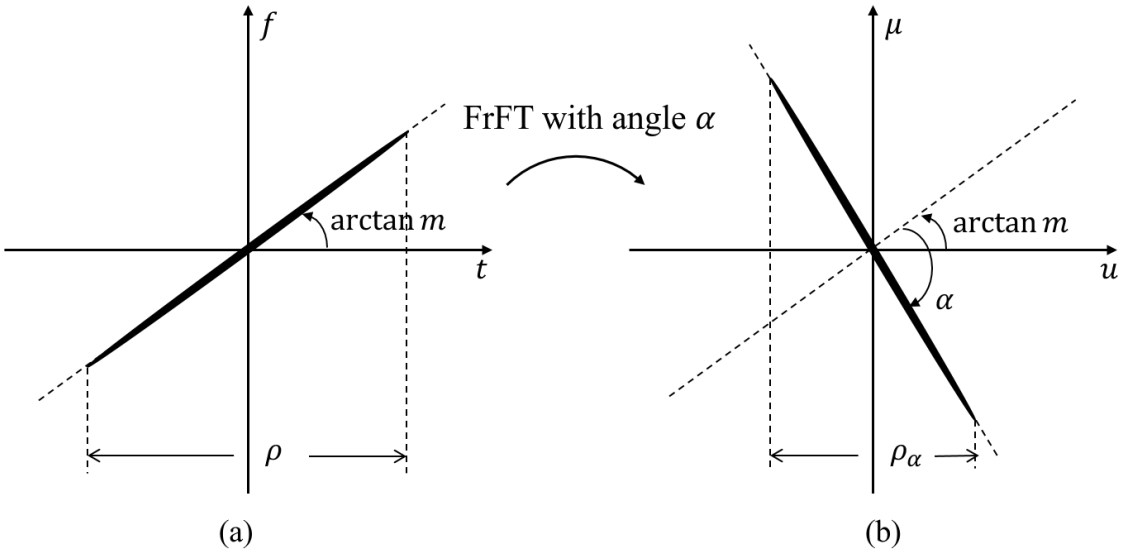

Figure 2.6 A chirp signal(a) in time-frequency plane and (b) rotated counter-clockwise by an angle of α due to the FrFT. Support of the transformed signal changes.

that involves multiplication by a chirp signal, followed by FT, scaling, and another multiplication by a chirp signal. This computation reveals that the basis functions in the FrFT are the chirp signals themselves. In the analysis of multi-component LFM signals, cross-terms pose a significant challenge; however, the FrFT, being a linear integration technique, overcomes this issue by operating without cross-terms, facilitating accurate analysis and estimation of LFM signals.

2.2.4 Computationally Efficient

FrFT has the same computational cost of FFT. The computational cost of FrFT is $\mathcal{O}(N \log N)$ for a signal of length N [101]. Therefore, there is no additional cost compared with FFT.

2.2.5 Examples of FrFT Based Estimation Algorithms

FrFT-based algorithms are commonly used to estimate LFM signal parameters as kernel of the FrFT consists of LFM signals, making it a natural domain for detection and parameter estimation [102–108]. In [104], the FrFT was shown to be an effective approach for estimating LFM signal parameters. To address the heavy computational cost of searching the entire fractional order space, coarse-to-fine search approaches were proposed in [102–105]. In [102], a quasi-Newton method was used for detection and parameter estimation using the peak magnitude of the FrFT and the variance of the FrFT-based estimator was derived. However, the proposed algorithm only

considered the mono-component case with high computational cost. In [103], a method for signal and image recovery in the FrFT domains using the method of alternating projections (MAP) was proposed. The MAP concept was introduced, and its implementation for signal and image recovery in fractional Fourier domains was explained. Performance of the proposed method was evaluated only through numerical simulations and compared with existing methods. In [105], a coarse-to-fine grid-search strategy was used to decrease the computational cost by using the peak magnitude of the FrFT domains. In [106], approximations, upper and lower bounds for the peak magnitude of the FrFT domains were proposed for mono and multi component cases. Analytical formulas were used to estimate the chirp rate, but this method can only be used for LFM signals modulated by a Gaussian window. In [109], accurate parameter estimation is achieved by leveraging information entropy. The technique takes advantage of the correlation between the distribution of information entropy and the concentration of LFM signal energy at different FrFT orders. By utilizing this correlation, the information entropy is employed as the target function for precise estimation of LFM signal parameters. In [110] an efficient method for parameter estimation and separation of multi-component LFM signals is proposed. The method explores rotation characteristics in the time-frequency domain and energy aggregation characteristics in the FrFT domain. It utilizes STFT for initial search interval determination and incorporates the Savitzky-Golay filter for smoothing and rough estimation of the optimal order search center. Additionally, an FrFT domain filter is employed to handle interference from overlapping components. However, the SNR breakdown threshold is high and the algorithm's removal strategy, aimed at reducing total signal power, leads to a decrease in estimation accuracy. In [111] It has been shown that the fractional auto-correlation cluster along lines passing through the origin with slopes corresponding to chirp rates. Leveraging the relationship between fractional auto-correlation FrFT the chirp rates has been extracted. However, the SNR breakdown threshold is high.

2.2.6 Limitations of the Current FrFT Based Estimation Algorithms

Despite the FrFT being an ideal tool for analyzing and estimating the parameters of chirp signals, current FrFT-based algorithms suffer from one or more of the following drawbacks.

- The trade-off between the estimation accuracy and the search step size of the rotation angle.
- Discretization of u leading to the picket fence effect.

- Spectral leakage, also known as the shading problem or bias effect, in multi-component chirp signal cases. This occurs when the sidelobes of the strong component (the component with higher energy than the others) shade the weak component, affecting not only its amplitude but also causing a slight shift at the index of the maximum squared value of the FrFT. The bias effect can be controlled by adjusting the amplitude, chirp rate, and sampling time [112].
- The error propagation effect, where the error in estimating the first component is propagated and affects the estimation accuracy of the other components.

Iterative interpolation methods presented in [113] aimed to overcome the challenges mentioned above and improve the fine search approach. However, these methods suffered from reduced accuracy and did not solve the bias effect.

Several algorithms adopted a technique in which the strongest component is first detected and its parameters are estimated, then, this component is subtracted from the original multi-component signal, and the algorithm is iterated until all components of the signal parameters are estimated. While this strategy can eliminate the bias effect, it increases the computational cost as the algorithm has to recalculate and estimate only one component's parameters in each iteration. Moreover, the error propagation effect can occur where the error in estimating the first component propagates and affects the accuracy of estimating the other components. In order to address these challenges, new FrFT-based algorithms have been proposed.

2.3 LFM Parameters Estimation Using the Fractional Fourier Transform

2.3.1 Introduction

Chirp signals have become a focal point in the fields of radar and signal processing in recent times. A notable application is the interception and estimation of chirp signals to deceive an enemy's reconnaissance radar by detecting and estimating the signals sent by the enemy, and then transmitting false echo signals. The detection and parameter estimation of LFM signals have also garnered significant attention due to their widespread use in various applications.

2.3.2 The LFM Signal in the Fractional Fourier Domain

The FrFT is a powerful tool for estimating LFM parameters, as it decomposes the signal into orthonormal chirp basis functions. An LFM signal can be transformed to its most

compact form, becoming a Dirac, in its optimum FrFT domain. The key to estimating LFM parameters using the FrFT is to rotate the time-frequency plane by an angle α. This changes the energy concentration of the signal in the u domain. For certain values of α the signal becomes more compact in the u domain, resulting in increased magnitude due to the preservation of energy through the FrFT. The optimum angle, α_{opt}, is the specific rotation angle where the FrFT of a chirp is the most concentrated to its compactest form throughout all the FrFT domains, resulting in maximum energy concentration and the highest magnitude of the transformed LFM signal in the u domain [104]. The signal will achieve the highest amplitude in u domain at

$$u_{opt} = f \sin \alpha_{opt}, \tag{2.10}$$

in which we call u_{opt} is the optimum value of u. A search for the maximum value in the $\{u, \alpha\}$ domains leads to following estimator [104, 106]

$$\left\{\widehat{\alpha}_{opt}, \widehat{u}_{opt}\right\} = \underset{\alpha,u}{\operatorname{argmax}} \left\{ \left| \mathscr{F}^{\alpha} \left\{ s(t) \right\} (u) \right|^2 \right\}. \tag{2.11}$$

For a single component LFM signal whose chirp-rate is m, the relation between the actual chirp-rate, m, and α_{opt} is [104]

$$\alpha_{opt} = \operatorname{arctan}(m) + \frac{\pi}{2} + n\pi, \tag{2.12}$$

Then, the estimated chirp-rate and initial frequency can be obtained by

$$\widehat{m} = -\cot \widehat{\alpha}_{opt}, \tag{2.13a}$$

$$\widehat{f} = \widehat{u}_{opt} \csc \widehat{\alpha}_{opt}, \tag{2.13b}$$

where $\widehat{m}$ and $\widehat{f}$ are the estimated values of the chirp-rate and initial frequency, respectively. For the K-component case, the u, α domains contain K peaks which correspond to the number of the LFM components. To estimate α_{opt} and u_{opt}, a two-dimensional search is required. Figure 2.7 plots a bi-component chirp signal in the noiseless case, where we have selected the chirp rates as $\mathbf{m} = [-0.2, 0.2]^T$ and the initial frequencies were $\mathbf{f} = [-0.1, 0.1]^T$ with signal length $N = 1024$ and $A = 1$. It is clear from the figure that the FrFT domain has two distinct peaks related to the chirp rates and initial frequencies. Figure 2.8 plots the same bi-component chirp signal, but this time with $SNR = -6dB$. The figure shows that the two peaks related to the two components are very distinct in spite of the high level of noise, which clearly demonstrates the noise immunity of the FrFT.

Hence, we can state that the chirp parameters can be estimated reliably by locating

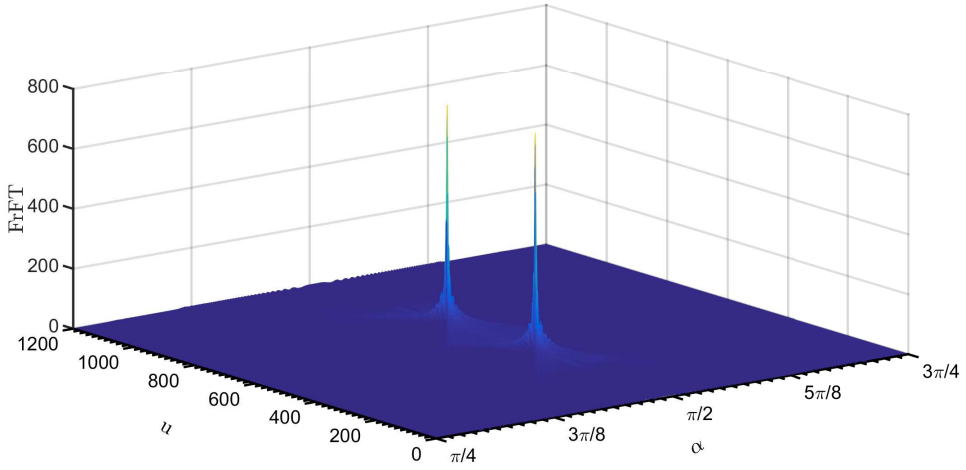

Figure 2.7 The magnitude of the FrFT of two component LFM signal in noiseless case.

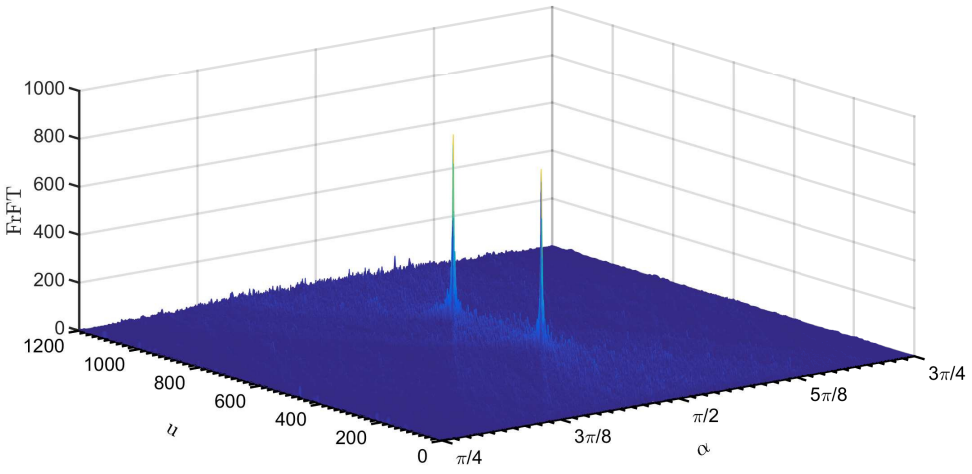

Figure 2.8 The magnitude of the FrFT of two component LFM signal when $SNR = -6dB$.

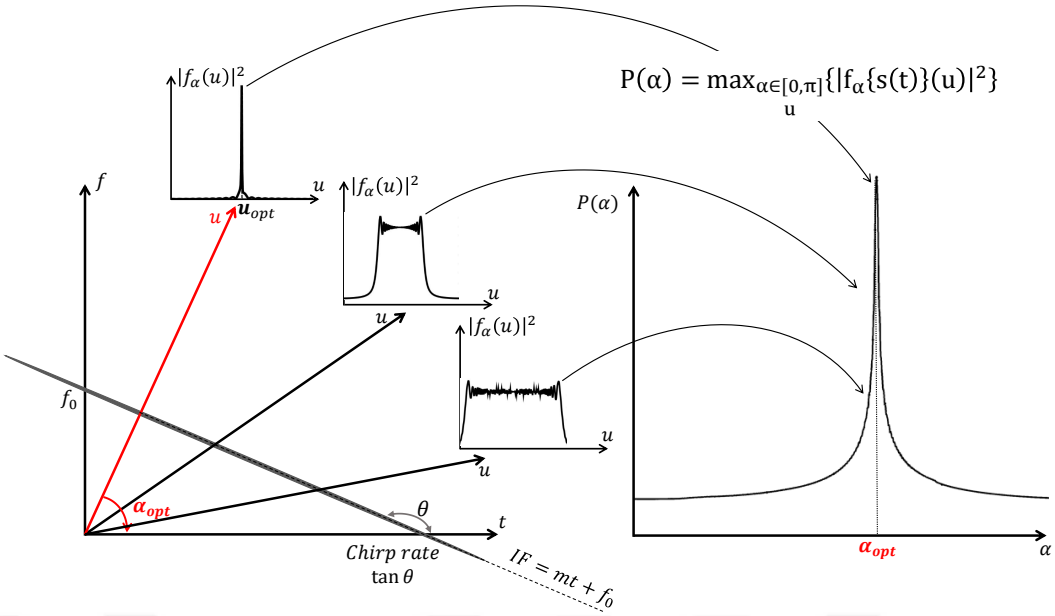

Figure 2.9 The $P(\alpha)$ function for a mono-component LFM signal.

the maximum values in the u, α domains using (2.11) and then estimating the chirp parameters using (2.13). However, this search can be computationally intensive, especially due to the two-dimensional search. Therefore, alternative methods with lower computational complexity are required for the estimation process.

In the following chapter, we demonstrate that the chirp-rate can be efficiently estimated through a one-dimensional search using a particular function. Thus, the joint estimation of α_{opt} and u_{opt} can be achieved by performing two one-dimensional searches in the FrFT domain. Furthermore, we show that estimating u_{opt} has no impact on the estimation of α_{opt}. As a result, we can estimate α_{opt} first and then estimate u_{opt} using the estimated α_{opt}. To this end, we define the unimodal function $P(\alpha)$ as [104, 106, 114],

$$P(\alpha) = \max_{u} \left\{ \left| \mathscr{F}^{\alpha} \{s(t)\}(u) \right|^2 \right\}, \tag{2.14}$$

in which this function has a unique peak at

$$\widehat{\alpha}_{opt} = \underset{\alpha}{\operatorname{argmax}} \{P(\alpha)\}, \tag{2.15}$$

for the mono-component LFM signal, and K peaks for a K-component LFM signal. The function $P(\alpha)$ has been utilized in several studies to estimate the chirp-rate of mono-component LFM signals [104, 106, 114]. It has been demonstrated in [104] that $P(\alpha)$ yields an asymptotically optimal estimator. Figure 2.9 illustrates the $P(\alpha)$ function for a mono-component LFM signal. As depicted in the figure, the $P(\alpha)$ function possesses a single peak at α_{opt}.

2.3.3 The Spectral Behaviour of LFM Signals in the Fractional Fourier Domains

Figure 2.10 shows the squared magnitude of the FrFT for a finite length LFM signal for four cases of α: (i) when α is far from α_{opt}, (ii) when α is moderately far from α_{opt}, (iii) when α is close to α_{opt}, and (iv) when $\alpha = \alpha_{opt}$. These plots demonstrate that due to the rotational property of the FrFT, the energy concentration changes with α. As the support width in the transformed u domain, ρ_α decreases, the amplitude of the transform increases until reaching the optimal rotation angle α_{opt}. At this rotation angle the energy concentration is maximum, and a distinct peak appears in the u domain.

When considering an LFM signal, the FrFT rotation angle α can have a significant impact on the resulting spectrum. When α is far from the optimal FrFT angle, α_{opt}, the spectrum appears nearly rectangular, and the support of the spectrum ρ_α is large, as shown in Figure 2.10 (a). However, as α approaches α_{opt}, the support becomes smaller, as demonstrated in Figure 2.10 (b). When α is very close to α_{opt}, there is only one maximum in the FrFT amplitude spectrum, and the support is very small, as depicted in Figure 2.10 (c). Finally, when $\alpha = \alpha_{opt}$, a distinct peak with zero support emerges in the u domain, as shown in Figure 2.10 (d). One can observe the change in support with the rotation angle by referring to Figure 2.11. In the time-frequency plane, the chirp signal appears as a line ρ, which makes an angle $\arctan m$ with the time axis. If the duration of the chirp signal in the time domain is T then

$$\rho = \frac{T}{|\cos(\arctan m)|}. \tag{2.16}$$

The effective support, denoted by ρ_α, is defined as the energy distribution support in the u domain, which is obtained by projecting ρ onto the u axis. For a given rotation angle α, the expression for ρ_α is given by

$$\rho_\alpha = \rho|\cos(\alpha - \arctan m)|. \tag{2.17}$$

When the rotation angle is optimal, i.e., $\alpha_{opt} = \arctan m + \pi/2$, the term $\cos(\alpha_{opt} - \arctan m)$ becomes zero, causing the projection onto the u axis to shrink to a point. As the duration of the signal approaches infinity, the energy concentrates to form a distinct peak in the u domain. Therefore, the key to obtaining the optimum FrFT angle is to search for the angle of rotation that yields the maximum in the FrFT magnitude spectrum.

From Figure 2.11, one can also observe how the support varies with α. As a result, the spectral distribution of the LFM signal at any FrFT angle exhibits certain

characteristics, as described in [113].

- Using (2.17), the support of the FrFT of an LFM signal can be given by

$$\rho_\alpha = T \left| \frac{\cos(\alpha - \arctan m)}{\cos(\arctan m)} \right| = \frac{T}{\csc \alpha} \left| m + \cot \alpha \right|. \tag{2.18}$$

  Therefore, the support of the spectral distribution in the FrFT domain is controlled only by α.

- The index of the center point of the effective support, u_c, is

$$u_c = f \sin \alpha. \tag{2.19}$$

- When the rotation angle α is far from the optimum angle α_{opt}, the spectral distribution of the LFM signal has a shape that is very close to a rectangle, with two maximum values located at indices u_{max1} and u_{max2}. These indices shift away from the starting and ending points of the effective support by a small amount Δu, as illustrated in Figure 2.10 (a).

- As α approaches α_{opt} (see Figure 2.10 (b)), the energy concentration increases, the effective support ρ_α decreases, and the rectangular spectral distribution narrows. However, there are still two maximum values $|S_\alpha(u_{\text{max1}})|^2$ and $|S_\alpha(u_{\text{max2}})|^2$.

- When α gets closer to α_{opt}, the effective support ρ_α decreases further, and only one maximum occurs at the index u_c, as shown in Figure 2.10 (c).

- When α is equal to α_{opt}, the energy is maximally concentrated, forming a distinct peak in the spectral distribution, as shown in Figure 2.10 (d).

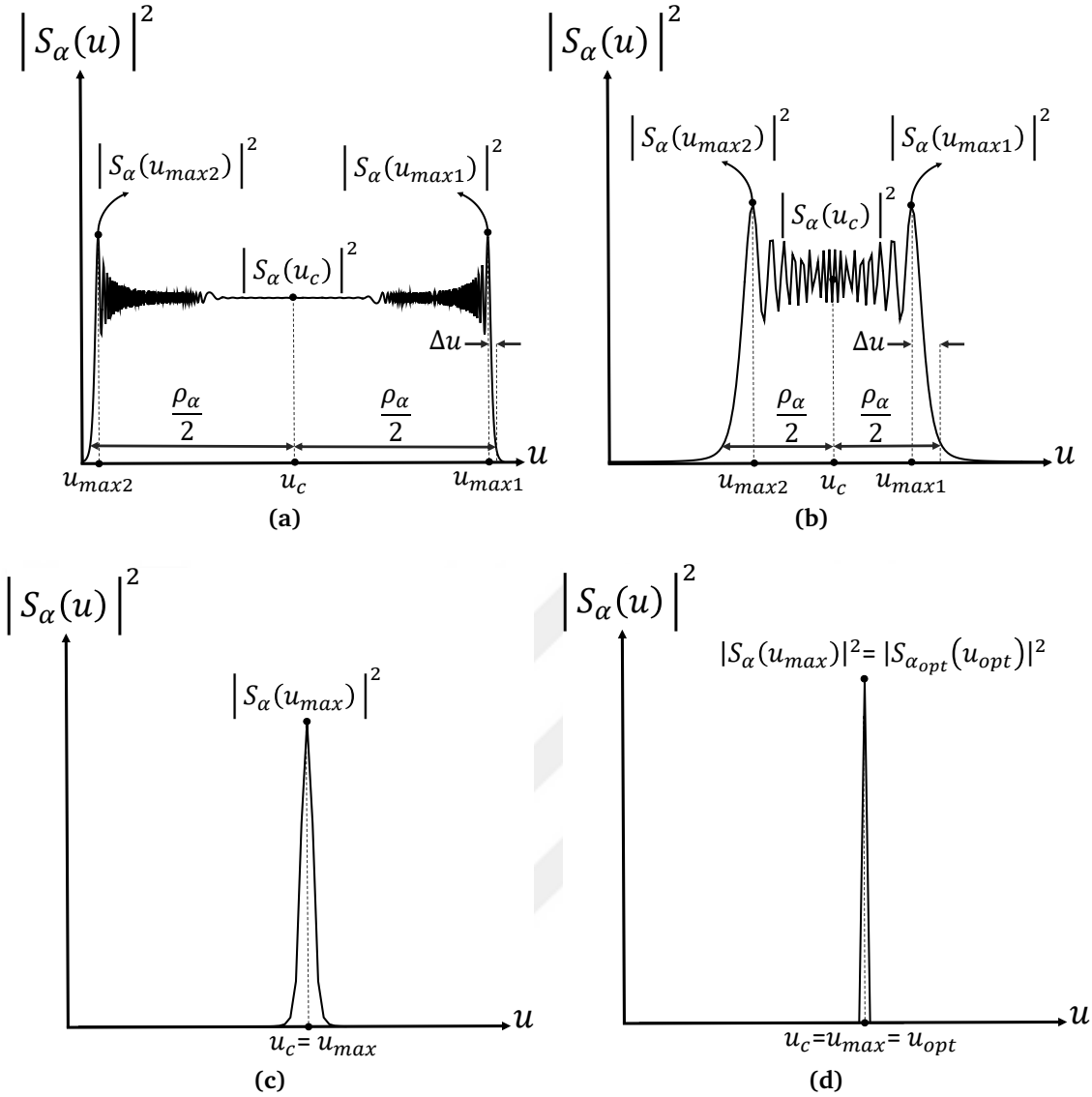

Figure 2.10 LFM signal in u domains.

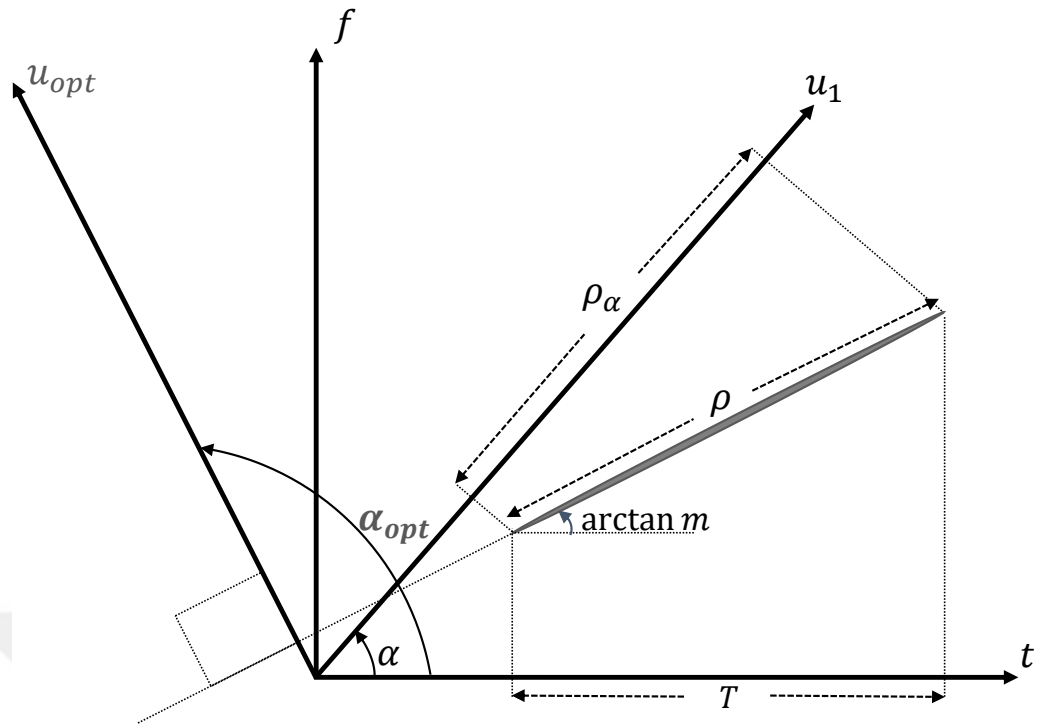

Figure 2.11 The support of mono-component LFM signal in two different u domains, u_1 when α is far from α_{opt} and u_{opt} when $\alpha = \alpha_{opt}$.

3
Performance of Chirp Parameter Estimation In The Fractional Fourier Domains

3.1 Introduction

The primary objective of this chapter is to perform a first-order statistical perturbation analysis on a FrFT-based chirp parameter estimator. The aim is to derive an asymptotically approximated variance of the estimated parameters. Through this analysis, we will establish the optimality of using a FrFT-based estimator for the chirp parameters estimation. The perturbation analysis will also reveal the extent to which the estimator's performance deviates from the ideal situation in the presence of noise. Assuming a large number of samples, we will calculate the asymptotic theoretical variance of the FrFT-based estimator and compare it to the theoretical lower bounds (CRLB).

3.2 Optimality of Chirp Parameter Estimation in the Fractional Fourier Domains

This section aims to demonstrate that the FrFT domain-based approach for estimating chirp parameters yields an optimal, unbiased estimator that can achieve the CRLB.

3.2.1 Cramér–Rao Lower Bound

The CRLB is defined as the minimum variance that can be achieved by any estimator, which is given by the inverse of the Fisher information [3]. It sets a limit on how precise an estimator can be constructed. According to [115, 116], the CRLB for the initial frequency and chirp rate estimator can be expressed as follows:

$$var(\widehat{m})=\frac{90\sigma^2}{A^2\pi^2T^5}, var\left(\widehat{f_0}\right)=\frac{3\sigma^2}{2A^2\pi^2T^3}. \tag{3.1}$$

3.2.2 Preliminary

The main objective of this analysis is to perform a statistical analysis, or first-order perturbation analysis, to determine the asymptotically approximated statistical properties of the FrFT-based estimator for the chirp parameter of a mono LFM signal. Our goal is to show that the FrFT-based estimator is asymptotically optimal, achieving the CRLB and being asymptotically unbiased. It is well-known that the chirp parameter estimation in the FrFT domain is equivalent to the maximum-likelihood estimator for Additive White Gaussian Noise (AWGN) and yields an efficient estimator that achieves the CRLB. However, to the best of our knowledge, this thesis is the first to provide a correct theoretical proof and derivations, taking into account the existence of previous mistaken attempts with the same goal. This chapter will present a detailed and rigorous proof of the optimality of chirp parameter estimation using the FrFT. In the next section, the perturbation analysis of $\widehat{\alpha}_{opt}$ and $\widehat{u}_{opt}$ will be performed first. Then, using the relationship between $\left(\widehat{\alpha}_{opt}, \widehat{u}_{opt}\right)$ and $(\widehat{m}, \widehat{f_0})$ which is defined in (2.13) the performance of the estimates of the chirp-rate and the initial frequency will be analysed. For simplicity, We will use the notation $|S_\alpha(u)|^2$ to represent the magnitude square of the FrFT of $s(t)$, which is defined in (2.1) as a noiseless mono LFM signal, i.e.,

$$|S_\alpha(u)|^2 = |\mathscr{F}^\alpha\{s(t)\}(u)|^2, \quad (w(t) = 0). \tag{3.2}$$

Similarly, we will use the notation $\left|\widetilde{S}_\alpha(u)\right|^2$ to represent the magnitude square of the FrFT of $\widetilde{s}(t)$, which is defined in (2.2) as a noisy mono LFM signal, i.e.,

$$\left|\widetilde{S}_\alpha(u)\right|^2 = |\mathscr{F}^\alpha\{\widetilde{s}(t)\}(u)|^2, \quad (w(t) \neq 0). \tag{3.3}$$

This way, we can easily distinguish between the noiseless and noisy cases in our analysis. We remind the reader that $w(t)$ denotes the additive white Gaussian noise with variance σ^2.

3.2.3 Perturbation Analysis

In the noiseless case, the maximum of $|S_\alpha(u)|^2$ for a chirp signal occurs at (α_{opt}, u_{opt}). Assuming differentiability of $|S_\alpha(u)|^2$ at (α_{opt}, u_{opt}), the derivative of the maximum of $|S_\alpha(u)|^2$ at (α_{opt}, u_{opt}) [114, 117, 118] can be expressed as zero, i.e.,

$$\frac{\partial}{\partial \alpha}|S_\alpha(u)|^2\Big|_{\substack{\alpha_{opt}\\u_{opt}}} = 0, \qquad \frac{\partial}{\partial u}|S_\alpha(u)|^2\Big|_{\substack{\alpha_{opt}\\u_{opt}}} = 0. \tag{3.4}$$

When the noise is introduced, the noisy $\left|\widetilde{S}_\alpha(u)\right|^2$ is

$$\left|\widetilde{S}_\alpha(u)\right|^2 = |S_\alpha(u) + W_\alpha(u)\,|^2, \tag{3.5}$$

where $W_\alpha(u)$ is the FrFT of the noise $w(t)$ at the angle α. This can be expanded to

$$\left|\widetilde{S}_\alpha(u)\right|^2 = S_\alpha(u)S_\alpha^*(u) + W_\alpha(u)S_\alpha^*(u) + S_\alpha(u)W_\alpha^*(u) + W_\alpha(u)W_\alpha^*(u), \tag{3.6}$$

where $(\cdot)^*$ represents the conjugation. When the noise is low powered in comparison with the power of the signal, $W_\alpha(u)W_\alpha^*(u)$ can be omitted. Then the equation above can further be rearranged as

$$\left|\widetilde{S}_\alpha(u)\right|^2 \approx |S_\alpha(u)|^2 + \delta S_\alpha(u), \tag{3.7}$$

where

$$\delta S_\alpha(u) \approx W_\alpha(u)S_\alpha^*(u) + S_\alpha(u)W_\alpha^*(u), \tag{3.8}$$

which represents the additive perturbation component. Due to the existence of $\delta S_\alpha(u)$ in the presence of noise, the indexes α_{opt} and u_{opt}, at which $|S_\alpha(u)|^2$ reaches its maximum value in the noiseless case have been moved to $\alpha_{opt} + \delta\alpha$ and $u_{opt} + \delta u$, respectively, where $\delta\alpha$ and δu are random disturbances in α domain and u domain respectively. Fig. 3.1 and Fig. 3.2 plot $\delta\alpha$ and δu in α domain and u domain. Consequently, the estimates of the new indexes α_{opt} and u_{opt} are

$$\widehat{\alpha}_{opt} = \alpha_{opt} + \delta\alpha, \qquad \widehat{u}_{opt} = u_{opt} + \delta u. \tag{3.9}$$

Assuming that (3.7) is differentiable, its partial derivatives at this new maximum indexes are zero, as expressed by

$$\frac{\partial}{\partial\alpha}\left(|S_\alpha(u)|^2 + \delta S_\alpha(u)\right)\Big|_{\substack{\alpha_{opt}+\delta\alpha \\ u_{opt}+\delta u}} = 0. \tag{3.10a}$$

$$\frac{\partial}{\partial u}\left(|S_\alpha(u)|^2 + \delta S_\alpha(u)\right)\Big|_{\substack{\alpha_{opt}+\delta\alpha \\ u_{opt}+\delta u}} = 0. \tag{3.10b}$$

According to [119] (Sec. 9.6), a statistical linearization under the assumption of large T and high SNR will suffice to derive the asymptotic properties. The first-order Taylor expansion of the equation above yields

$$\frac{\partial}{\partial\alpha}|S_\alpha(u)|^2\Big|_{\substack{\alpha_{opt} \\ u_{opt}}} + \frac{\partial\,\delta S_\alpha(u)}{\partial\alpha}\Big|_{\substack{\alpha_{opt} \\ u_{opt}}} + \frac{\partial^2|S_\alpha(u)|^2}{\partial\alpha^2}\Big|_{\substack{\alpha_{opt} \\ u_{opt}}}\delta\alpha + \frac{\partial^2}{\partial\alpha\partial u}|S_\alpha(u)|^2\Big|_{\substack{\alpha_{opt} \\ u_{opt}}}\delta u \approx 0, \tag{3.11a}$$

$$\frac{\partial}{\partial u}|S_\alpha(u)|^2\Big|_{\substack{\alpha_{opt}\\u_{opt}}} + \frac{\partial}{\partial u}\delta S_\alpha(u)\Big|_{\substack{\alpha_{opt}\\u_{opt}}} + \frac{\partial^2|S_\alpha(u)|^2}{\partial u^2}\Big|_{\substack{\alpha_{opt}\\u_{opt}}}\delta u + \frac{\partial^2}{\partial\alpha\partial u}|S_\alpha(u)|^2\Big|_{\substack{\alpha_{opt}\\u_{opt}}}\delta\alpha \approx 0, \tag{3.11b}$$

where the higher-order additive terms of orders $\mathcal{O}(\delta\alpha^2)$, $\mathcal{O}(\delta u^2)$, and $\mathcal{O}(\delta\alpha\delta u)$ are ignored. The theoretical derivations are achieved by applying the first-order perturbation analysis of maxima of random functions similar to the one in [6] and [107], Where only the zeroth order Taylor term $\frac{\partial\delta S_\alpha(u)}{\partial\alpha}\Big|_{\substack{\alpha_{opt}\\u_{opt}}}$ is considered, while the first order terms in the expansion $\frac{\partial 2\delta S_\alpha(u)}{\partial\alpha^2}\Big|_{\substack{\alpha_{opt}\\u_{opt}}}\delta\alpha$ and $\frac{\partial 2\delta S_\alpha(u)}{\partial\alpha\partial u}\Big|_{\substack{\alpha_{opt}\\u_{opt}}}\delta u$ are ignored because their effects can be neglected. The first terms in both of the above equations are zero as given by (3.4). Therefore, (3.11) can be simplified to

$$\frac{\partial}{\partial\alpha}\delta S_\alpha(u)\Big|_{\substack{\alpha_{opt}\\u_{opt}}} + \frac{\partial^2}{\partial\alpha^2}|S_\alpha(u)|^2\Big|_{\substack{\alpha_{opt}\\u_{opt}}}\delta\alpha + \frac{\partial^2}{\partial\alpha\partial u}|S_\alpha(u)|^2\Big|_{\substack{\alpha_{opt}\\u_{opt}}}\delta u \approx 0, \tag{3.12a}$$

and

$$\frac{\partial}{\partial u}\delta S_\alpha(u)\Big|_{\substack{\alpha_{opt}\\u_{opt}}} + \frac{\partial^2}{\partial u^2}|S_\alpha(u)|^2\Big|_{\substack{\alpha_{opt}\\u_{opt}}}\delta u + \frac{\partial^2}{\partial u\partial\alpha}|S_\alpha(u)|^2\Big|_{\substack{\alpha_{opt}\\u_{opt}}}\delta\alpha \approx 0. \tag{3.12b}$$

Combining the equations above yields

$$\begin{bmatrix} s_{11} & s_{12} \\ s_{12} & s_{22} \end{bmatrix}\begin{bmatrix} \delta\alpha \\ \delta u \end{bmatrix} = -\begin{bmatrix} s_1 \\ s_2 \end{bmatrix}, \tag{3.13}$$

where

$$s_{11} = \frac{\partial^2}{\partial\alpha^2}|S_\alpha(u)|^2\Big|_{\substack{\alpha_{opt}\\u_{opt}}}, \qquad s_{22} = \frac{\partial^2}{\partial u^2}|S_\alpha(u)|^2\Big|_{\substack{\alpha_{opt}\\u_{opt}}}$$
$$s_{12} = \frac{\partial^2}{\partial\alpha\partial u}|S_\alpha(u)|^2\Big|_{\substack{\alpha_{opt}\\u_{opt}}}, \qquad s_1 = \frac{\partial}{\partial\alpha}\delta S_\alpha(u)\Big|_{\substack{\alpha_{opt}\\u_{opt}}}, \qquad s_2 = \frac{\partial}{\partial u}\delta S_\alpha(u)\Big|_{\substack{\alpha_{opt}\\u_{opt}}}. \tag{3.14}$$

Therefore, the perturbations $\delta\alpha$ and δu are

$$\begin{bmatrix} \delta\alpha \\ \delta u \end{bmatrix} = -\begin{bmatrix} s_{11} & s_{12} \\ s_{12} & s_{22} \end{bmatrix}^{-1}\begin{bmatrix} s_1 \\ s_2 \end{bmatrix}. \tag{3.15}$$

The 2×2 matrix on the right hand side of the equation above is a Hessian, which is demonstrably a positive definite and therefore, an invertible matrix. Then

$$\delta\alpha = \frac{s_1 s_{22} - s_2 s_{12}}{s_{11}s_{22} - s_{12}^2}.$$

$$\delta u = \frac{s_2 s_{11} - s_1 s_{12}}{s_{11} s_{22} - s_{12}^2}. \tag{3.16}$$

3.2.4 Statistical Properties of the FrFT Estimator

The main focus of this subsection is to evaluate the performance of the FrFT domain chirp parameter estimator. Firstly, we aim to demonstrate that the estimator is unbiased, which can be expressed as $E\{\delta\alpha\} = 0$ and $E\{\delta u\} = 0$. Next, we proceed to calculate the variances of the estimator, denoted by, $\text{var}(\delta\alpha)$ and $\text{var}(\delta u)$. Upon obtaining the variances $\delta\alpha$ and δu, we can then determine the variance of the estimates for chirp-rate and initial frequency. For simplicity, we shall denote $\overline{\alpha} = \alpha_{opt}$ and $\overline{u} = u_{opt}$, where

$$\overline{\alpha} = \arctan(m) + \frac{\pi}{2}, \qquad \overline{u} = \frac{f_0}{\sqrt{m^2+1}}. \tag{3.17}$$

Here, m and f_0 are the actual chirp-rate and the initial frequency of the relevant chirp signal, respectively. The squared magnitude FrFT of the chirp signal $|S_\alpha(u)|^2$ can be written as

$$|S_\alpha(u)|^2 = S_\alpha(u) \times S_\alpha(u)^* = |A|^2 \sqrt{\csc^2(\alpha)} \iint_T E_{\alpha,u}(t,\upsilon) dt d\upsilon, \tag{3.18}$$

where the term $E_{\alpha,u}(t,\upsilon)$ is

$$E_{\alpha,u}(t,\upsilon) = e^{j\pi\left[(m+\cot(\alpha))\left(t^2-\upsilon^2\right)+(2f_0-2u\csc(\alpha))(t-\upsilon)\right]}.$$

The fist derivative of $|S_\alpha(u)|^2$ with respect to α is

$$\frac{\partial |S_\alpha(u)|^2}{\partial \alpha} = |A|^2 \sqrt{\csc^2(\alpha)} \iint_T \csc(\alpha) E_{\alpha,u}(t,\upsilon) B_{\alpha,u}(t,\upsilon) dt d\upsilon, \tag{3.19}$$

where the term $B_{\alpha,u}(t,\upsilon)$ is given by

$$B_{\alpha,u}(t,\upsilon) = j\pi \csc(\alpha)(\upsilon - t)(\upsilon + t - 2u\cos(\alpha)) - \cos(\alpha).$$

And the first derivative of $|S_\alpha(u)|^2$ with respect to u is

$$\frac{\partial |S_\alpha(u)|^2}{\partial u} = 2|A|^2 \pi \sqrt{\csc^2(\alpha)} \times \iint_T j \csc(\alpha)(\upsilon - t) E_{\alpha,u}(t,\upsilon) dt d\upsilon. \tag{3.20}$$

Computation of s_{11}

Taking the derivative of (3.19) again yields

$$\frac{\partial^2}{\partial \alpha^2}|S_\alpha(u)|^2 = -|A|^2\sqrt{\csc^2(\alpha)}\iint_T E_{\alpha,u}(t,\upsilon)Z_{\alpha,u}(t,\upsilon)dtd\upsilon, \tag{3.21}$$

where $Z_{\alpha,u}(t,\upsilon) = -1 + \csc(\alpha)(-2\cos(\alpha)\cot(\alpha) + \pi(\upsilon - t)(\csc^3(\alpha)(\upsilon + t - 2u\cos(\alpha))(\pi(\upsilon - t)(\upsilon + t - 2u\cos(\alpha)) + 2j\sin(2\alpha)) - 2ju))$. Replacing $\alpha = \overline{\alpha}$ and $u = \overline{u}$ as per (3.17), and then taking the integral results in

$$\frac{\partial^2}{\partial \alpha^2}|S_\alpha(u)|^2\Big|_{\substack{\overline{\alpha}\\ \overline{u}}} = -\frac{1}{90}|A|^2\sqrt{1+m^2}T^2\times(-90-180m^2+60f^2m^2\pi^2T^2+(1+m^2)^2\pi^2T^4),$$

The equation above can be rewritten as

$$s_{11} = -\frac{A^2T^6}{90}\pi^2\left(m^2+1\right)^{5/2} + \mathcal{O}(T^4), \tag{3.22}$$

where the additive term $\mathcal{O}(T^4)$ represents the terms that can be omitted when record length of T is large. The reader may refer to [120] for the $\mathcal{O}$-notation.

Computation of s_{22}

Taking the derivative of (3.20) again yields

$$\frac{\partial^2}{\partial u^2}|S_\alpha(u)|^2 = -4|A|^2\pi^2\sqrt{\csc^2(\alpha)}\times\iint_T \csc(\alpha)^2(\upsilon-t)^2E_{\alpha,u}(t,\upsilon)dtd\upsilon. \tag{3.23}$$

Replacing α, u with $\overline{\alpha}, \overline{u}$ as per (3.17) yields

$$\frac{\partial^2}{\partial u^2}|S_\alpha(u)|^2\Big|_{\substack{\overline{\alpha}\\ \overline{u}}} = -4|A|^2\pi^2\left(m^2+1\right)^{\frac{3}{2}}\iint_T (t-\upsilon)^2d\upsilon dt. \tag{3.24}$$

Taking the integral and simplifying it results in (3.25).

$$s_{22} = -\frac{2A^2T^4}{3}\pi^2(1+m^2)^{3/2}. \tag{3.25}$$

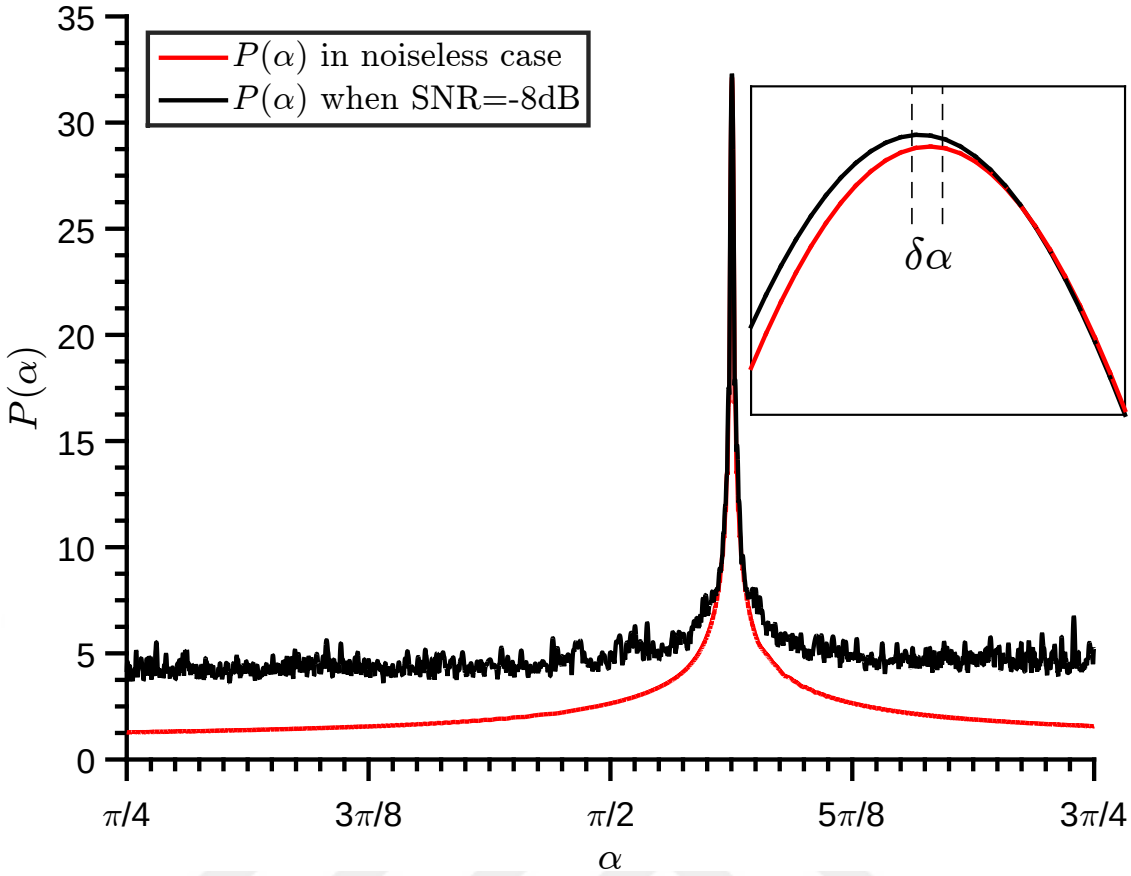

Figure 3.1 $\delta\alpha$ in α domain.

Computation of s_{12}

Taking the derivative of (3.20) with respect to α yields

$$\frac{\partial^2}{\partial\alpha\partial u}|S_\alpha(u)|^2 = -2|A|^2\sqrt{\csc^2(\alpha)}\iint_T Q_{\alpha,u}(t,\upsilon)E_{\alpha,u}(t,\upsilon)dtd\upsilon, \tag{3.26}$$

where $Q_{\alpha,u}(t,\upsilon) = \pi\csc^3(\alpha)(\upsilon-t)(\pi(\upsilon-t)(\upsilon+t-2u\cos(\alpha))+j\sin(2\alpha))$. Replacing the indexes with the optimum values and doing the integration results in (3.27).

$$s_{12} = -\frac{2A^2T^4}{3}\pi^2 f_0 m(1+m^2), \tag{3.27}$$

Theorem 1. *Estimation of* $\widehat{\alpha}_{opt}$ *in the FrFT domain is unbiased, since*

$$E\left\{\widehat{\alpha}_{opt}\right\} = \alpha_{opt}. \tag{3.28}$$

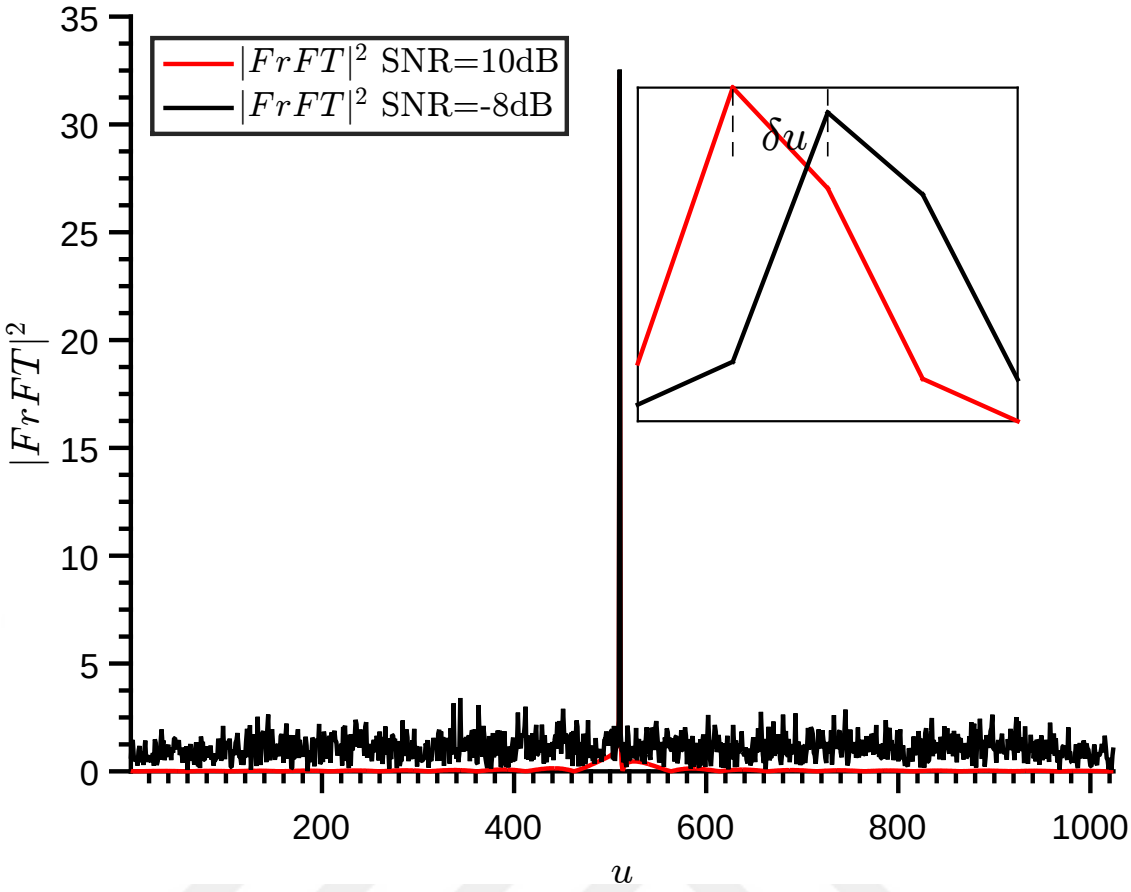

Figure 3.2 δu in u domain.

Proof. Taking the expected values of the both sides of (3.15) yields

$$E\{\delta\alpha\} = E\left\{\frac{s_1 s_{22} - s_2 s_{12}}{s_{11} s_{22} - s_{12}^2}\right\} = \frac{E\{s_1\} s_{22} - E\{s_2\} s_{12}}{s_{11} s_{22} - s_{12}^2}. \tag{3.29}$$

$E\{s_1\}$ is calculated by taking the expected value of the derivative of (3.8) with respect to α and can be expressed by

$$\begin{aligned} E\{s_1\} &= E\left\{\frac{\partial}{\partial\alpha}\left(S_\alpha(u) W_\alpha^*(u) + S_\alpha^*(u) W_\alpha(u)\right)\Big|_{\substack{\alpha_{opt} \\ u_{opt}}}\right\} \\ &= \frac{\partial}{\partial\alpha}\left(S_\alpha(u) E\left\{W_\alpha^*(u)\right\} + S_\alpha^*(u) E\{W_\alpha(u)\}\right)\Big|_{\substack{\alpha_{opt} \\ u_{opt}}} = 0, \end{aligned} \tag{3.30}$$

as the noise is assumed to have a mean of zero, i.e., $E\{W_\alpha(u)\} = 0$. When the same steps for the derivation of $E\{s_2\}$ are followed, it can also be shown that

$$E\{s_2\} = 0. \tag{3.31}$$

Substituting (3.30) and (3.31) demonstrates that

$$E\{\delta\alpha\} = 0. \tag{3.32}$$

Since $\widehat{\alpha}_{opt} = \alpha_{opt} + \delta\alpha$, then $E\{\widehat{\alpha}_{opt}\} = \alpha_{opt} + E\{\delta\alpha\}$. Since $E\{\delta\alpha\} = 0$, then the FrFT-domain maximum magnitude square estimator $\widehat{\alpha}_{opt}$ is unbiased, which proves (3.28). ■

Theorem 2. *Estimation of $\widehat{u}_{opt}$ in the FrFT domain is unbiased, since*

$$E\left\{\widehat{u}_{opt}\right\} = u_{opt}. \tag{3.33}$$

Proof. Taking the expected value of the both sides of (3.15) yields

$$E\{\delta u\} = \frac{E\{s_2\} s_{11} - E\{s_1\} s_{12}}{s_{11} s_{22} - s_{12}^2}. \tag{3.34}$$

Replacing (3.30) and (3.31) in the equations above yields

$$E\{\delta u\} = 0. \tag{3.35}$$

Since $\widehat{u}_{opt} = u_{opt} + \delta u$, then $E\{\widehat{u}_{opt}\} = u_{opt} + E\{\delta u\}$. Since $E\{\delta u\} = 0$, then the FrFT-domain maximum magnitude square estimator $\widehat{u}_{opt}$ is unbiased, which proves (3.33). ■

Theorems 1 and 2 prove that the FrFT-domain estimator (2.11) is unbiased. Variances of $\widehat{\alpha}_{opt}$ and $\widehat{u}_{opt}$ will be given by Theorems 3 and 4 as follows.

Theorem 3. *The variance of the FrFT domain estimator of the optimum FrFT angle is*

$$\mathrm{var}\left(\widehat{\alpha}_{opt}\right) = \frac{90\sigma^2}{A^2(1+m^2)^2\pi^2T^5} + \mathcal{O}\left(T^{-7}\right), \tag{3.36}$$

where the term $\mathcal{O}(T^{-7})$ represents the terms on the order of T^{-7} or lower and can therefore be omitted asymptotically.

Proof. Since $\widehat{\alpha}_{opt} = \alpha_{opt} + \delta\alpha$, variance of the estimate is $\mathrm{var}\left(\widehat{\alpha}_{opt}\right) = \mathrm{var}(\delta\alpha)$. As $E\{\delta\alpha\} = 0$, then $\mathrm{var}\left(\hat{\alpha}_{opt}\right) = E\left\{\delta\alpha^2\right\}$. Expanding (3.15) and taking the magnitude square yields

$$E\left\{\delta\alpha^2\right\} = \frac{E\left\{|s_1|^2\right\}|s_{22}|^2 + E\left\{|s_2|^2\right\}|s_{12}|^2}{|s_{11}s_{22} - s_{12}^2|^2} - \frac{E\left\{s_1s_2^*\right\}s_{22}s_{12}^* + E\left\{s_1^*s_2\right\}s_{22}^*s_{12}}{|s_{11}s_{22} - s_{12}^2|^2}. \tag{3.37}$$

Computation of $E\{|s_1|^2\}$

Taking the derivative of (3.8) with respect to α yields

$$\left|\frac{\partial\,\delta S_\alpha(u)}{\partial\alpha}\right|^2 = \left|S_\alpha(u)\frac{\partial W_\alpha^*(u)}{\partial\alpha} + S_\alpha^*(u)\frac{\partial W_\alpha(u)}{\partial\alpha} + \frac{\partial S_\alpha(u)}{\partial\alpha}W_\alpha^*(u) + \frac{\partial S_\alpha^*(u)}{\partial\alpha}W_\alpha(u)\right|^2. \tag{3.38}$$

$E\{|s_1|^2\}$ is the expected value of the above equation, which can be expressed by

$$\begin{aligned} E\left\{\left|\frac{\partial}{\partial\alpha}\delta S_\alpha(u)\right|^2\Big|_{\substack{\overline{\alpha}\\ \overline{u}}}\right\} = {} & 2\left|\frac{\partial}{\partial\alpha}S_\alpha(u)\right|^2 E\left\{|W_\alpha(u)|^2\right\}\Big|_{\substack{\overline{\alpha}\\ \overline{u}}} \\ & + 4Re\left\{S_\alpha(u)\frac{\partial}{\partial\alpha}S_\alpha^*(u)\,E\left\{W_\alpha(u)\frac{\partial}{\partial\alpha}W_\alpha^*(u)\right\}\Big|_{\substack{\overline{\alpha}\\ \overline{u}}}\right\} \\ & + 2\,|S_\alpha(u)|^2\,E\left\{\left|\frac{\partial}{\partial\alpha}W_\alpha(u)\right|^2\right\}\Big|_{\substack{\overline{\alpha}\\ \overline{u}}}. \end{aligned} \tag{3.39}$$

The right hand side terms of the equation above will be calculated starting with the first one. Let us first apply the definition (2.6) to the following signal

$$S_\alpha(u) = A_\alpha\int_{-\infty}^{+\infty} s(t)\,K_\alpha(t,u)\,dt, \quad w(t) = 0. \tag{3.40}$$

Taking the derivative with respect to α, substituting α and u with $\overline{\alpha}$ and $\overline{u}$ (given by

(3.17)), and doing the integration yields

$$\left.\frac{\partial S_\alpha(u)}{\partial \alpha}\right|_{\substack{\bar{\alpha}\\ \bar{u}}} = \frac{AT(m-j)e^{-j\pi\frac{f_0^2 m}{m^2+1}}}{12\sqrt{1+jm}} \times \left(12\pi f_0^2 + \pi\left(m^2+1\right)T^2 + 6jm - 6\right). \tag{3.41}$$

Taking its magnitude square gives

$$\left.\left|\frac{\partial S_\alpha(u)}{\partial \alpha}\right|^2\right|_{\substack{\bar{\alpha}\\ \bar{u}}} = \frac{1}{144}|A|^2T^2\sqrt{m^2+1} \times \left(\left(12\pi f_0^2 + \pi\left(m^2+1\right)T^2 - 6\right)^2 + 36m^2\right), \tag{3.42}$$

whereas by following the same steps

$$S_\alpha(u)|_{\substack{\bar{\alpha}\\ \bar{u}}} = AT\sqrt{1+jm}\exp\left(-j\pi\frac{mf_0^2}{1+m^2}\right), \tag{3.43}$$

is obtained. Therefore,

$$|S_\alpha(u)|^2\big|_{\substack{\bar{\alpha}\\ \bar{u}}} = |A|^2T^2\sqrt{(m^2+1)}. \tag{3.44}$$

The expected value of the noise magnitude square is calculated using

$$E\left\{W_\alpha(u)\,W_\alpha^*(u)\right\} = |A_\alpha|^2 \times \iint_T E\left\{w(t)\,w^*(\upsilon)\right\}K_\alpha(t,u)K_\alpha^*(\upsilon,u)\,dt\,d\upsilon. \tag{3.45}$$

Replacing $E\{w(t)\,w^*(\upsilon)\} = \sigma^2\delta(t-\upsilon)$ and replacing (3.17) yields

$$E\left\{|W_\alpha(u)|^2\right\} = \sigma^2\sqrt{1+m^2}\int_T dt = \sigma^2\sqrt{1+m^2}T. \tag{3.46}$$

The derivative of $W_\alpha(u)$ with respect to α can be expressed by

$$\frac{\partial W_\alpha(u)}{\partial \alpha} = \int_T w(t)\frac{\partial A_\alpha K_\alpha(t,u)}{\partial \alpha}dt = \int_T w(t)\left(\frac{\partial A_\alpha}{\partial \alpha}K_\alpha(t,u) + A_\alpha B_\alpha(t,u)K_\alpha(t,u)\right)dt, \tag{3.47}$$

where $\frac{\partial K_\alpha(t,u)}{\partial \alpha} = B_\alpha(t,u)K_\alpha(t,u)$ and $B_\alpha = -j\pi\csc^2(\alpha)\left(t^2+u^2-2tu\cos(\alpha)\right)$ have

been used. Therefore,

$$E\left\{\left|\frac{\partial}{\partial\alpha}W_\alpha(u)\right|^2\right\}\Bigg|_{\substack{\overline{\alpha}\\ \overline{u}}} = \sigma^2\int_T\left(\frac{\partial A_\alpha}{\partial\alpha}K_\alpha(t,u)+A_\alpha B_\alpha(t,u)K_\alpha(t,u)\right)\times \left(\frac{\partial A_\alpha^*}{\partial\alpha}K_\alpha^*(t,u)+A_\alpha^* B_\alpha^*(t,u)K_\alpha^*(t,u)\right)dt$$
$$= \sigma^2\int_T\left|\frac{\partial A_\alpha}{\partial\alpha}+A_\alpha B_\alpha(t,u)\right|^2\Bigg|_{\substack{\overline{\alpha}\\ \overline{u}}} dt. \tag{3.48}$$

Expanding, simplifying, and substituting using (3.17) produces

$$E\left\{\left|\frac{\partial}{\partial\alpha}W_\alpha(u)\right|^2\right\}\Bigg|_{\substack{\overline{\alpha}\\ \overline{u}}} = \frac{\sigma^2}{80}\pi^2\left(m^2+1\right)^{5/2}T^5+\mathcal{O}(T^3). \tag{3.49}$$

To find the final term of (3.39)

$$E\left\{W_\alpha(u)\frac{\partial}{\partial\alpha}W_\alpha^*(u)\right\}\Bigg|_{\substack{\overline{\alpha}\\ \overline{u}}} = \sigma^2\times\int_T A_\alpha K_\alpha(t,u)\left(\frac{\partial A_\alpha^*}{\partial\alpha}K_\alpha^*(t,u)+A_\alpha^* B_\alpha^*(t,u)K_\alpha^*(t,u)\right)dt,$$
$$= \sigma^2\int_T A_\alpha\frac{\partial A_\alpha^*}{\partial\alpha}+|A_\alpha^*|^2 B_\alpha^*(t,u)dt, \tag{3.50}$$

must be calculated. Expanding, taking the integral, simplifying, and substituting using (3.17) produces

$$E\left\{W_\alpha(u)\frac{\partial}{\partial\alpha}W_\alpha^*(u)\right\}\Bigg|_{\substack{\overline{\alpha}\\ \overline{u}}} = \frac{\pi\sigma^2\sqrt{1-jm}(m-j)\left(m^2+1\right)}{12\sqrt{1+jm}}T^3+\mathcal{O}(T). \tag{3.51}$$

By substituting (3.42), (5.26), (3.44), (3.49), (3.43), (3.41) and (3.51) into (3.39) will result in (3.66a).

Computation of $E\{|s_2|^2\}$

$E\{|s_2|^2\}$ is found by taking the derivative of (3.8) with respect to u and taking the expected value of the squared magnitude. Therefore, $E\{|s_2|^2\}$ can be expressed

by,

$$E\left\{\left|\frac{\partial}{\partial u}\delta S_\alpha(u)\right|^2\Big|_{\substack{\overline{\alpha}\\ \overline{u}}}\right\} = 2\left|\frac{\partial S_\alpha(u)}{\partial u}\right|^2 E\left\{|W_\alpha(u)|^2\right\}\Big|_{\substack{\overline{\alpha}\\ \overline{u}}} + 4Re\left\{S_\alpha(u)\frac{\partial}{\partial u}S_\alpha^*(u)\,E\left\{W_\alpha(u)\frac{\partial}{\partial u}W_\alpha^*(u)\right\}\Big|_{\substack{\overline{\alpha}\\ \overline{u}}}\right\} + 2\left|S_\alpha(u)\right|^2 E\left\{\left|\frac{\partial}{\partial u}W_\alpha(u)\right|^2\right\}\Big|_{\substack{\overline{\alpha}\\ \overline{u}}}. \tag{3.52}$$

The three right hand side terms of the above equation will be calculated starting with the first term. Taking the derivative of (3.40) with respect to u, substituting using the maximum value and integrating results in

$$\frac{\partial S_\alpha(u)}{\partial u}\Big|_{\substack{\overline{\alpha}\\ \overline{u}}} = -\frac{2j\pi Af\,m\sqrt{1+jm}Te^{-\frac{i\pi f^2 m}{m^2+1}}}{\sqrt{m^2+1}}. \tag{3.53}$$

Taking its magnitude square gives

$$\left|\frac{\partial S_\alpha(u)}{\partial u}\right|^2\Big|_{\substack{\overline{\alpha}\\ \overline{u}}} = \frac{4\pi^2|A|^2f^2m^2T^2}{\sqrt{m^2+1}}. \tag{3.54}$$

Regarding the noise terms, the derivative of $W_\alpha(u)$ with respect to u can be expressed by

$$\frac{\partial W_\alpha(u)}{\partial u} = \int_T A_\alpha w(t)\frac{\partial K_\alpha(t,u)}{\partial u}dt = \int_T A_\alpha w(t)H_\alpha(t,u)K_\alpha(t,u)dt, \tag{3.55}$$

where $H_\alpha(t,u) = j\pi(2u\cot(\alpha) - 2t\csc(\alpha))$. Therefore,

$$E\left\{\left|\frac{\partial}{\partial u}W_\alpha(u)\right|^2\right\} = \sigma^2A_\alpha \times \int_T w(t)\left(H_\alpha(t,u)K_\alpha(t,u)\right)\left(H_\alpha^*(t,u)K_\alpha^*(t,u)\right)dt, \tag{3.56}$$

Expanding, simplifying, and substituting by (3.17) produces

$$E\left\{\left|\frac{\partial}{\partial u}W_\alpha(u)\right|^2\right\}\Big|_{\substack{\overline{\alpha}\\ \overline{u}}} = \frac{\sigma^2}{3}\pi^2\left(m^2+1\right)^{3/2}T^3 + \mathcal{O}(T). \tag{3.57}$$

To find the final term of (3.52),

$$E\left\{W_\alpha(u)\frac{\partial}{\partial u}W_\alpha^*(u)\right\} = \sigma^2\int_T \left|A_\alpha H_\alpha(t,u)\right|^2 dt, \tag{3.58}$$

must be calculated. Expanding, integrating, simplifying, and substituting using (3.17) produces

$$E\left\{W_\alpha(u)\frac{\partial}{\partial u}W_\alpha^*(u)\right\}\Big|_{\substack{\alpha\\u}} = j2\pi\sigma^2 f_0 mT. \tag{3.59}$$

By substituting (3.54), (5.26), (3.44), (3.57), (3.43), (3.53) and (3.59) into (3.52) will result in (3.66b).

Computation of $E\left\{s_1 s_2^*\right\}$

$E\left\{s_1 s_2^*\right\}$ is the expected value of the derivative of (3.8) with respect to α times the complex conjugate of derivative of (3.8) with respect to u. Therefore, $E\left\{s_1 s_2^*\right\}$ can be expressed by,

$$\begin{aligned}
E\left\{\frac{\partial\delta S_\alpha(u)}{\partial u}\left(\frac{\partial\delta S_\alpha(u)}{\partial\alpha}\right)^*\Big|_{\substack{\alpha\\u}}\right\} &= 2Re\left\{\frac{\partial S_\alpha(u)}{\partial\alpha}\frac{\partial S_\alpha^*(u)}{\partial u}E\left\{|W_\alpha(u)|^2\right\}\Big|_{\substack{\alpha\\u}}\right.\\
&+ S_\alpha(u)\frac{\partial S_\alpha^*(u)}{\partial\alpha}E\left\{W_\alpha(u)\frac{\partial W_\alpha^*(u)}{\partial u}\right\}\Big|_{\substack{\alpha\\u}} + \frac{\partial S_\alpha(u)}{\partial u}S_\alpha^*(u)E\left\{\frac{\partial W_\alpha(u)}{\partial\alpha}W_\alpha^*(u)\right\}\Big|_{\substack{\alpha\\u}}\\
&+ \left.|S_\alpha(u)|^2 E\left\{\frac{\partial W_\alpha(u)}{\partial\alpha}\frac{\partial W_\alpha^*(u)}{\partial u}\right\}\Big|_{\substack{\alpha\\u}}\right\}.
\end{aligned} \tag{3.60}$$

The first term on the right hand side of the equation above can be calculated by multiplying the complex conjugate of (3.41) with (3.53) and (5.26) to obtain

$$\begin{aligned}
&2Re\left\{\frac{\partial S_\alpha(u)}{\partial\alpha}\frac{\partial S_\alpha^*(u)}{\partial u}E\left\{|W_\alpha(u)|^2\right\}\Big|_{\substack{\alpha\\u}}\right\} =\\
&\frac{\sigma^2|A|^2}{3}\times\pi T^3 f_0 m\sqrt{m^2+1}\left(12\pi f_0^2+\pi\left(m^2+1\right)T^2-6\right).
\end{aligned} \tag{3.61}$$

The second term on the right hand side of (3.60) can be calculated by multiplying the complex conjugate of (3.41) with (3.43) and (3.58)

$$\begin{aligned}
&2Re\left\{S_\alpha(u)\frac{\partial S_\alpha^*(u)}{\partial\alpha}E\left\{W_\alpha(u)\frac{\partial W_\alpha^*(u)}{\partial u}\right\}\Big|_{\substack{\alpha\\u}}\right\} =\\
&-\frac{\sigma^2|A|^2}{3}\pi T^3 f_0 m\sqrt{m^2+1}\left(\pi\left(m^2+1\right)T^2+12\pi f_0^2-6\right).
\end{aligned} \tag{3.62}$$

The third term on the right hand side of (3.60) can be calculated by using the complex

conjugate (3.43), (3.53), and the complex conjugate of (3.51)

$$2Re\left\{\frac{\partial S_\alpha(u)}{\partial u}S_\alpha^*(u)\,E\left\{\frac{\partial W_\alpha(u)}{\partial \alpha}W_\alpha^*(u)\right\}\Big|_{\substack{\alpha\\u}}\right\} = -\frac{\sigma^2|A|^2}{3}\pi T^3 f_0 m\sqrt{m^2+1}(-6+12f_0^2\pi+(1+m^2)\pi T^2). \tag{3.63}$$

To compute the last term on the right hand side of (3.60), we first calculate

$$2Re\left\{E\left\{\frac{\partial}{\partial \alpha}W_\alpha(u)\,\frac{\partial}{\partial u}W_\alpha^*(u)\Big|_{\substack{\alpha\\u}}\right\}\right\} = \pi T f_0 m\left(4\pi f_0^2+\pi(m^2+1)T^2-2\right), \tag{3.64}$$

by combining (3.47) and the complex conjugate of (3.55). Then, using (3.44) and multiplying with the equation above yields

$$2Re\left\{|S_\alpha(u)|^2\,E\left\{\frac{\partial W_\alpha(u)}{\partial \alpha}\frac{\partial W_\alpha^*(u)}{\partial u}\right\}\Big|_{\substack{\alpha\\u}}\right\} = \sigma^2|A|^2\times\pi T^3 f_0 m\sqrt{m^2+1}\left(4\pi f_0^2+\pi m^2T^2+\pi T^2-2\right). \tag{3.65}$$

Substituting (3.61),(3.62), (3.63), and (3.65) into the right hand side of (3.60) yields $E\{s_1 s_2^*\}$ as indicated by (3.66c).

$$E\left\{|s_1|^2\right\} = \frac{A^2T^7\sigma^2}{90}\pi^2(1+m^2)^3+\mathcal{O}(T^5). \tag{3.66a}$$

$$E\left\{|s_2|^2\right\} = \frac{2A^2T^5\sigma^2}{3}\pi^2(1+m^2)^2. \tag{3.66b}$$

$$E\left\{s_1s_2^*\right\} = E\left\{s_2s_1^*\right\} = \frac{2A^2T^5\sigma^2}{3}\pi^2 f_0 m(1+m^2)^{\frac{3}{2}}. \tag{3.66c}$$

Replacing (3.22),(3.25),(3.27) and (3.66) into (3.37) and simplifying yields,

$$E\left\{\delta\alpha^2\right\} = \frac{90\sigma^2}{A^2(1+m^2)^2\pi^2T^5}+\mathcal{O}\left(T^{-7}\right). \tag{3.67}$$

This concludes the proof, since $E\left\{\delta\alpha^2\right\} = \mathrm{var}\left(\widehat{\alpha}_{opt}\right)$. ■

Theorem 3 further demonstrates that the variance of a chirp-rate estimate based on a FrFT depends only on the actual chirp-rate and is independent of the initial frequency. Therefore, Theorem 3 demonstrates that, with less computational cost, the chirp-rate may be calculated in a one-dimensional search space.

Theorem 4. *The variance of the FrFT domain estimator of u_{opt} is*

$$\mathrm{var}\left(\widehat{u}_{opt}\right) = \frac{3\sigma^2}{2A^2(1+m^2)\pi^2T^3} + \mathcal{O}\left(T^{-5}\right), \tag{3.68}$$

where the term $\mathcal{O}(T^{-5})$ represents additional terms on the order of T^{-5} or lower and can be omitted asymptotically.

Proof. Since $\widehat{u}_{opt} = u_{opt} + \delta u$, the variance of the estimate is $\mathrm{var}\left(\widehat{u}_{opt}\right) = \mathrm{var}\left(\delta u\right)$. As $E\left\{\delta u\right\} = 0$, then $\mathrm{var}\left(\hat{u}_{opt}\right) = E\left\{\delta u^2\right\}$. Using (3.15),

$$E\left\{\delta u^2\right\} = \frac{E\left\{|s_2|^2\right\}|s_{11}|^2 + E\left\{|s_1|^2\right\}|s_{12}|^2}{|s_{11}s_{22} - s_{12}^2|^2} - \frac{E\left\{s_1^* s_2\right\} s_{11}s_{12}^* + E\left\{s_1 s_2^*\right\} s_{11}^* s_{12}}{|s_{11}s_{22} - s_{12}^2|^2}. \tag{3.69}$$

Replacing (3.22), (3.25),(3.27) and (3.66) in the equations above results in

$$E\left\{\delta u^2\right\} = \frac{3\sigma^2}{2A^2(1+m^2)\pi^2T^3} + \mathcal{O}\left(T^{-5}\right), \tag{3.70}$$

which concludes the proof since $E\left\{\delta u^2\right\} = \mathrm{var}\left(\widehat{u}_{opt}\right)$. ■

The performance of the initial frequency estimator is influenced by the actual value of the chirp-rate, as well as the optimal FrFT angle, as demonstrated by Theorem 4. Consequently, the performance of the FrFT index estimator depends on the performance of the optimum FrFT angle estimator. Since the chirp signal parameters are m and f_0, their estimation is important. In the following corollaries, we calculate the statistical performance of the FrFT-domain chirp-rate and initial frequency estimator using Theorems 1–4.

In the following corollaries, $X \overset{a}{\sim} \mathcal{N}(\mu, \mathrm{var}(X))$ denote that the random variable X is normal with an asymptotic mean of μ and an asymptotic variance of $\mathrm{var}(X)$. Furthermore, $\overset{a}{=}$ will denote *'asymptotically equal to'*.

Corollary 4.1. *The FrFT-domain chirp-rate estimator is asymptotically efficient, i.e, $\widehat{m} \overset{a}{\sim} \mathcal{N}(m, \mathrm{var}(m))$, where*

$$E\{\widehat{m}\} \overset{a}{=} m, \tag{3.71a}$$

$$\mathrm{var}(\widehat{m}) \overset{a}{=} \frac{90\sigma^2}{A^2\pi^2T^5}, \tag{3.71b}$$

which is also equal to the asymptotic CRLB [6, 115]. Thus, the FrFT domain chirp-rate estimator is asymptotically minimum variance and is unbiased.

Proof. Taking the expected value of both sides of (2.13a) yields

$$E\{\widehat{m}\} = E\{-\cot(\widehat{\alpha}_{opt})\} = -E\{\cot(\alpha_{opt} + \delta\alpha)\}. \tag{3.72}$$

Expanding this into a Taylor series around $\delta\alpha = 0$ and re-arranging it provides

$$E\{\widehat{m}\} = -\cot(\alpha_{opt}) + \left(1 + \cot^2(\alpha_{opt})\right) E\{\delta\alpha\} + \mathcal{O}\left(E\left\{\delta\alpha^2\right\}\right). \tag{3.73}$$

Substituting (3.32) and (3.67) into the equation above and using the fact that $m = -\cot(\alpha_{opt})$ produces

$$E\{\widehat{m}\} = -\cot(\alpha_{opt}) + \mathcal{O}\left(T^{-5}\right). \tag{3.74}$$

Therefore, (3.71a) has been proven, since the term $\mathcal{O}\left(T^{-5}\right)$ can be asymptotically ignored. Applying the well-known transformation of the parameters [119] property to (2.13a), the variance of $\widehat{m}$ can be found by using

$$\mathrm{var}(\widehat{m}) = \left(\frac{\partial m}{\partial \alpha_{opt}}\right)^2 \times \mathrm{var}\left(\widehat{\alpha}_{opt}\right). \tag{3.75}$$

Taking the derivative of (2.13a) yields $\frac{\partial m}{\partial \alpha_{opt}} = \csc^2(\alpha_{opt}) = 1 + m^2$. Replacing it in (3.36) produces

$$\mathrm{var}(\widehat{m}) = \frac{90\sigma^2}{A^2\pi^2T^5} + \mathcal{O}\left(T^{-7}\right), \tag{3.76}$$

which is asymptotically equal to (3.71b). That concludes the proof. ■

Corollary 4.2. *The FrFT-domain initial-frequency estimator is asymptotically efficient, i.e,* $\widehat{f_0} \overset{a}{\sim} \mathcal{N}(f_0, \mathrm{var}(f_0))$*, where*

$$E\left\{\widehat{f_0}\right\} \overset{a}{=} f_0, \tag{3.77a}$$

$$\mathrm{var}\left(\widehat{f_0}\right) \overset{a}{=} \frac{3\sigma^2}{2A^2\pi^2T^3}, \tag{3.77b}$$

which is also equal to the asymptotic CRLB [6, 115]. Thus, the FrFT domain initial frequency estimator is asymptotically minimum variance and is unbiased.

Proof. Taking the expected value of both sides of (2.13b) yields

$$E\left\{\widehat{f_0}\right\} = E\left\{\left(u_{opt} + \delta u\right)\csc\left(\alpha_{opt} + \delta\alpha\right)\right\}, \tag{3.78}$$

where $\widehat{\alpha}_{opt} = \alpha_{opt} + \delta\alpha$ and $\widehat{u}_{opt} = u_{opt} + \delta u$ have been replaced. Expanding this into

a Taylor series around ($\delta u = 0,\ \delta\alpha = 0$) and rearranging it produces

$$E\left\{\widehat{f_0}\right\} = u_{opt}\csc(\alpha_{opt}) + u_{opt}\cot(\alpha_{opt})\csc(\alpha_{opt})E\{\delta\alpha\} + \csc(\alpha_{opt})E\{\delta u\} + \mathcal{O}(E\{\delta\alpha^2\}) + \mathcal{O}(E\{\delta u^2\}).$$

Assuming that $E\{\delta\alpha\delta u\} = E\{\delta\alpha\}E\{\delta u\}$ and substituting (3.32), (3.35), (3.67), and (3.70) into the equation above yields

$$E\left\{\widehat{f_0}\right\} = f_0 + \mathcal{O}(T^{-5}), \tag{3.79}$$

where we have used the fact that $f_0 = u_{opt}\csc(\alpha_{opt})$. Therefore, (3.77a) has been proven, since the term $\mathcal{O}\left(T^{-5}\right)$ can be asymptotically ignored.

Applying the well-known transformation of the parameters [119] property, the variance of $\widehat{f_0}$ can be found by using

$$\mathrm{var}\left(\widehat{f_0}\right) = \left(\frac{\partial f_0}{\partial u_{opt}}\right)^2 \times \mathrm{var}\left(\widehat{u}_{opt}\right). \tag{3.80}$$

Taking the derivative of (2.13b), yields $\frac{\partial f_0}{\partial u_{opt}} = \csc(\alpha_{opt}) = \sqrt{1+m^2}$. Replacing it in (3.68) produces

$$\mathrm{var}\left(\widehat{f_0}\right) = \frac{3\sigma^2}{2A^2\pi^2T^3} + \mathcal{O}\left(T^{-5}\right), \tag{3.81}$$

which is asymptotically equal to (3.77b). Consequently, the proof is concluded. ■

The performance of FrFT-based LFM signal parameter estimation is ideal, as demonstrated by Corollaries 4.1 and 4.2. The actual initial frequency is a function of both α_{opt} and u_{opt}, while the actual chirp rate is only a function of α_{opt}. Theorem 3 shows that the variance of the estimated FrFT angle depends only on the actual chirp rate, so α_{opt} can be estimated independently of u_{opt}. This means that joint estimation of α_{opt} and u_{opt} in a two-dimensional search space is not necessary. Instead, the FrFT angle should be estimated first, followed by estimation of the optimum FrFT index using the estimated angle. Once α_{opt} has been estimated, the chirp rate can be estimated. Therefore, estimating α_{opt} and u_{opt} independently in single-dimensional search spaces is sufficient.

3.3 The Statistical Variances in the Discrete Mode

Up to this point, we have focused on the continuous case. However, for the sake of consistency in this thesis, we will now present the discrete-time counterpart

of the variances of the chirp-rate and initial frequency estimates, denoted by $\widehat{m}_d$ and $\widehat{f}_{0_d}$ respectively. To obtain the discrete-time variances, we need to multiply the continuous-time variances by $1/T_s$ [121], where T_s is the sampling rate. Assuming the presence of white Gaussian noise as a stationary ergodic process $x(t)$, which is a commonly encountered situation in real-world scenarios, its time average estimate can be expressed as:

$$\widehat{A}_x = \frac{1}{T}\int_0^T x(t)\,dt, \tag{3.82}$$

When T tends to infinity, the time-average value converges to the ensemble average. $\mathrm{T}\to\infty \Longrightarrow \widehat{A}_x = A_x$. And easily the variance will be

$$\sigma^2 = \lim_{T\to\infty} \frac{1}{T}\int_0^T \left|x(t) - \widehat{A}_x\right|^2 dt\ . \tag{3.83}$$

And for the discrete case $\widehat{A}_x = \frac{1}{N}\sum_{n=1}^{N} x(n)$ and the variance

$$\sigma^2 = \lim_{N\to\infty} \frac{1}{N}\sum_{n=1}^{N} \left|x(n) - \widehat{A}_x\right|^2 . \tag{3.84}$$

The transition from continuous mode to discrete mode

$$\sigma^2_{c\to d} = \lim_{T\to\infty} \frac{1}{NT_s}\int_0^T \left|x(t)\sum_{n=1}^{N}\delta(t-nT_s) - \widehat{A}_x\right|^2 dt = \lim_{T\to\infty}\frac{1}{NT_s}\lim_{N\to\infty}\frac{1}{N}\sum_{n=1}^{N}\left|x(n)-\widehat{A}_x\right|^2 = \frac{1}{T_s}\,\sigma^2. \tag{3.85}$$

When transitioning from continuous white noise to discrete white noise, a compensation factor of $\frac{1}{T_s}$ should be applied. Therefore, we can express the variances of the chirp-rate and initial frequency estimates in the discrete-time domain as follows:

$$\mathrm{var}(\widehat{m}_d) \overset{a}{=} \frac{90\sigma^2}{A^2 {T_s}^4 N^5}, \qquad \mathrm{var}\left(\widehat{f}_{0_d}\right) \overset{a}{=} \frac{6\sigma^2}{A^2 {T_s}^2 N^3}, \tag{3.86}$$

where N is the total number of samples for a discrete chirp signal as defined by

$$s[n] = A\exp\left[j\pi\left(m_d n^2 + 2f_{0_d} n\right)\right] + w[n], n = 0, 1, \cdots, N-1, \tag{3.87}$$

where $w[n]$ is a discrete circular additive white Gaussian noise with a variance of σ^2.

The derivations presented in this section rely on the assumption that T is sufficiently large, which is a reasonable assumption for practical applications. The outcomes demonstrate that utilizing the FrFT for estimating chirp parameters can provide

optimal values.

3.4 Discussion and Results

The following summarizes this chapter.

- Our study showed and proved that the FrFT-based chirp parameter estimator is asymptotically unbiased and capable of achieving the CRLB, demonstrating that the estimation of chirp parameters in the FrFT domain is asymptotically efficient. Although it is widely known that FrFT-domain chirp parameter estimation is optimal, we have provided a rigorous mathematical proof of this fact to support researchers interested in this field. Additionally, this proof has yielded valuable supplementary insights in the field of LFM parameter estimation. Through perturbation analysis of both the chirp-rate and initial frequency parameters, we have derived theoretical formulations for the continuous and discrete cases and obtained the asymptotic statistical characteristics (mean and variance) of the FrFT-based estimator. Our findings demonstrate that the FrFT-based estimator yields the optimum results when estimating chirp parameters.

- Our derivations showed that, for a FrFT-based chirp-rate estimator, the performance is reliant solely on the actual chirp-rate and SNR, rather than the initial frequency. This allows for the estimation of chirp-rate in a simplified one-dimensional search space, significantly reducing computational costs. In the case of the MLE for the AWGN, where the estimates are given by

$$\widehat{m},\widehat{f_0},\widehat{A} = \underset{\widehat{m},\widehat{f_0},\widehat{A}}{\operatorname{argmin}} \sum_{n=0}^{n=N-1} \left| \widetilde{s}(n) - \widehat{A}\exp\left[j\pi\left(\widehat{m}n^2 + 2\widehat{f_0}n\right)\right]\right|^2. \tag{3.88}$$

  By analyzing the MLE, it can be observed that it necessitates a three-dimensional search in the search-space, which typically has a computational complexity of $\mathcal{O}(N^3)$. In addition, all three parameters, namely A, f_0, and m, have to be jointly estimated in order to minimize the aforementioned equation. However, it is widely acknowledged that there are rapid techniques for the MLE that enable the amplitude to be estimated separately, thereby reducing the search space from three dimensions to two dimensions. Not only does the FrFT-based estimator have lower computational complexity, but it also possesses other valuable properties, such as the independence and order of parameter estimation. The FrFT allows for separate estimation of the chirp rate using a one-dimensional search without requiring the estimation of the other parameter, f_0. This conclusion was drawn from the conducted perturbation analysis, where it was

found that the variance of both $\delta\alpha$ and δu only depends on the chirp rate m, as seen in equations (3.67) and (3.70). Hence, for applications solely concerned with the chirp rate, the FrFT can be used as it provides a fast and asymptotic estimator. The following briefly summarize the above discussion.

  - Theorem 3 indicates that the variance of the FrFT angle is solely determined by the original chirp rate of the signal and not by the initial frequency.
  - Since the variance of the FrFT angle (var(α_{opt})) only depends on the original chirp rate of the signal, the search space can be reduced to a single dimension, which significantly decreases the computational cost.
  - The variance of the FrFT index (var(u_{opt})) relies on the actual value of the chirp rate. Therefore, to accelerate the algorithm's speed, the chirp rate should be estimated beforehand.

- The validity of the assumption that the FrFT-based estimator is equivalent to the MLE depends on the value of T. When T is sufficiently large, the rotation property of the FrFT can concentrate the signal power relative to the noise level. However, as there is an SNR breakdown threshold that specifies the minimum value of SNR required for the estimator to work properly, there is a breakdown threshold of T beyond which the concentration ability of the FrFT is no longer effective. Through perturbation analysis, several key findings regarding the T breakdown threshold were obtained. Equations (3.74), (3.76), (3.79), and (3.81) provide the minimum T required for the mean and variance to be considered asymptotically efficient. In the case of small T, the results are affected by the $\mathcal{O}$ term, which can be deduced from the equations. The breakdown T can be determined by considering the terms that were previously ignored. Additionally, the variance was derived for both continuous and discrete cases, providing an asymptotic bound in these scenarios.

4
Estimating Chirp-Rates Using The FrFT And The GSS Algorithm

4.1 Introduction

A new algorithm has been proposed in this work to estimate the chirp-rate of mono and multi-component LFM signals at a low computational cost and with high precision, using an efficient iterative technique in the FrFT domains. The approach is based on the well-known golden section search (GSS) algorithm, which is known to require the lowest calculations in the search space for a uni-modal cost function, according to [122]. In [114], an initial version of the GSS-based algorithm was proposed for estimating the chirp rate of mono-component LFM signals. The proposed algorithm was also compared with Zheng and Shi's method [105], and it was shown to be faster and more accurate. In [104], this concept was extended to the scenario of multi-component LFM signals, and the optimal number of iterations for achieving asymptotic CRLB convergence with the GSS algorithm was determined, showing that more iterations are not necessary for better estimate performance, leading to a reduction in computational cost. To the authors' knowledge, the algorithm presented here has the lowest computational cost among existing methods.

4.2 Estimating Chirp-Rate for Mono-Component LFM Signals Using the FrFT and the GSS Algorithm

In order to avoid the high computational cost of computing the FrFT for each value of α, an alternative approach is needed. One such approach is to use the GSS algorithm to find the maximum magnitude of the FrFT domains, or the maximum value of $P(\alpha)$, which in turn leads to the optimal angle. The GSS algorithm is a well-known method for finding the maximum or minimum of a unimodal continuous function over a given interval without the need for derivative calculations [123]. By computing the FrFT at only a few carefully chosen angles, the GSS algorithm accelerates the search process.

The algorithm's error tolerance determines the accuracy of the final result. Computing the FrFT at a limited number of angles significantly reduces the processing expense compared to computing the FrFT for each angle.

The GSS algorithm evaluates the function $P(\alpha)$ at the boundaries of the search interval, denoted by $[\alpha_a, \alpha_b]$. Two points α_1 and α_2 are then selected within this interval using these two equations:

$$\alpha_1 = \alpha_b - r\,(\alpha_b - \alpha_a), \qquad \alpha_2 = \alpha_a + r\,(\alpha_b - \alpha_a), \tag{4.1}$$

Next, the function is evaluated at these two points. If $P(\alpha_1) < P(\alpha_2)$, the search interval is narrowed down to a new range of $(\alpha_1, \alpha_b]$. Similarly, if $P(\alpha_1) > P(\alpha_2)$, the new range containing the maximum is set to $[\alpha_a, \alpha_2)$. If $P(\alpha_1) = P(\alpha_2)$, then the maximum lies in the new range (α_1, α_2) since the two points are on either side of the maximum. Once the range is updated, a single new point is determined using the golden ratio, and the other point calculated in the previous iteration is reused. For example, if the new range after the first iteration is $(\alpha_1, \alpha_b]$, then the new point in the second iteration is determined to be $\alpha_3 = \alpha_1 + r(\alpha_b - \alpha_1)$. Thus, only one new interior point is required, and the function is evaluated only once more instead of twice at each iteration. The process is repeated until the search interval is less than the required precision of $0 < \varepsilon \ll 1$. The most recently updated point is used as the maximum value index. The advantage of the GSS is that one of the two test points is reused each time the range is updated, resulting in fewer calculations and a more efficient search. The steps of the GSS algorithm have been illustrated in Figure 4.1.

4.2.1 The Validity of the GSS in the Mono-Component LFM Case

In Fig. 4.2, we observe a plot of $P(\alpha)$ for a chirp signal with a chirp rate of 0.3 in the absence of noise. The first eight steps of GSS are also shown, where $P(\alpha)$ is evaluated. The plot demonstrates that $P(\alpha)$ in the absence of noise is nearly unimodal.

In noisy situations, $P\,(\alpha)$ may not be perfectly unimodal. We will use the notation $\widetilde{P}(\alpha)$ to refer to the function $P\,(\alpha)$ in noisy cases in the upcoming chapters. Despite the noise, the GSS algorithm can still perform very well in noisy environments due to two reasons. Firstly, the rapid entry of search steps into the high-energy region of $\widetilde{P}(\alpha)$, which is the area surrounding the α_{opt}. In the next chapters, we will use the term "almost noise-free region" or "signal-dominant area" to refer to the same area. According to [53], the normalized chirp-rate values after sampling range between $-1 \leq m \leq 1$, which corresponds to $\pi/4 \leq \alpha_{opt} \leq 3\pi/4$ for the rotation angles. Therefore, the first search space is limited to the range $\alpha \in [\pi/4, 3\pi/4]$. When the

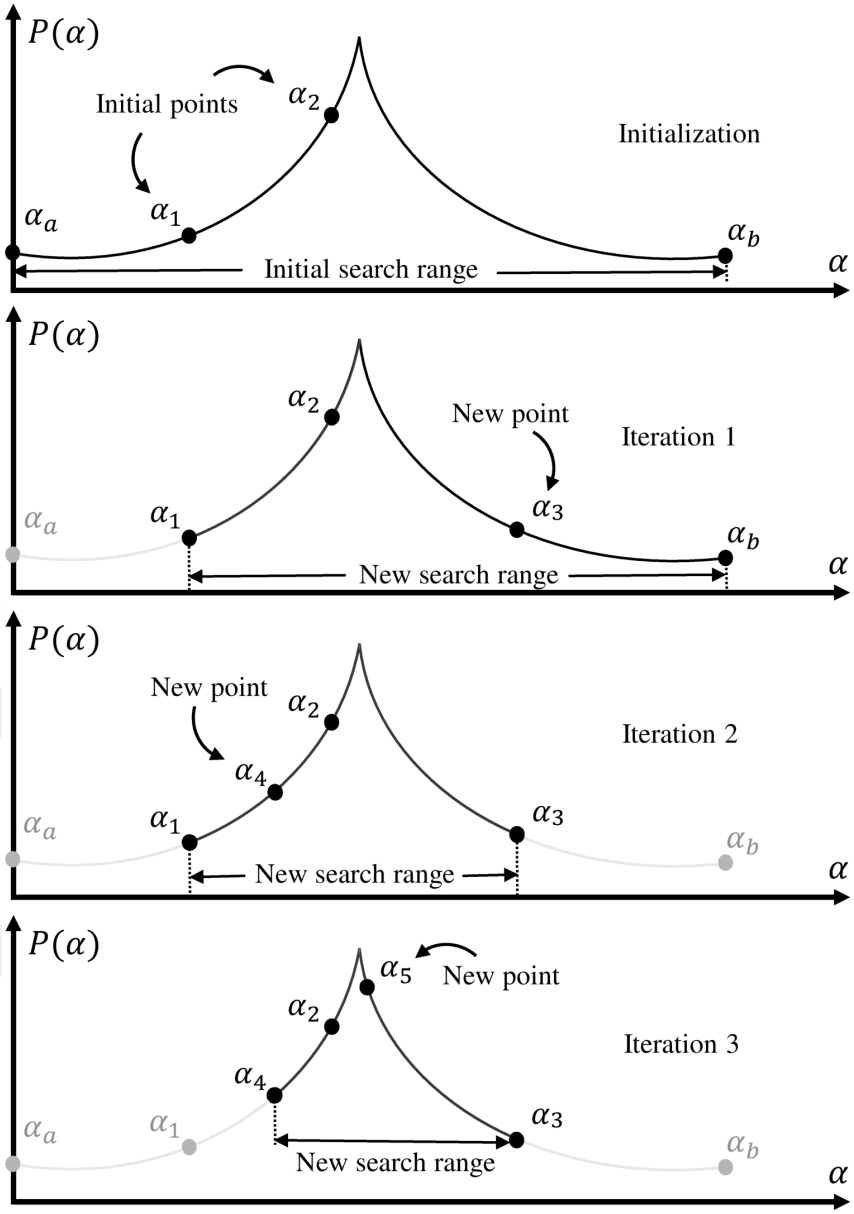

Figure 4.1 The GSS algorithm.

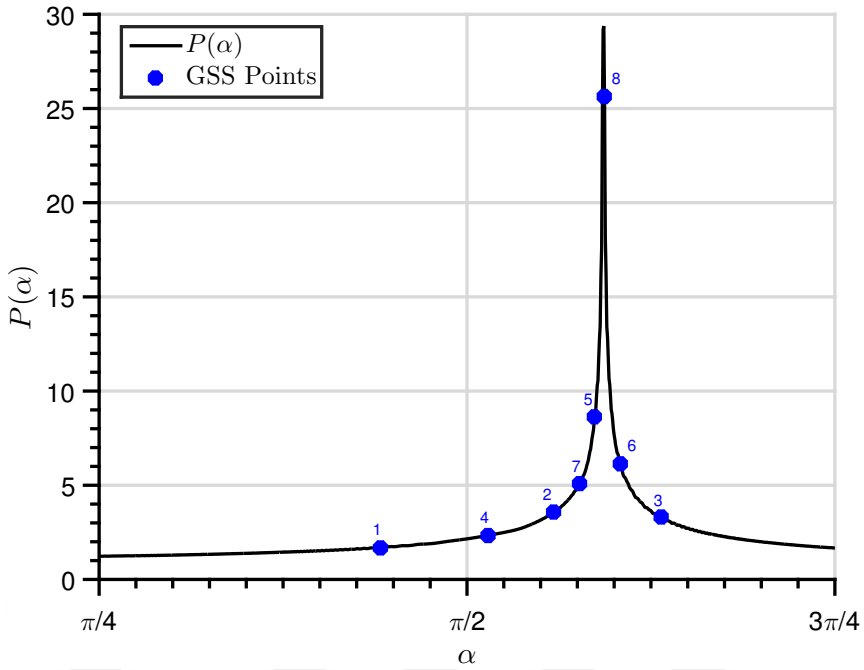

Figure 4.2 Illustration of a sample $P(\alpha)$ for a chirp function in a noiseless environment. Computed GSS values are shown in the figure.

GSS algorithm begin with this search space, it rapidly moves into the signal-dominant area. The second reason is that the signal-dominant area is relatively free of noise and that due to the rotational property of FrFT in the time-frequency plane, where the chirp energy is concentrated in this area, and the noise energy is not. This maintains the unimodal property of $\widetilde{P}(\alpha)$ in this region. Consequently, it enters an almost unimodal climb region. As a result, the GSS algorithm chooses the initial points in an area where the noise has a minimal impact compared to other regions. The iterative process is repeated until the search interval reaches a predetermined tolerance value, typically a very small positive number ε, where $\varepsilon \ll 1$. In the presence of noise with an SNR of -6 dB and a mono-component chirp signal, Figure 4.3 shows a sample of GSS points. There is a noise floor for $\widetilde{P}(\alpha)$, similar to the power spectrum of a noisy signal. However, above this noise floor, $\widetilde{P}(\alpha)$ is practically noise-free. The noise floor value is still very low due to the rotation property of the FrFT, as observed from the figure. Therefore, the area around α_{opt} can be considered virtually uni-modal, and noise floor value is very low. Moreover, only a relatively small number of iterations are required for the GSS algorithm to enter the almost noise-free region. Further elaboration on this point will be provided in the next chapter. As depicted in the figure, the search interval $\alpha \in [\pi/4, 3\pi/4]$ contains mostly noise-free regions of $\widetilde{P}(\alpha)$, allowing the GSS algorithm to swiftly enter the almost-noise-free area. This property makes the proposed GSS algorithm a robust and efficient tool for estimating the optimum FrFT angle that corresponds to the maximum of $\widetilde{P}(\alpha)$.

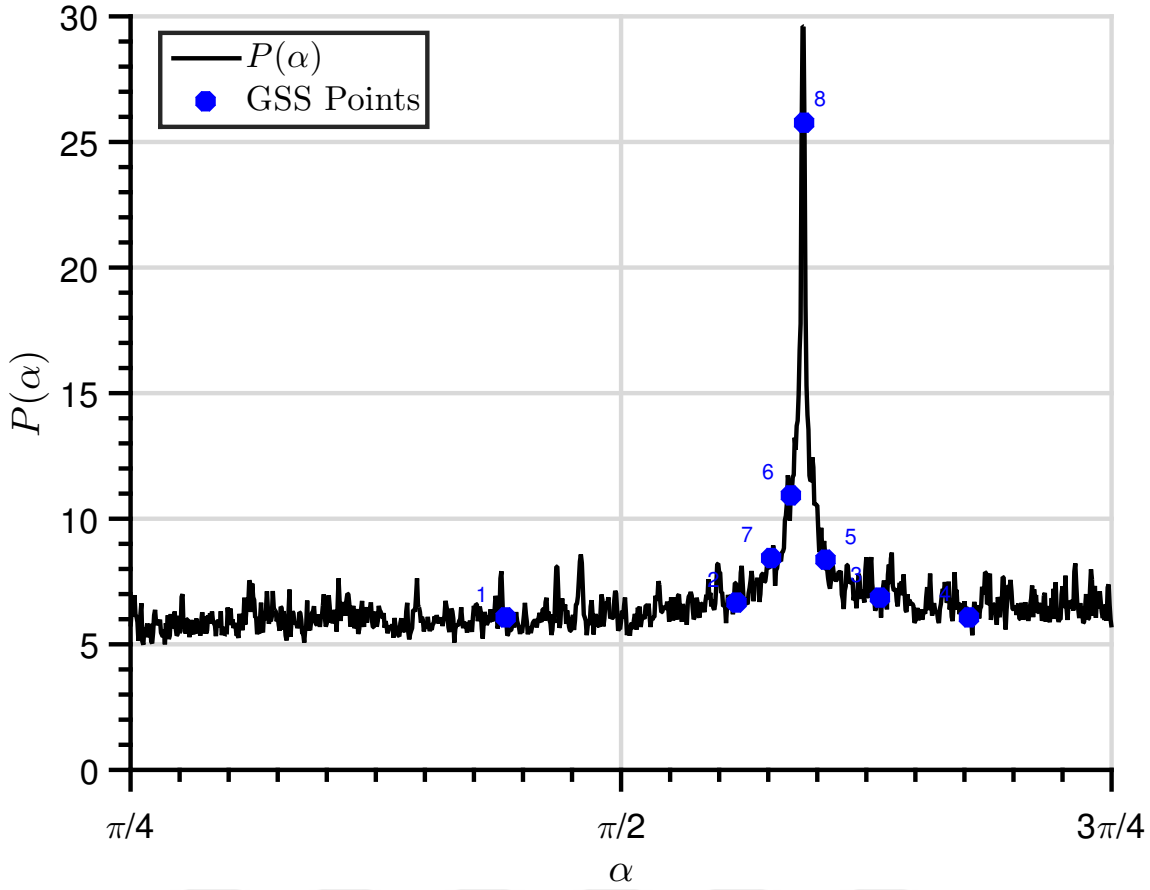

Figure 4.3 Sample GSS points for a noisy signal when the $SNR = -6$dB.

Using a rectangular window can introduce sidelobes in the FrFT domain, but these sidelobes will not appear in the $\widetilde{P}(\alpha)$ domain. The proposed method involves taking the FrFT of the signal $\widetilde{S}_{\alpha}(u) = |\mathscr{F}^{\alpha}\{\widetilde{s}(t)\}(u)|^2$. However, due to the limited observation duration of T, sidelobes may appear in $\widetilde{S}_{\alpha}(u)$. To mitigate this, we take the absolute square of $\widetilde{S}_{\alpha}(u)$ and then compute its maximum value, resulting in $\widetilde{P}(\alpha) = \max_u \left\{|\mathscr{F}^{\alpha}\{\widetilde{s}(t)\}(u)|^2\right\}$.over all values of u. Therefore, even if sidelobes are present in $\widetilde{S}_{\alpha}(u)$, they will not affect the maximum value of its magnitude square.

Algorithm 1 summarizes the above algorithm in which the GSS is applied on $\widetilde{P}(\alpha)$ for a signal $\widetilde{s}(t)$, where $[\alpha_a \ \alpha_b]$ is the initial search interval.

Algorithm 1 The proposed GSS algorithm for estimating the chirp-rate of a single chirp.

Initialize:
$\alpha_1 \leftarrow \alpha_b - r(\alpha_b - \alpha_a)$,
$\alpha_2 \leftarrow \alpha_a + r(\alpha_b - \alpha_a)$,
Set the dummy variables:
$v_1 \leftarrow \max\left\{|\mathscr{F}^{\alpha_1}\{\widetilde{s}(t)\}(u)|^2\right\}$,
$v_2 \leftarrow \max\left\{|\mathscr{F}^{\alpha_2}\{\widetilde{s}(t)\}(u)|^2\right\}$,
while 1 **do**
  if $v_1 < v_2$ **then**
    $\alpha_a \leftarrow \alpha_1$
    $\alpha_1 \leftarrow \alpha_2$
    $\alpha_2 \leftarrow \alpha_a + r\ (\alpha_b - \alpha_a)$
    $v_1 \leftarrow v_2$
    $\widehat{\alpha}_{opt} \leftarrow \alpha_2$
    if $|\alpha_b - \alpha_a| \leq \varepsilon$ **then**
      break
    end if
    $v_2 \leftarrow \max\left\{|\mathscr{F}^{\alpha_2}\{\widetilde{s}(t)\}(u)|^2\right\}$
  else
    $\alpha_b \leftarrow \alpha_2$
    $\alpha_2 \leftarrow \alpha_1$
    $\alpha_1 \leftarrow \alpha_b - r(\alpha_b - \alpha_a)$
    $v_2 \leftarrow v_1$
    $\widehat{\alpha}_{opt} \leftarrow \alpha_1$
    if $|\alpha_b - \alpha_a| \leq \varepsilon$ **then**
      break
    end if
    $v_1 \leftarrow \max\left\{|\mathscr{F}^{\alpha_1}\{\widetilde{s}(t)\}(u)|^2\right\}$
  end if
end while
return $\widehat{m} \leftarrow -\cot\left(\hat{\alpha}_{opt}\right)$

4.2.2 The Computational Cost

The total iteration number is given by

$$I = \left\lceil \frac{\log[\varepsilon/(\alpha_b - \alpha_a)]}{\log(r)} \right\rceil, \tag{4.2}$$

where $\lceil \cdot \rceil$ is the ceiling function. At each iteration, we compute FrFT once. As the computational cost of FrFT is $\mathcal{O}(N \log N)$ [101] for a signal of length N, the total computational complexity of GSS is $\mathcal{O}(I \times N \log N)$.

4.2.3 Simulations

Experiments were conducted to demonstrate the effectiveness of the proposed algorithm for the chirp-rate estimation problem. A chirp signal was created using the following parameters: $m = 0.4$, sampling frequency $F_s = \sqrt{N}$, and initial frequency $f_0 = -0.1$. The search interval for the GSS was set to $[\pi/4, 3\pi/4]$ with a tolerance of $\varepsilon = \pi/2 \times 10^{-4}$. The SNR was varied from -15dB to 20dB in increments of 1dB to execute the experiment. For each SNR value, 200 Monte Carlo runs were performed. The MSE is

$$MSE = \frac{1}{\mathrm{C}} \sum_{i=1}^{\mathrm{C}} (\widehat{m}_i - m)^2, \tag{4.3}$$

where $\widehat{m}_i$ is the estimated chirp rate at i-th Monte Carlo simulation and C is the total number of Monte-Carlo simulations at each SNR. In the experimental results, Fig. 4.4 illustrates the performance of the proposed algorithm for a signal length of 256, Fig. 4.5 for a signal length of 512, and Fig. 4.6 for a signal length of 1024 samples. In each case, we compare our results with the CRLB [116] and Zheng and Shi's MACF algorithm [105]. The results indicate that the proposed GSS algorithm achieves almost the same accuracy as the CRLB for SNR values as low as -7 dB, which is the SNR breakdown threshold in this case. The MACF algorithm, on the other hand, has a higher SNR breakdown threshold of -4 dB. When using the same settings as in [105], the MACF method has a computational complexity of $\mathcal{O}(63 \times N \log N)$ with the exception of the tolerance $\varepsilon = \pi/2 \times 10^{-4}$, while the proposed GSS method has a computational complexity of $\mathcal{O}(21 \times N \log N)$. Thus, for the same accuracy or tolerance level, the GSS method is three times faster than the MACF. Based on these findings, we conclude that the proposed GSS method is not only faster but also more accurate and reliable.

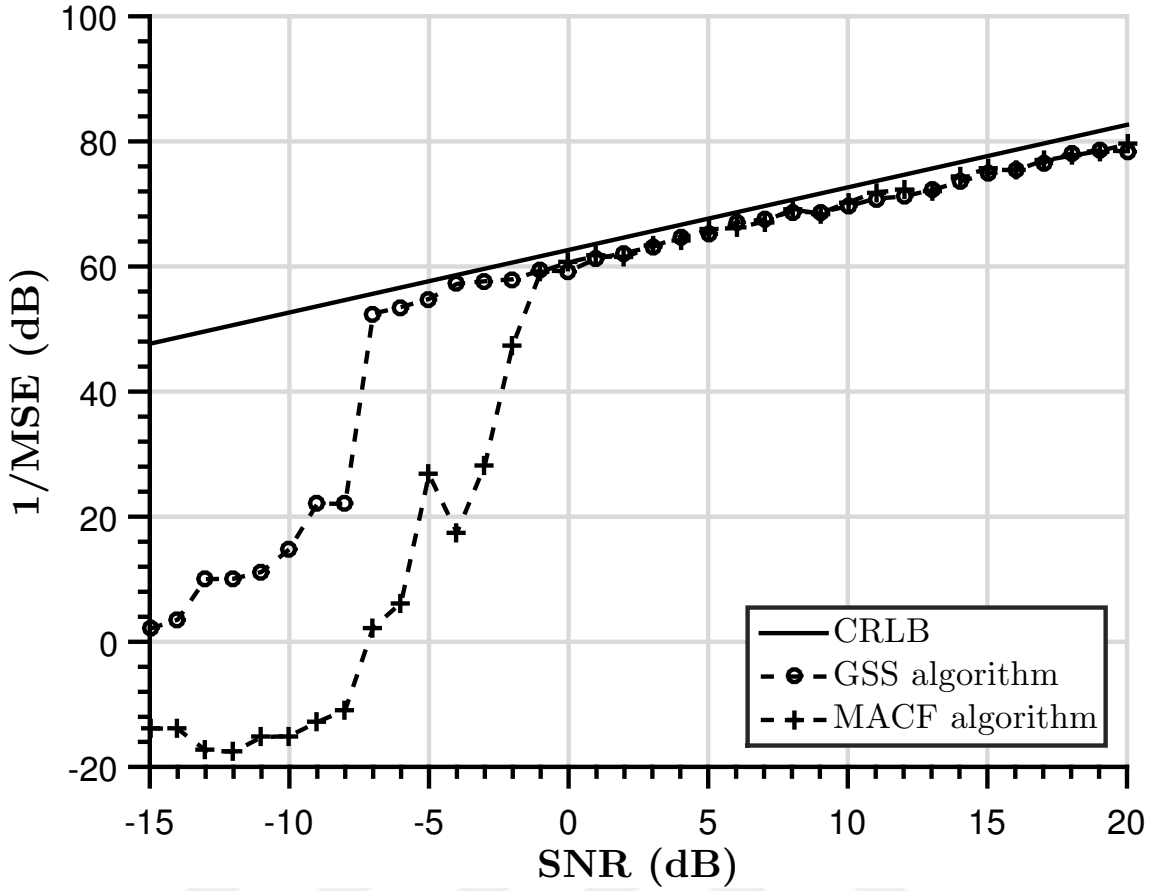

Figure 4.4 The performance of the proposed algorithm for $N = 256$.

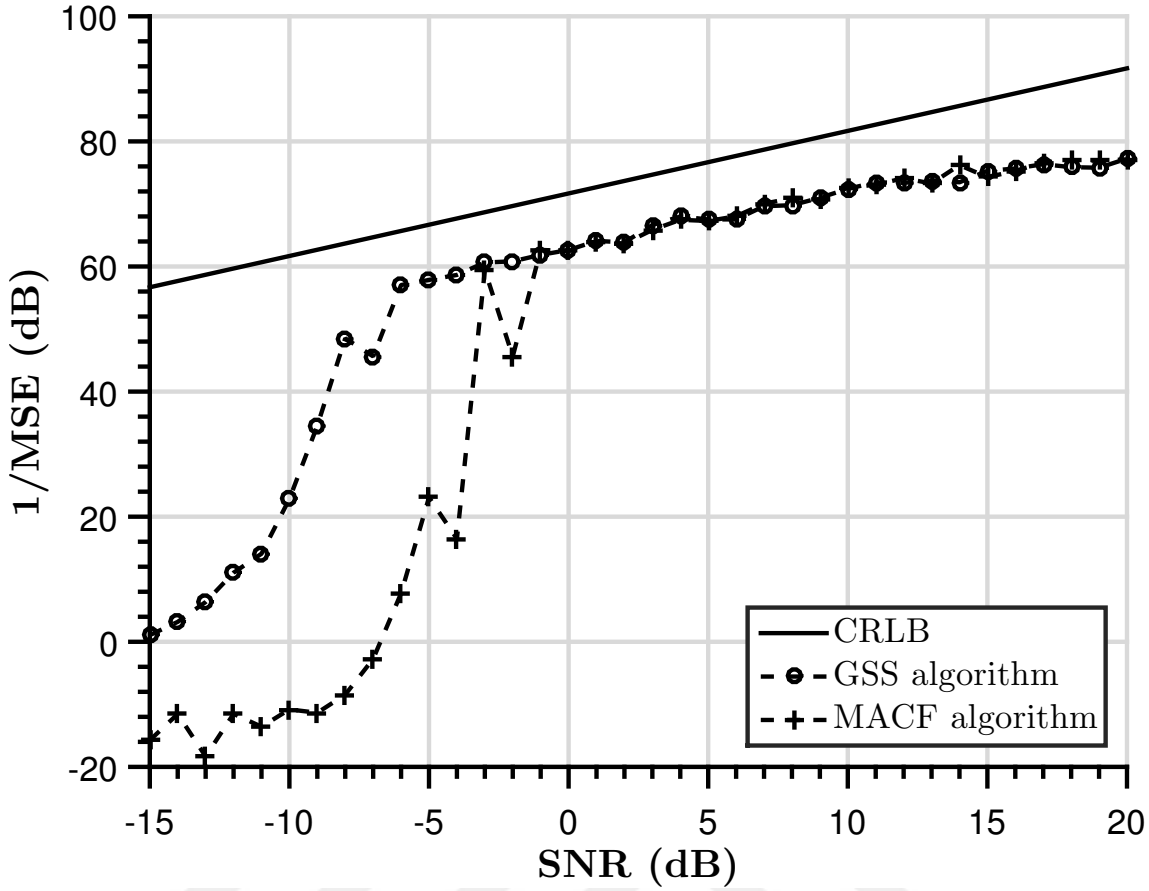

Figure 4.5 The performance of the proposed algorithm for $N = 512$.

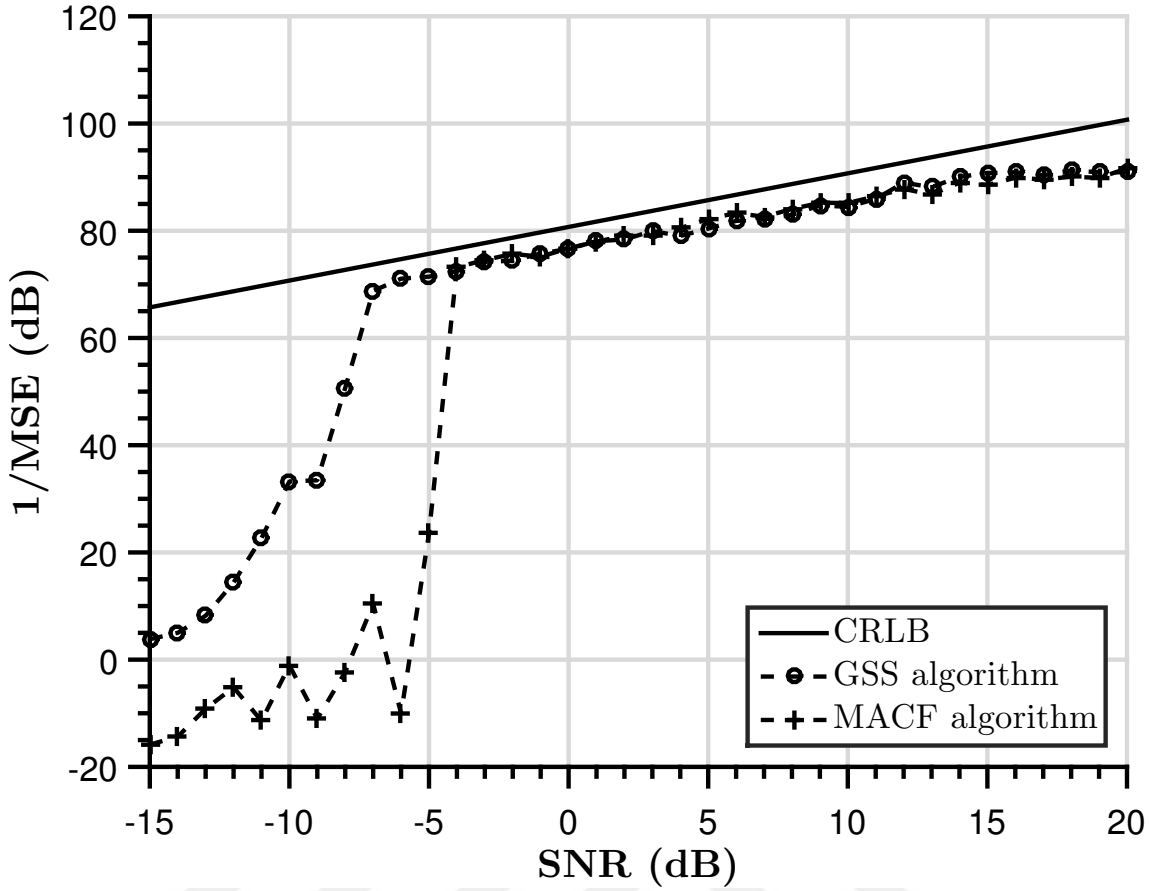

Figure 4.6 The performance of the proposed algorithm for $N = 1024$.

4.2.4 Results and Discussion

The GSS algorithm is a suitable method for estimating the chirp-rate due to several reasons. Firstly, as shown in Fig. 4.1, the function $P(\alpha)$ is nearly unimodal, making the GSS an effective tool for determining the maximum value. Secondly, the GSS is an optimal search algorithm that requires only a few iterations, resulting in lower computational costs compared to other search methods. The proposed technique utilizes the GSS algorithm to identify the maximum value of the FrFT and determine the optimal angle for chirp rate estimation in noisy environments. Simulation results demonstrate the effectiveness of the proposed algorithm, which achieves near CRLB performance even for SNR values as low as -7dB, while requiring less computational cost. Comparing the GSS with the MACF method, the former is faster, more accurate, and more reliable.

4.3 Estimating Chirp-Rates for Multi-Component LFM Signals Using the FrFT and the GSS Algorithm

In this section, we extend and generalize the concept of parameter estimation for mono-component chirp signals to the K-component scenario using the signal $\widetilde{s}_K(t)$. Furthermore, we can extend the function $P(\alpha)$ to handle noisy multi-component LFM signals $\widetilde{s}_K(t)$ as follows:

$$\widetilde{P}_K(\alpha) = \max_{\alpha\in[0,\pi]} \left\{ \left| \mathscr{F}^{\alpha} \left\{ \widetilde{s}_K(t) \right\}(u) \right|^2 \right\}. \tag{4.4}$$

As observed in the mono-component case, $P(\alpha)$ has a single peak corresponding to α_{opt}. In the general case of a noisy multi-component LFM signal $\widetilde{P}_K(\alpha)$ contains K local maxima corresponding to the K chirp-rates present in the signal [106]. For instance, in the case of a bi-component chirp signal, the function $\widetilde{P}_2(\alpha)$ will have two local maxima at the indices $\alpha_{opt_1} = \arctan(m_1) + \frac{\pi}{2}$ and $\alpha_{opt_2} = \arctan(m_2) + \frac{\pi}{2}$, respectively. By generalizing to K components, it can be concluded that, $\widetilde{P}_K(\alpha)$ has K local maxima at $\alpha_{opt_i} = \arctan(m_i) + \frac{\pi}{2}$, for $i = 1, \cdots, K$.

When using the GSS method on $\widetilde{P}_K(\alpha)$, it randomly selects one of the local maxima corresponding to, for instance, $\widehat{m}_1$. Once the first chirp-rate is determined, the task of estimating the associated initial frequency $\widehat{f}_1$ becomes simpler, as it involves calculating the frequency of a sinusoidal signal. This can be achieved by performing a de-chirping process, which projects the signal onto the subspace spanned by the complex exponential of the estimated chirp-rate. Any single sinusoidal estimation algorithm, such as the Aboutanios and Mulgrew estimator (AME) [124] or the High-Accuracy Quadratic Sine Estimator (HAQSE) [125], can then be used to obtain

an accurate estimation for the initial frequency.

After estimating the chirp-rate and the initial frequency $\{\widehat{m}_1, \widehat{f}_1\}$, the amplitude can be estimated by

$$\widehat{A}_1 = \frac{1}{N}\sum \widetilde{s}_K(t) \times \exp\left[j\pi\left(-\widehat{m}_1 t^2 - 2\widehat{f}_1 t\right)\right]. \tag{4.5}$$

Finally, the $(K-1)$ component chirp signal can be written as

$$\widetilde{s}_{K-1}(t) = \widetilde{s}_K(t) - \widehat{A}_1 \exp\left[j\pi\left(\widehat{m}_1 t^2 + 2\widehat{f}_1 t\right)\right]. \tag{4.6}$$

Once the number of components in a multi-component chirp signal is known, the estimation of all the chirp-rates and frequency shifts can be straightforward by applying the GSS method K times. However, if the number of components is unknown, the procedure can be repeated iteratively until the detected peak value falls below a certain threshold, which can indicate the number of components. The value of this threshold depends on the level of noise in the signal and can be determined using appropriate statistical methods. The pseudo-code for the algorithm is provided as follows.

Algorithm 2 The proposed GSS-based algorithm for estimating the chirp-rates of a K-component chirp.

Initialize:
$\widetilde{s}(t) \leftarrow \widetilde{s}_K(t)$,
for $i = 1$ to K **do**
  $\widehat{m}_i \leftarrow \text{GSS}(\widetilde{s}(t))$, *%Use Alg. 1 to estimate chirp-rate*
  $\widehat{f}_i \leftarrow \text{AME}(\widetilde{s}(t) \times e^{-j\pi\widehat{m}_i t^2})$, *%Use [124] to est. freq.*
  $\widehat{A}_i \leftarrow \frac{1}{N}\sum \widetilde{s}(t) \times e^{-j\pi\left(\widehat{m}_i t^2 + 2\widehat{f}_i t\right)}$,
  $\widetilde{s}(t) \leftarrow \widetilde{s}(t) - A_i e^{j\pi\left(\widehat{m}_i t^2 + 2\widehat{f}_i t\right)}$,
end for
return $\widehat{m} = [\widehat{m}_1, \widehat{m}_2, \cdots, \widehat{m}_K]^T$

In the presence of multiple components, there is a possibility of getting trapped in a local maximum due to the nonlinear interaction between the components. This issue can even arise in a noiseless scenario and is a common problem with fast search algorithms. To address this issue, the search space's start and end points can be adjusted when a false peak is detected. Alternatively, increasing the signal length may also help to mitigate the problem.

4.3.1 The Optimum Number of Iterations

When the GSS algorithm's search interval becomes smaller than ε, the iteration ends. The accuracy of the GSS algorithm can be adjusted by changing the error tolerance,

which depends on the application. The chosen value of ε, where $\text{var}(\widehat{\alpha}) \sim \varepsilon^2$, has a direct impact on the estimator's performance. The lower bound of the variance of $\widehat{\alpha}$ is $\mathcal{O}(N^{-5})$ because the CRLB of $\widehat{\alpha}$ is also $\mathcal{O}(N^{-5})$. Therefore, if ε^2 is of a lower order than $\mathcal{O}(N^{-5})$, no additional advantage can be gained asymptotically. To ensure that the algorithm converges and achieves the CRLB, the number of iterations should stop when ε^2 reaches an order of $\mathcal{O}\left(N^{-5}\right)$.

$$\varepsilon^2 \sim \mathcal{O}(N^{-5}). \tag{4.7}$$

There are countless options for ε that satisfy the relation shown above. But out of convenience, we choose

$$\varepsilon = \frac{\pi}{2} \times N^{-3}. \tag{4.8}$$

To simplify the result and incorporate the conversion between the FrFT angle and the FrFT order, we include an optional multiplier of $\pi/2$ in the formula. By modifying the expression in (4.2) and using the search range of $\alpha_b = 3\pi/4$ and $\alpha_a = \pi/4$ as initial values, we can determine the optimal number of iterations for using the GSS algorithm to estimate the chirp rate.

$$I = \left\lceil \frac{\log\left(\frac{\pi}{2} \times \frac{N^{-3}}{\alpha_b - \alpha_a}\right)}{\log(r)} \right\rceil = \left\lceil \frac{3\log N}{\log(1/r)} \right\rceil. \tag{4.9}$$

Apart from the initial iteration that requires two FrFTs, each subsequent iteration in GSS algorithm requires only a single FrFT. Therefore, a total of $(I + 1)$ FrFTs are required to estimate the chirp-rate of a mono-component chirp. Consequently, the overall computational cost of GSS for a mono-component scenario is determined.

$$\text{Computational Cost (Single Chirp)} = \mathcal{O}(I \times N \log N), = \mathcal{O}(N \log^2 N), \tag{4.10}$$

where $O(N \log N)$ is the computational cost of a single FrFT [96] and that $(I + 1) = \mathcal{O}(\log N)$ can be replaced. For a K-component multi-chirp signal, the total computational cost of the GSS is

$$\text{Computational Cost (Multi Chirp)} = \mathcal{O}(K \times I \times N \log N), = \mathcal{O}(K \times N \log^2 N). \tag{4.11}$$

The computational cost of several methods, including coherent ICPF (CICPF), Lv's distribution (LVD), parameterized centroid frequency-chirp rate distribution (PCFCRD) [60], product high-order ambiguity function (PHAF) [126], and keystone transformation of the WVD (KWT) [44], are presented in Table 4.1. Where, M is the number of used lags in PHAF. The GSS method has unquestionably the lowest computational cost when compared with the computational costs of these algorithms.

Table 4.1 Comparison of the Computational Costs of Various Algorithms

Algorithm	Computational Cost
CICPF	$\mathcal{O}(N^3)$
LVD	$\mathcal{O}(N^2 \log N)$
PCFCRD	$\mathcal{O}(N^2 \log N)$
KWT	$\mathcal{O}(N^2 \log N)$
PHAF	$\mathcal{O}(KNM \log N)$
Proposed Algorithm	$\mathcal{O}(KN \log^2 N)$

4.3.2 The Validity of the GSS in the Multi-Component LFM Case

The GSS algorithm is based on the assumption that $P(\alpha)$ can be treated as a unimodal function in noise-free scenarios and almost unimodal when a certain level of noise is present. This is due to the FrFT's rotation property, which concentrates the chirp energy more strongly than the noise energy in the time-frequency plane. This concept remains valid in multi-component cases, although the mutual influence between components must be considered. The effect is greater when the components are closer to each other. Fig. 4.7 and Fig. 4.8 plot $P_2(\alpha)$ for two component chirp signal with two signal lengths in the noiseless case for the following LFM signal

$$s_2(n) = e^{j\pi\left(0.175(n)^2+0.2(n)\right)} + e^{j\pi\left(0.075(n)^2+0.2(n)\right)}. \tag{4.12}$$

The figure indicates that the $P_2(\alpha)$ function has two distinct peaks that correspond to the two components present. Furthermore, it is apparent that for each component, the $P_2(\alpha)$ function is unimodal. The slight nonlinearity observed between the two components in the figure is due to the time window effect. However, as the Fig. 4.8 shows, when the signal duration is increased to $N = 2048$, this effect diminishes. Fig. 4.9 and Fig. 4.10 demonstrate the application of the GSS algorithm to the same chirp signal in the noiseless case. The figures only display the first 10 iterations. In Fig. 4.9 the GSS algorithm iterates until it finds the optimal value of α for the component $m = 0.175$, after which this component is removed. In Fig. 4.10 the GSS algorithm is applied again to the signal after removing the first component. It is evident from the figure that six to seven iterations are sufficient to enter the nearly noise-free region for the two components. Fig. 4.11 and Fig. 4.12 show the GSS algorithm applied to the same chirp signal with an SNR of -6 dB. It is evident that the GSS algorithm's performance remains unaffected even in the presence of noise. This is due to the fact that $\widetilde{P}(\alpha)$ retains its characteristics and does not change significantly, despite the presence of noise. Similar to the mono-component case, the GSS algorithm quickly enters the almost-noise-free region for multi-component chirp signals. It is fast

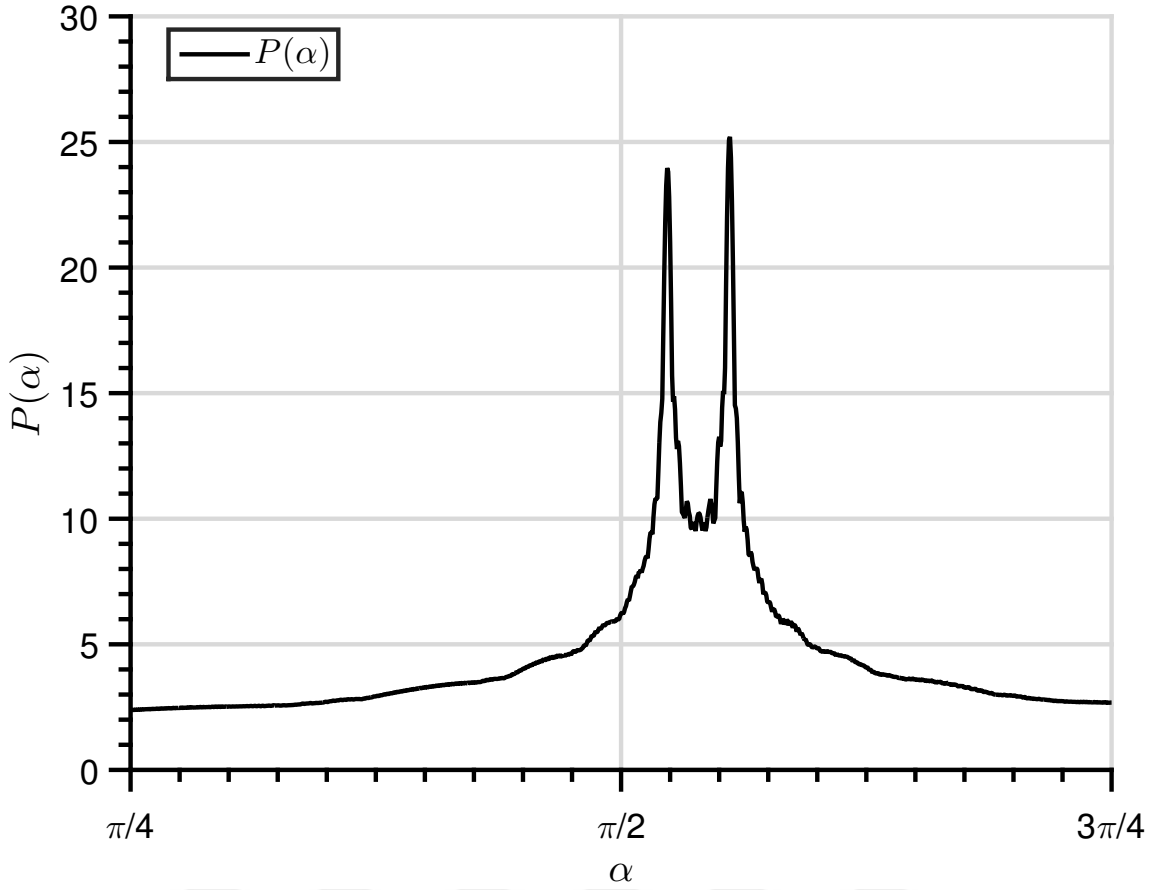

Figure 4.7 The $P(\alpha)$ of two-component LFM signal in noiseless case and when $N = 512$.

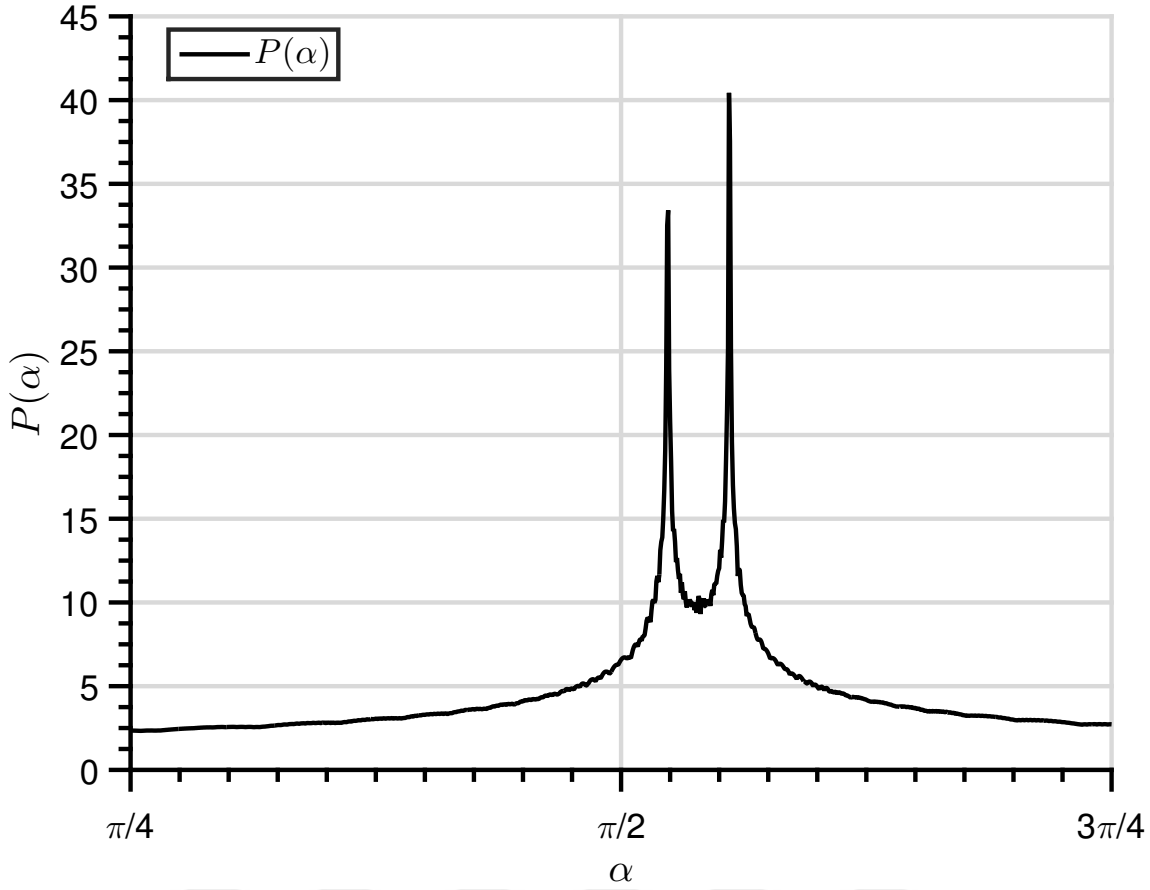

Figure 4.8 The $P(\alpha)$ of two-component LFM signal in noiseless case $N = 2048$.

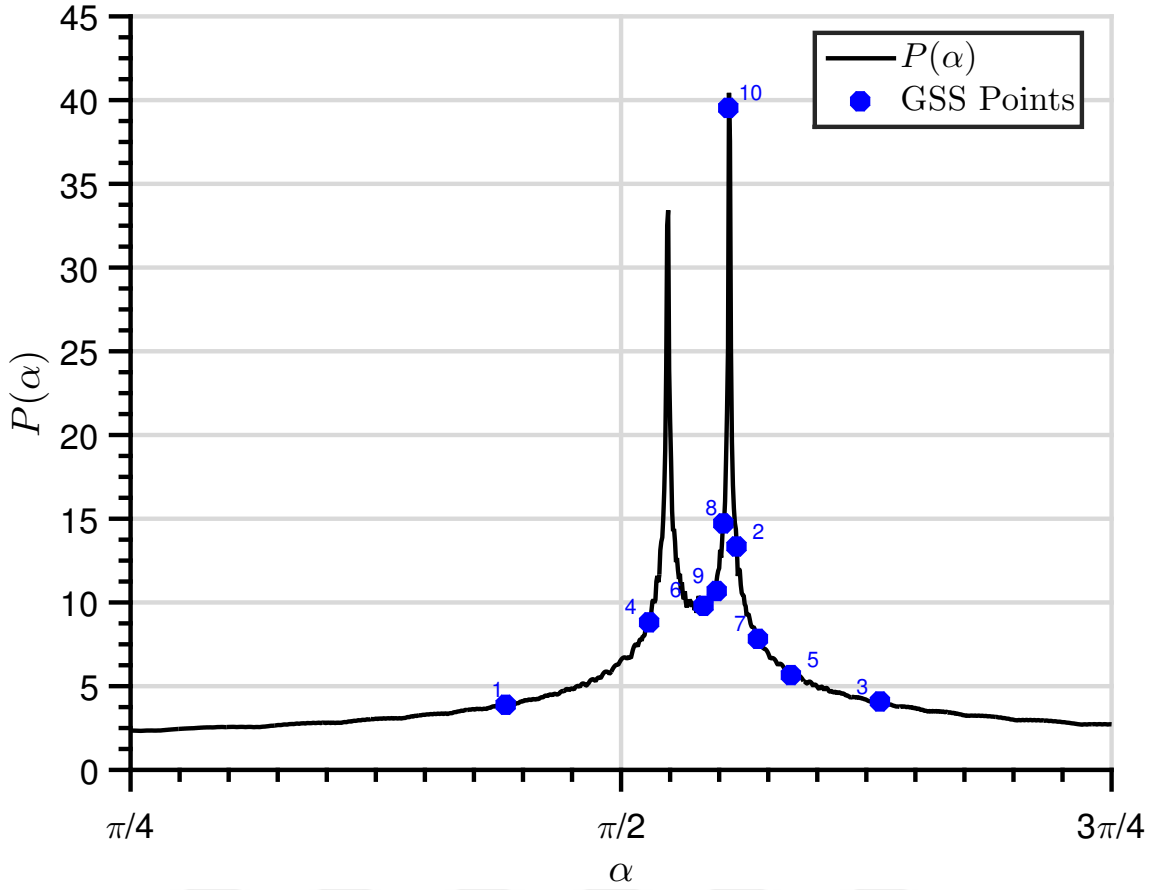

Figure 4.9 The GSS algorithm for two components in noiseless case.

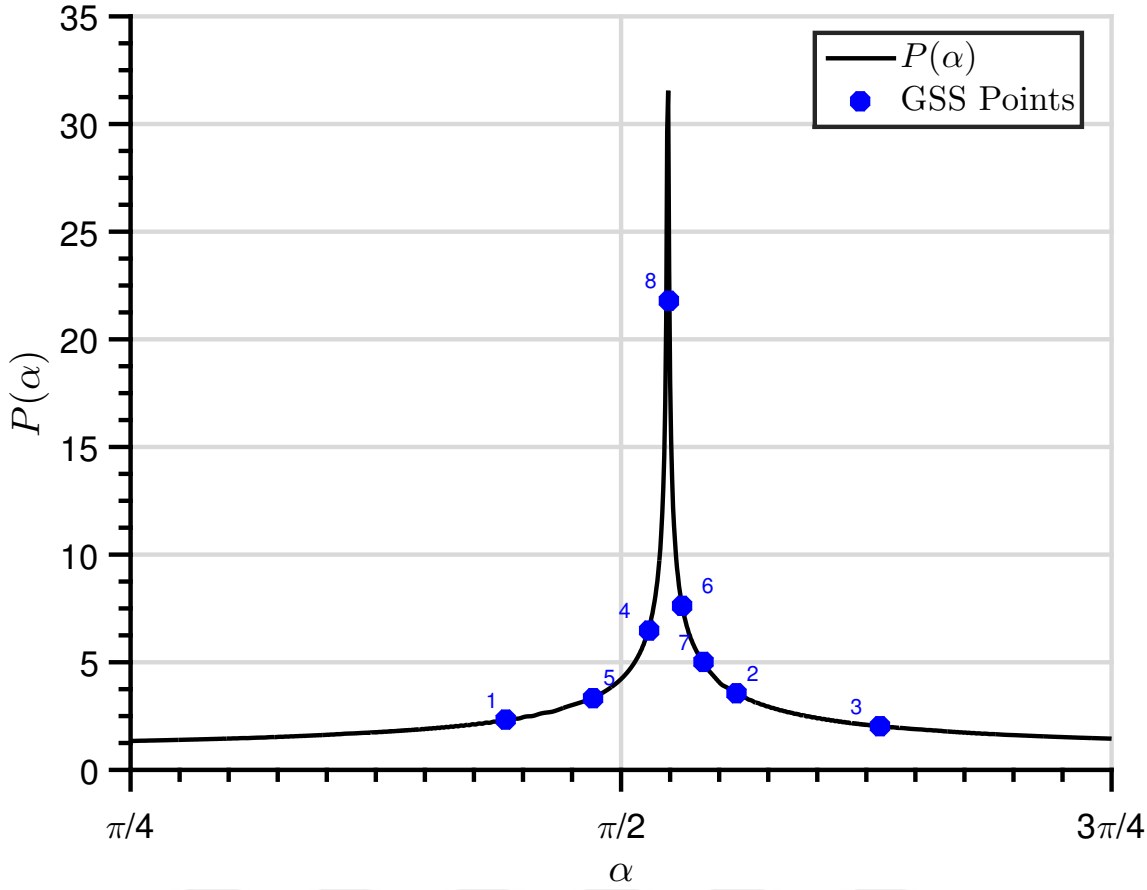

Figure 4.10 The GSS algorithm for two components after removing the first component in noiseless case.

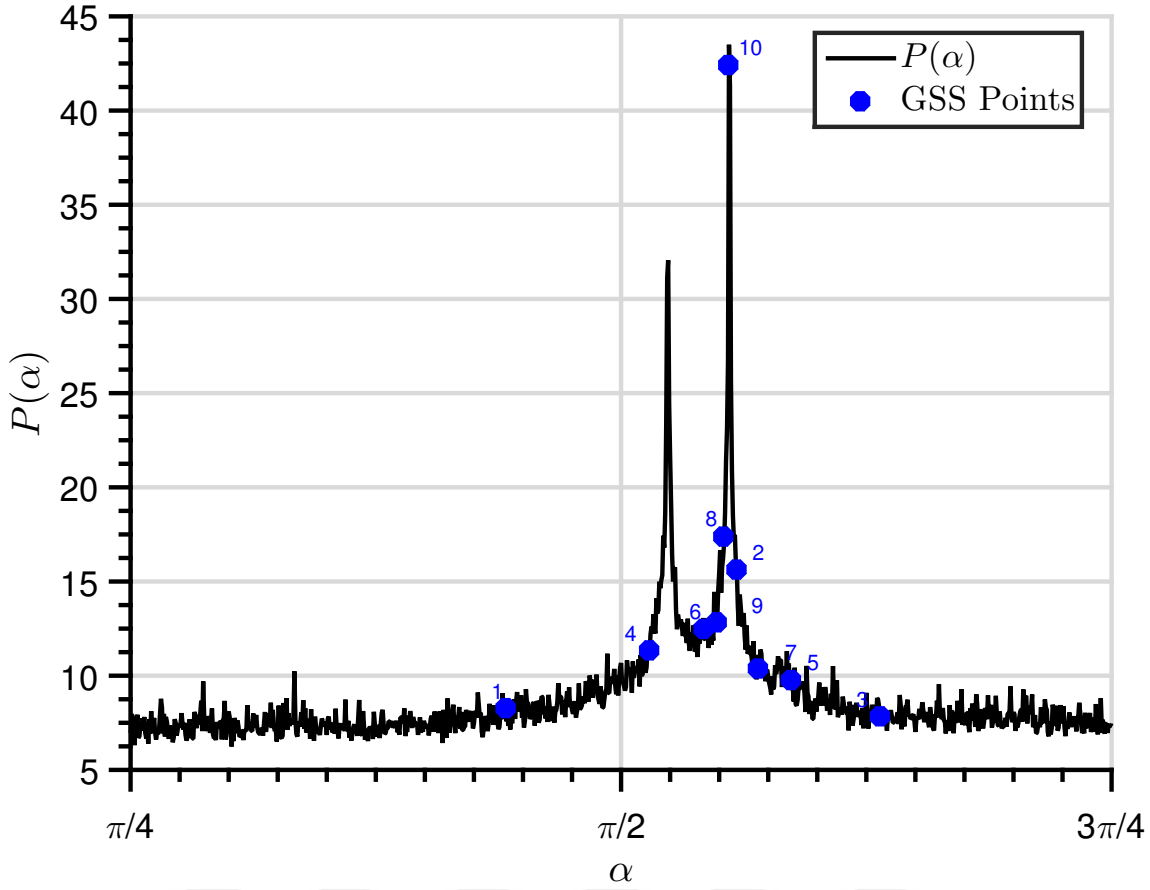

Figure 4.11 The GSS algorithm for two components in noisy case.

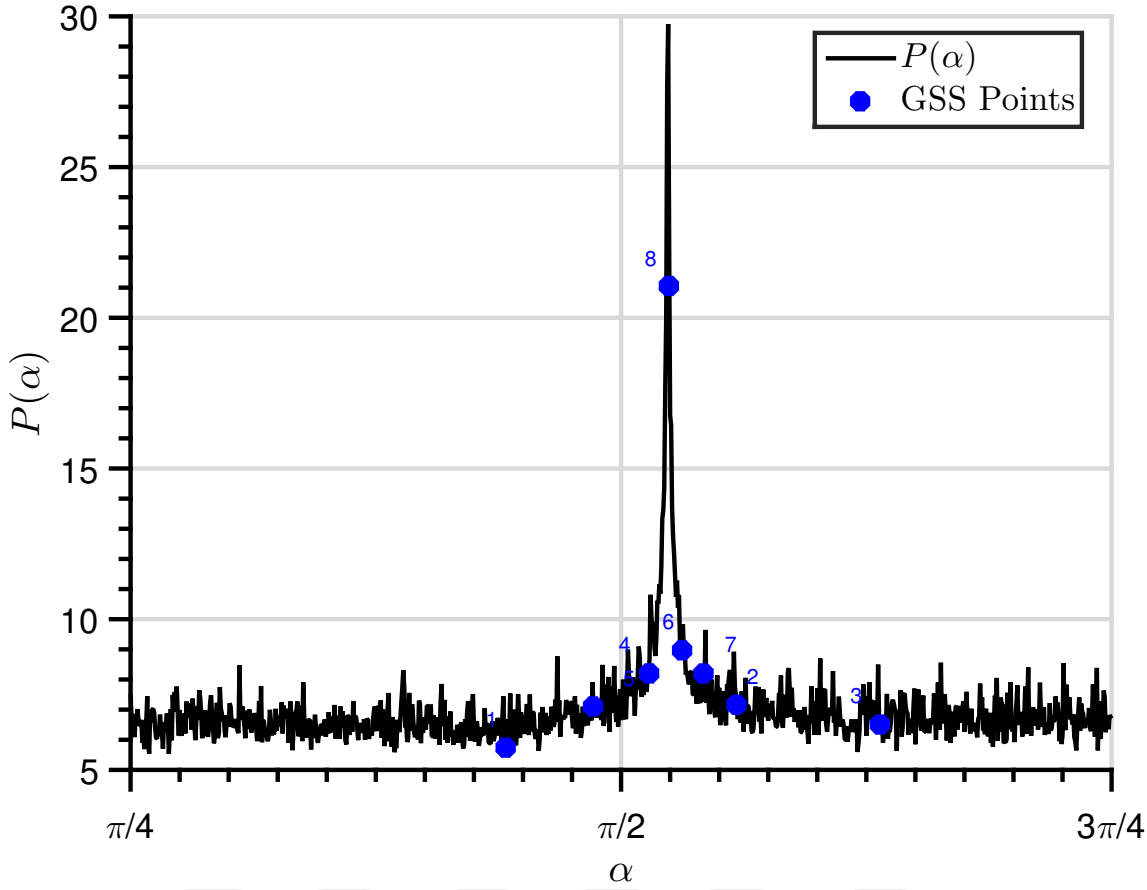

Figure 4.12 The GSS algorithm for two components after removing the first component in noisy case.

and accurate, making it an efficient method for estimating the chirp rate of mono and multi-component chirp signals. The GSS algorithm excludes regions that are not expected to have a maximum inside when it starts iterating. Therefore, in the multi-component case, when the GSS algorithm reaches a noiseless region related to one of the maximum values, it continues until it finds the maximum of that region, as this region can be considered almost uni-modal, just like in the mono-component case. The algorithm removes the estimated component from the original signal, effectively eliminating the effect of this component. The validity of the GSS algorithm depends on the validity of the $P(\alpha)$ function, which maintains its characteristics when the SNR is not too low, and the time duration of the chirp is long. Even when higher noise levels are introduced, there are several ways to access the uni-modal area and initiate the GSS algorithm from this point. The simplest approach is to use the same first search phase as in Zheng and Shi's MACF algorithm. The key aspect of this algorithm is its ability to find the maximum value using the minimum number of iterations. Therefore, if the uni-modal area is accessed, the algorithm will yield the best performance at the minimum computational cost.

4.3.3 Simulations

Extensive computer simulations demonstrate the accuracy and convenience of the proposed GSS-based estimation techniques for LFM parameter estimation. To evaluate performance under various noise levels, Monte Carlo simulations were conducted with $R = 2,000$ repetitions for each SNR value ranging from -10 dB to 10 dB at 2 dB intervals. The MSE was used as the performance metric.

$$MSE = \frac{1}{C}\sum_{i=1}^{C}(\widehat{m}^{(i)} - m)^2, \tag{4.13}$$

where $\widehat{m}^{(i)}$ is the estimated chirp-rate for the $i-th$ iteration of the Monte Carlo simulation and m is the actual value of the chirp-rate, for each value of the SNR.

4.3.3.1 Mono-Component Case

To validate the theoretical results, three different mono-chirp signals of varying lengths and parameter sets were generated. The first signal had a length of $N = 256$ and parameters $A, f_0, m = 1, 0.2, -0.2$, the second signal had a length of $N = 512$ and parameters $A, f_0, m = 1, -0.1, 0.2$, and the third signal had a length of $N = 1024$ and parameters $A, f_0, m = 1, -0.1, 0.2$. The required number of FrFTs for each Monte Carlo simulation were 36, 40, and 45 for the signals with lengths of 256, 512, and

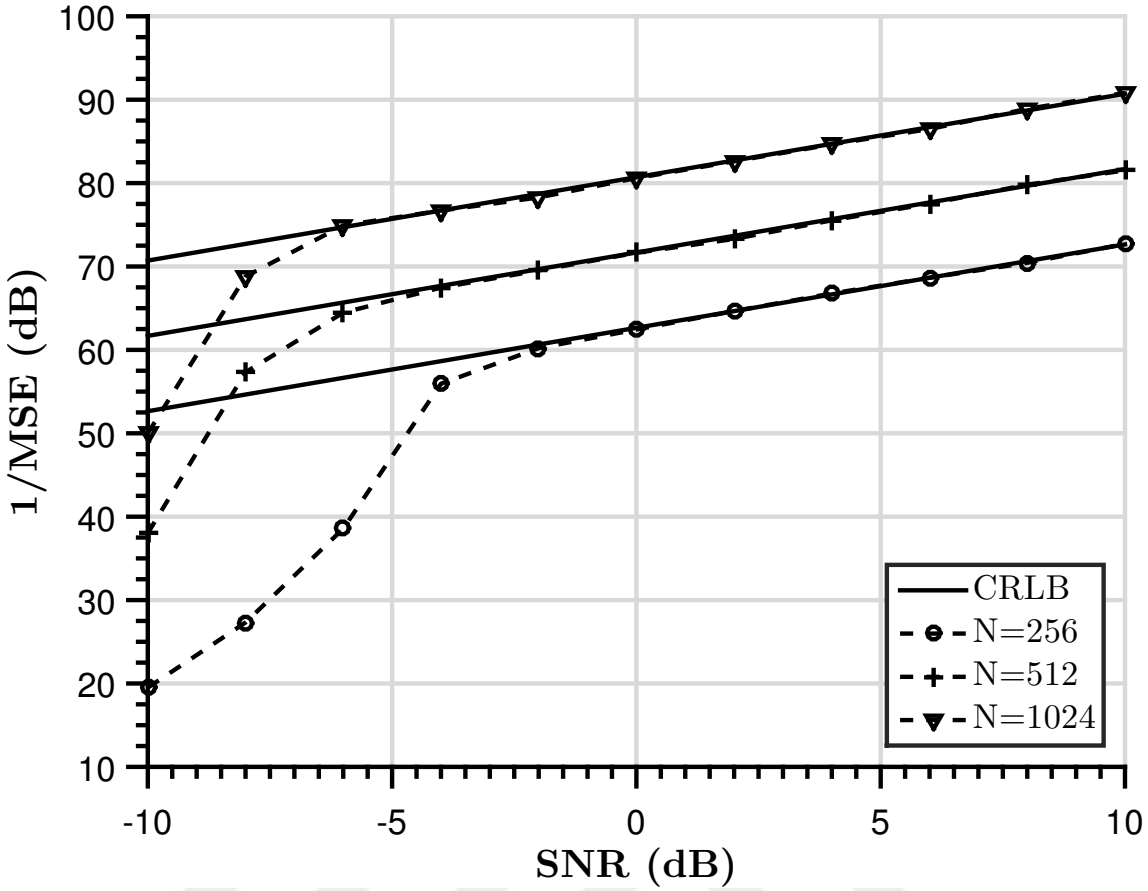

Figure 4.13 Performance comparison of the proposed GSS algorithm for mono-component chirp signals with different lengths.

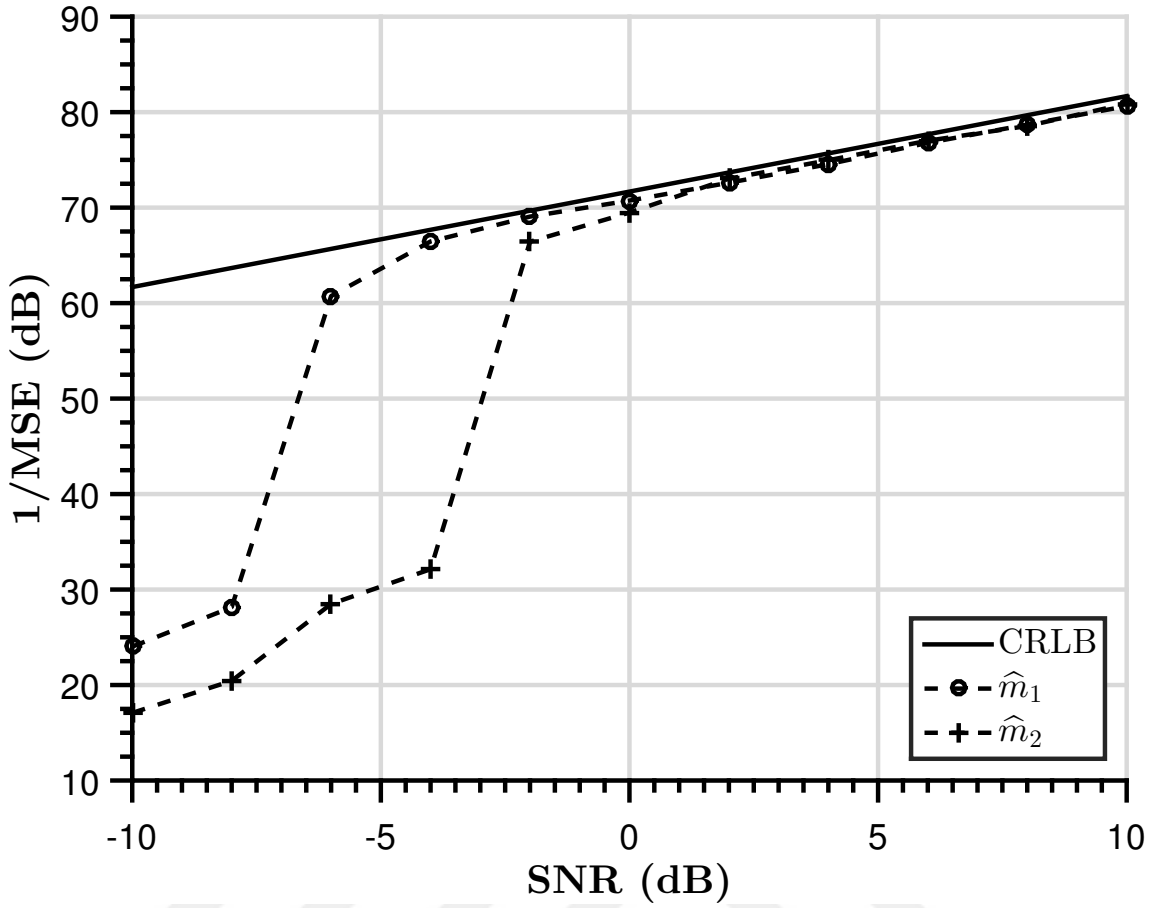

Figure 4.14 Performance comparison of the proposed GSS algorithm for a bi-component chirp signal.

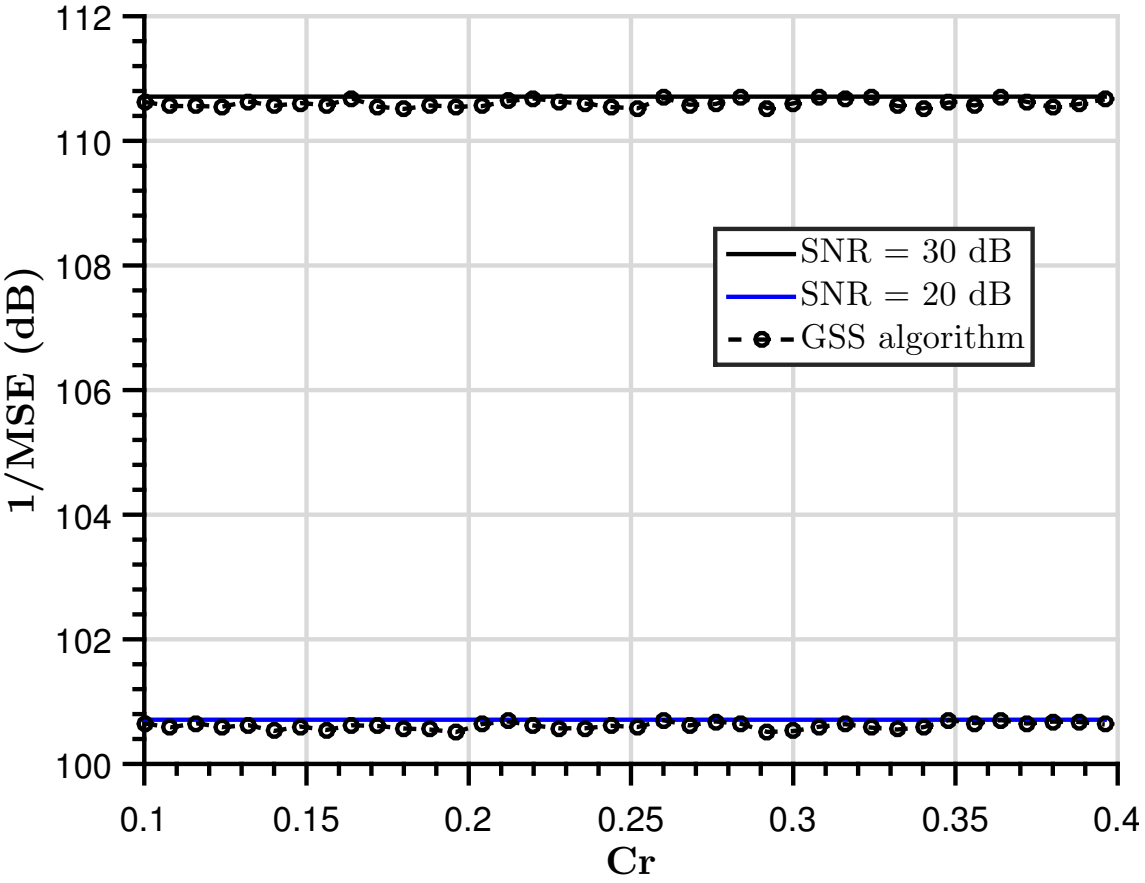

Figure 4.15 The performance of the proposed algorithm for a range of chirp rates between 0.1 and 0.4.

1024, respectively. These numbers confirm the theoretical number of iterations given by (6.22).

Fig. 4.13 presents a comparison between the simulation results and the CRLB for the three aforementioned scenarios. The proposed GSS algorithm for estimating the chirp rate of mono-chirp signals approaches the CRLB, as shown in the figure. This confirms the correctness, validity, and compatibility of the proposed algorithm, along with its extremely low computational cost. This leads to the conclusion that the proposed enhanced algorithm is fast, precise, and reliable.

To test the usability of the proposed algorithm, another simulation was conducted. Fig. 4.15 presents the performance of the proposed algorithm for a range of chirp rates between 0.1 and 0.4. The almost flat results in the two SNR scenarios demonstrate the validity of the proposed technique for various chirp rate values.

4.3.3.2 Multi-Component Case

In order to assess the effectiveness and accuracy of the GSS method for multi-component chirps, a similar experiment was conducted using a bi-component chirp signal. The signal had a length of $N = 512$ and the parameters were $A_1, f_1, m_1 = 1, -0.1, 0.1$ and $A_2, f_2, m_2 = 1, 0.2, -0.2$.

The simulation results for both estimated chirp rates, $\widehat{m}_1$ and $\widehat{m}_2$, are shown in Fig. 4.14, along with the CRLB. The figure clearly demonstrates that the GSS technique can be extended to the multi-component scenario, as the results closely match the CRLB for both components.

4.3.4 Results and Discussion

In this chapter, a novel chirp-rate estimation algorithm was introduced for both mono and multi-component LFM signals. The proposed method relies on the FrFT and the GSS algorithm, which exploit the concept of the optimal transform angle in the FrFT domains that corresponds to the chirp rate, leading to an impulse with maximum magnitude and compact signal energy [117, 118]. The FrFT-based approach allows for efficient estimation of chirp rates by searching for the maximum magnitude in the FrFT domains, which directly corresponds to the chirp rate of the signal. To reduce computational complexity, Zheng and Shi [105] proposed a coarse-to-fine grid-search approach to estimate the compact fractional Fourier domain using the maximum magnitude concept.

The proposed technique enhances chirp-rate estimation accuracy in noisy environments more effectively than existing methods by utilizing the GSS algorithm to identify the maximum squared magnitude of the FrFT domains. The GSS algorithm accelerates the estimation process and improves accuracy in noisy conditions. The performance of the proposed algorithm was evaluated using computer simulations, which demonstrated that the initial version of the algorithm achieves high accuracy, with parameter estimates approaching the CRLB for SNR values as low as -7 dB.

According to the simulation results, the proposed method achieves higher accuracy in estimating chirp rates in noisy environments and outperforms Zheng and Shi's method [105] while incurring lower computational costs. The proposed algorithm also determines the optimum number of iterations required by the GSS algorithm to achieve the CRLB. In addition, the proposed algorithm was extended to the multi-component case, demonstrating that it achieves the CRLB for both mono and multi-component LFM signals with the lowest computational cost compared to similar algorithms.

In summary, the proposed algorithm offers a more efficient and accurate solution for chirp-rate estimation in noisy environments and provides a promising approach for a wide range of practical applications, including radar, sonar, and biomedical signal processing.

5
Peak Magnitude Of The Fractional Fourier Transform: Analytical Formulation

5.1 Introduction

The index of the peak FrFT magnitude (PFM), also known as the maximum magnitude of the FrFT, has become a commonly used tool for estimating the parameters of LFM signals, as demonstrated in various studies [104–106, 114]. In particular, [104] shows that the PFM is asymptotically efficient for estimating LFM signal parameters, and that it is dependent solely on the chirp-rate of the signal, making it an efficient and reliable tool for parameter estimation in terms of both performance and computational efficiency. In this chapter, we provide mathematical analyses to derive approximate models for the PFM of both mono and multi-component LFM signals in both noiseless and noisy environments. We also investigate the statistical properties of the PFM for mono and multi-component LFM signals in the presence of noise. Under certain conditions, such as high SNR and large signal length, as well as in the vicinity of the optimal FrFT angle, the statistical properties of the PFM converge to unbiased mean and zero variance asymptotically. Overall, our work provides a deeper understanding of the properties of the PFM and its usefulness as a tool for LFM signal parameter estimation, even in noisy environments. Our findings can contribute to the development of more effective and efficient algorithms for LFM signal processing.

5.2 The Analytical Model of the $P(\alpha)$ Function

[106] introduces analytical formulations, approximations, and bounds for the angle sweep of the maximum magnitude of FrFT in mono and multi-component LFM signals. In this paper, the chirp signal is multiplied by a Gaussian window, making the analytical approximation specifically valid for this case with limited resolution. However, recognizing this limitation, we propose a general analytical approximation for the PFM that offers unlimited resolution. This enables the application of these models in various real-world scenarios.

5.2.1 Noiseless Case

In the following, we will present Theorem 5, which provides an analytical model for $P(\alpha)$ that is approximately valid for noiseless mono-component LFM signals. This model will be useful for estimating the chirp-rates of such signals.

Theorem 5. *For a mono-component LFM signal with chirp-rate m and in the absence of noise, an analytical expression that can approximate $P(\alpha)$ is*

$$P(\alpha) \approx \Omega(\alpha; m) = |A|^2 \gamma \frac{\cosh(z) - \cos(z)}{\cosh(z) + \cos(z)}, \tag{5.1}$$

where

$$\gamma = \frac{\csc(\alpha)}{m + \cot(\alpha)}, \;\; z = T\sqrt{2\,(m + \cot(\alpha))}. \tag{5.2}$$

Proof. The FrFT of the chirp signal $s(t)$, defined in (2.1), is

$$S_\alpha(u) = AA_\alpha e^{j\pi u^2 \cot\alpha} \int_{-\frac{T}{2}}^{\frac{T}{2}} e^{j\pi\left((2f - 2u\csc\alpha)t + (\cot\alpha + m)t^2\right)} dt, \tag{5.3}$$

where $S_\alpha(u) = \mathscr{F}^\alpha\{s(t)\}(u)$. According to [127, pp. 339],

$$\int_{-T}^{T} e^{j\pi\left(at^2 + 2bt + c\right)} dt = \frac{1}{2}\sqrt{\frac{1}{ja}} e^{\frac{j\pi(ac - b^2)}{a}} \left(\operatorname{erfi}\left(\sqrt{\frac{j\pi}{a}}(aT + b)\right) - \operatorname{erfi}\left(\sqrt{\frac{j\pi}{a}}(b - aT)\right)\right). \tag{5.4}$$

By using (5.4), (5.3) can be simplified to

$$|S_\alpha(u)|^2 = \frac{-j|A|^2\gamma}{4}\Big(\operatorname{erf}(z_1) - \operatorname{erf}(z_2)\Big)\Big(\operatorname{erfi}(z_2) - \operatorname{erfi}(z_1)\Big), \tag{5.5}$$

where erf(·) and erfi(·) are the Gaussian error and the Gaussian imaginary error functions, respectively. The equation above can be further simplified to

$$|S_\alpha(u)|^2 = \frac{|A|^2\gamma}{4}|\operatorname{erf}(z_1) - \operatorname{erf}(z_2)|^2, \tag{5.6}$$

where, the arguments z_1 and z_2 are

$$\begin{aligned} z_1 &= \frac{(1-j)\sqrt{\frac{\pi}{2}}(u_c+\rho_\alpha/2-u)\csc\alpha}{\sqrt{\cot\alpha+m}}, \\ z_2 &= \frac{(1-j)\sqrt{\frac{\pi}{2}}(u_c-\rho_\alpha/2-u)\csc\alpha}{\sqrt{\cot\alpha+m}}. \end{aligned} \tag{5.7}$$

When α is close to α_{opt}, a Taylor approximation of (5.6) around $\alpha = \alpha_{opt}$ yields

$$\begin{aligned} |S_\alpha(u)|^2 &= \frac{|A|^2\csc\alpha\sin^2\Big(\pi T(f-u\csc\alpha)\Big)}{\pi^2(f-u\csc\alpha)^2}+\nu, \\ &= |A|^2T^2\csc\alpha\,\mathrm{sinc}^2\Big(T(f-u\csc\alpha)\Big)+\nu, \end{aligned} \tag{5.8}$$

where $\nu \sim \mathcal{O}(\alpha-\alpha_{opt})$. From the equation above we can see that the index of the maximum value is $u = u_c = f\sin\alpha$.

When α is significantly far from α_{opt}, $|S_\alpha(u)|^2$ is almost rectangular, and the center index of this rectangle is also at $u = u_c = f\sin\alpha$ (see Sec. 2.3.3). By applying the Euler expansion $e^{i\phi} = \cos\phi + j\sin\phi$, the exponential term in (5.3) can be separated into two terms, and $|S_\alpha(u)|^2$ in (5.5) can be expressed as:

$$|S_\alpha(u)|^2 = \frac{|A|^2\gamma}{2}\big(C(z_3)-C(z_4)\big)^2+\big(S(z_3)-S(z_4)\big)^2, \tag{5.9}$$

where, $C(\cdot)$ and $S(\cdot)$ are Fresnel sine and cosine integral functions. The arguments z_3 and z_4 are

$$z_3 = (j-1)\sqrt{\pi}z_1, z_4 = (j-1)\sqrt{\pi}z_2. \tag{5.10}$$

According to [127, pp. 890], when the arguments of $C(\cdot)$ and $S(\cdot)$ are outside the range of $[-1,1]$, these functions are nearly constant and approximately equal to $1/2$. When α is far from α_{opt} and T is sufficiently large, both arguments z_3 and z_4 are outside the range of $[-1,1]$. Thus, it can be concluded that $|S_\alpha(u)|^2$ is approximately constant and equal to

$$|S_\alpha(u)|^2 \approx |A|^2\gamma. \tag{5.11}$$

Consequently, we can assume that $\max|S_\alpha(u)|^2 \approx |S_\alpha(u_c)|^2$ in this case.

In summary, we can conclude the following: when α is close to α_{opt}, $|S_\alpha(u)|^2$ reaches its maximum value at $u = u_c = f\sin\alpha$. When α is far from α_{opt}, the support of $|S_\alpha(u)|^2$ is almost rectangular, and we can consider the center point of the support, $u = u_c = f\sin\alpha$, as the index of the maximum value of $|S_\alpha(u)|^2$. Therefore, for all values of α, we can approximate $\max|S_\alpha(u)|^2$ as $|S_\alpha(u_c)|^2$, where $u_c = f\sin\alpha$ for all

values of α. Therefore, substituting $u = u_c$ in (5.7) yields

$$z_2 = -z_1 = \frac{j-1}{4}\sqrt{\pi}z, \tag{5.12}$$

which further yields an approximation to the maximum of (5.6), *i.e.,*

$$\max_u |S_\alpha(u)|^2 \approx |A|^2\gamma \left|\text{erf}\left(\frac{j-1}{4}\sqrt{\pi}z\right)\right|^2. \tag{5.13}$$

We can approximate the error function by using

$$\text{erf}(x) \approx \tanh\left(\frac{2x}{\sqrt{\pi}}\right), \tag{5.14}$$

for nearly all values of x [128]. For complex arguments, $\tanh(\cdot)$ can be alternatively represented for any real a and b by [129]

$$\tanh(a+bj) = \frac{\sinh(2a) + j\sin(2b)}{\cosh(2a) + \cos(2b)}. \tag{5.15}$$

Substituting (5.15) in (5.13) then yields

$$\begin{aligned} \max_u |S_\alpha(u)|^2 &\approx |A|^2\gamma \left|\frac{j\sin z - \sinh z}{\cosh z + \cos z}\right|^2. \\ &\approx |A|^2\gamma \frac{\sinh^2 z + \sin^2 z}{(\cosh z + \cos z)^2}. \end{aligned} \tag{5.16}$$

Finally, substituting $\sinh^2 z = \cosh^2 z - 1$ and $\sin^2 z = 1 - \cos^2 z$ in the equation above gives (5.1), which concludes the proof. ■

5.2.2 Noisy Case

In this section, we will examine $P(\alpha)$ in the presence of additive noise. To differentiate between the noisy and noiseless cases, we will use $\widetilde{P}(\alpha)$ to denote the function $P(\alpha)$ in the presence of noise. Since $\widetilde{s}(t)$ is a random process, so is $\widetilde{P}(\alpha)$. In order to model $\widetilde{P}(\alpha)$, we will determine its expected value and variance. The following theorem is presented for this purpose.

Theorem 6. *In the noisy environment, the expected value and variance of $\widetilde{P}(\alpha)$ can be approximated by*

$$\begin{aligned} E\left[\widetilde{P}(\alpha)\right] \approx \widetilde{\Omega}(\alpha; m) &= |A|^2\gamma \frac{\cosh z - \cos z}{\cosh z + \cos z} + \sigma^2 T \csc\alpha, \\ &= \Omega(\alpha; m) + \sigma^2 T \csc\alpha, \end{aligned} \tag{5.17}$$

and

$$\operatorname{var}\left[\widetilde{P}(\alpha)\right] \approx \widetilde{\Omega}^2(\alpha; m) - \Omega^2(\alpha; m), \tag{5.18}$$

where γ *and* z *are given in* (5.2) *and* $\Omega(\alpha; m)$ *is the same as given in* (5.1).

Proof. We now define $\widetilde{P}(\alpha)$ as

$$\widetilde{P}(\alpha) = \max_u \left\{ \left| \mathscr{F}^{\alpha} \left\{ \widetilde{s}(t) \right\} (u) \right|^2 \right\}. \tag{5.19}$$

In the absence of noise, $P(\alpha)$ reaches its maximum value at $u = u_c$. However, when noise is present, the index at which $\widetilde{P}(\alpha)$ achieves its maximum is shifted from u_c to $u_c + \delta u$, where δu represents the perturbation or displacement caused by the noise. Thus, δu is a random variable that affects $\widetilde{P}(\alpha)$ in a nontrivial way. To study this effect, we will perform a perturbation analysis. The expected value of $\widetilde{P}(\alpha)$ is

$$E\left[\widetilde{P}(\alpha)\right] = E\left[\left| S_\alpha(u) + W_\alpha(u) \right|^2 \Big|_{u_c + \delta u} \right], \tag{5.20}$$

where $W_\alpha(u)$ is the FrFT of the noise. Expanding (5.20) gives

$$\begin{aligned} E\left[\widetilde{P}(\alpha)\right] = E\Big[& \left\{ |S_\alpha(u)|^2 + W_\alpha(u) S_\alpha^*(u) \right. \\ & \left. + S_\alpha(u) W_\alpha^*(u) + |W_\alpha(u)|^2 \right\} \Big|_{u_c + \delta u} \Big]. \end{aligned} \tag{5.21}$$

We focus on the above terms separately. Assuming that δu is small and adopting the same analysis as in [107], we can expand the first term using a first-order Taylor series, yielding

$$\begin{aligned} E\left[|S_\alpha(u)|^2 \Big|_{u_c + \delta u} \right] \approx & E\left[|S_\alpha(u)|^2 \Big|_{u_c} \right] \\ & + E\left[\frac{\partial}{\partial u} |S_\alpha(u)|^2 \Big|_{u_c} \delta u \right]. \end{aligned} \tag{5.22}$$

The higher-order terms with orders $\mathcal{O}(\delta u^n)$, where $n > 1$ in (5.22) are neglected since δu is small, making the higher-order terms negligible.

Moreover, note that the second term in the left-hand side of (5.22) is zero, since the derivative at the maximum is zero. Then,

$$E\left[|S_\alpha(u)|^2 \Big|_{u_c + \delta u} \right] \approx E\left[|S_\alpha(u)|^2 \Big|_{u_c} \right] = P(\alpha) \approx \Omega(\alpha; m). \tag{5.23}$$

The second and third terms in (5.21) are zero, *i.e.*,,

$$E\left[\left\{W_\alpha(u)S_\alpha^*(u)+S_\alpha(u)W_\alpha^*(u)\right\}\Big|_{u_c+\delta u}\right]=0, \tag{5.24}$$

as the noise is zero mean. The last term in (5.21) can be calculated by

$$\begin{aligned} E\left[\,|W_\alpha(u)|^2\,\right] &= E\left[\,|W_\alpha(u)|^2\Big|_{u_c+\delta u}\right] = \\ &\csc\alpha\iint_T E\left[w(t)w^*(\upsilon)\right]K_\alpha(t,u)K_\alpha^*(\upsilon,u)dtd\upsilon. \end{aligned} \tag{5.25}$$

Replacing $E\left[w(t)w^*(\upsilon)\right]=\sigma^2\delta(t-\upsilon)$ gives

$$E\left[\,|W_\alpha(u)|^2\,\right]=\sigma^2\csc\alpha\int_T dt=\sigma^2T\csc\alpha. \tag{5.26}$$

Substituting (5.23), (5.24) and (5.26) into (5.21) gives (5.17). Therefore, the first part of the proof regarding (5.17) is completed. The variance of $\widetilde{P}(\alpha)$ is

$$\mathrm{var}\left[\widetilde{P}(\alpha)\right]=E\left[\widetilde{P}(\alpha)^2\right]-E^2\left[\widetilde{P}(\alpha)\right]. \tag{5.27}$$

Expanding the first term in the equation above gives

$$\begin{aligned} E\left[\widetilde{P}(\alpha)^2\right]=E\Big[&\left\{|S_\alpha(u)|^2+W_\alpha(u)S_\alpha^*(u)\right.\\ &+S_\alpha(u)W_\alpha^*(u)+|W_\alpha(u)|^2\left.\right\}\left\{|S_\alpha(u)|^2+W_\alpha(u)S_\alpha^*(u)\right.\\ &\left.+S_\alpha(u)W_\alpha^*(u)+|W_\alpha(u)|^2\right\}^*\Big|_{u_c+\delta u}\Big], \end{aligned}$$

which can be simplified to

$$\begin{aligned} E\left[\widetilde{P}(\alpha)^2\right]=E\Big[&\,|S_\alpha(u)|^4+|W_\alpha(u)|^4+4|S_\alpha(u)|^2\\ &+|W_\alpha(u)|^2\,\Big]\Big|_{u=u_c+\delta u}. \end{aligned} \tag{5.28}$$

The first and third terms of the equation above can be computed by using (5.22) and (5.26). The only missing term is the second term. Assuming $W_\alpha^r(u)$ and $W_\alpha^i(u)$ are real and imaginary parts of the complex Gaussian random variable $W_\alpha(u)$

$$|W_\alpha(u)|^4=\left(W_\alpha^r(u)\right)^4+\left(W_\alpha^i(u)\right)^4+2\left(W_\alpha^r(u)\right)^2\left(W_\alpha^i(u)\right)^2, \tag{5.29}$$

where $W_\alpha^r(u)$ and $W_\alpha^i(u)$ are independent normal random variables with means and

variances

$$\begin{aligned} W_\alpha(u) &\sim N(0, \sigma^2 T \csc\alpha). \\ W_\alpha^r(u), w_\alpha^i(u) &\sim N\left(0, \frac{\sigma^2}{2} T \csc\alpha\right). \end{aligned} \tag{5.30}$$

Therefore, the expected value of $|W_\alpha(u)|^4$ is

$$E\left[\, |W_\alpha(u)|^4 \big|_{u_c+\delta u}\right] = 2E\left[\left(W_\alpha^r(u)\right)^4\right] + 2E^2\left[\left(W_\alpha^r(u)\right)^2\right]. \tag{5.31}$$

Using the fourth and second moments of $W_\alpha^r(u)$ produces

$$\begin{aligned} E\left[\, |W_\alpha(u)|^4 \big|_{u_c+\delta u}\right] &= \tfrac{3}{2}\sigma^4 T^2 \csc^2\alpha + \tfrac{1}{2}\sigma^4 T^2 \csc^2\alpha, \\ &= 2\sigma^4 T^2 \csc^2\alpha. \end{aligned} \tag{5.32}$$

Replacing (5.26) and (5.32) into (5.28) gives

$$E\left[\widetilde{P}(\alpha)^2\right] = P(\alpha)^2 + 2\sigma^4 T^2 \csc^2\alpha + 4\sigma^2 T \csc\alpha P(\alpha). \tag{5.33}$$

Substituting (5.33) and (5.17) into (5.27) gives

$$\mathrm{var}\left[\widetilde{P}(\alpha)\right] = \sigma^4 T^2 \csc^2\alpha + 2\sigma^2 T \csc\alpha P(\alpha). \tag{5.34}$$

The above equation can be rewritten after replacing $P(\alpha)$ by $\Omega(\alpha; m)$ and using (5.17) as

$$\mathrm{var}\left[\widetilde{P}(\alpha)\right] \approx \sigma^2 T \csc\alpha \times \left(\widetilde{\Omega}(\alpha; m) + \Omega(\alpha; m)\right). \tag{5.35}$$

The term $\sigma^2 T \csc\alpha$ can be replaced by $\widetilde{\Omega}(\alpha; m) - \Omega(\alpha; m)$ using (5.17). Therefore the proof is concluded. ■

In practical applications, it is common to sample α within the range of $[\frac{\pi}{4}, \frac{3\pi}{4}]$ to avoid aliasing [53]. In this case, the term $\sigma^2 T \csc\alpha$ in (5.17) takes values within the range of $[\sigma^2 T, \frac{3}{2}\sigma^2 T]$. When α is close to α_{opt} and the SNR is high enough, $\Omega(\alpha; m) \gg \sigma^2 T \csc\alpha$, and the signal dominates the expected value of $\widetilde{P}(\alpha)$, rendering the effect of noise negligible. We refer to this region as the signal-dominant area. Conversely, when α is far from α_{opt}, $\Omega(\alpha; m)$ is almost a small constant value and the effect of noise becomes apparent. In this region, we refer to it as the noise-dominant area. Both regions are depicted in Fig. 5.1. We can establish the validity of this phenomenon by demonstrating that the expected value of $\widetilde{P}(\alpha)$ can be approximated by $P(\alpha)$ when $SNR \gg \frac{1}{T}$. These cases are formalized in the following two corollaries.

Corollary 6.1. *Under the condition* $SNR \gg \frac{1}{T}$

$$E\left[\widetilde{P}(\alpha)\right] \to P(\alpha) \approx \widetilde{\Omega}(\alpha, m), \tag{5.36}$$

asymptotically when α *is close to* α_{opt}.

Proof. In the vicinity of α_{opt} the maximum happens at the index $u = u_c = f_0 \sin\alpha$. According to (5.8), the maximum of $|S_\alpha(u)|^2$ is

$$\max_u |S_\alpha(u)|^2 = |A|^2 T^2 \csc\alpha. \tag{5.37}$$

Using the equation above and (5.26) into (5.17) yields

$$E\left[\widetilde{P}(\alpha)\right] \approx \underbrace{|A|^2 T^2 \csc\alpha}_{P(\alpha)} + \sigma^2 T \csc\alpha. \tag{5.38}$$

Which can be written

$$E\left[\widetilde{P}(\alpha)\right] = P(\alpha) \times \left(1 + \frac{1}{SNR \times T}\right). \tag{5.39}$$

Therefore, the expected value of $\widetilde{P}(\alpha)$ approaches to the noiseless-case $P(\alpha)$ in the vicinity of α_{opt} when $SNR \times T \gg 1$. Therefore, the proof is concluded. ■

It is useful also to elaborate on how $E\left[\widetilde{P}(\alpha)\right]$ is defined in the noise dominant area. Using (5.11) and (5.21)in the case when α is far from α_{opt}, $E\left[\widetilde{P}(\alpha)\right]$ is

$$E\left[\widetilde{P}(\alpha)\right] = |A|^2\gamma + \sigma^2 T \csc\alpha. \tag{5.40}$$

Using (5.2), and rearranging results

$$E\left[\widetilde{P}(\alpha)\right] = \sigma^2 T \csc\alpha \times \left(1 + \frac{SNR}{T\,(m + \cot\alpha)}\right). \tag{5.41}$$

The previous equation indicates that the noise dominates when α is far from α_{opt}. Additionally, from equation (5.17), it is evident that when α is far from α_{opt}, the following applies:

$$\frac{\cosh z - \cos z}{\cosh z + \cos z} \approx 1, \tag{5.42}$$

As m gets farther away from $\cot\alpha$ and T becomes larger, the value of z also increases. Therefore, in this case, the model (5.17) is equivalent to (5.40), which confirms our observations.

Corollary 6.2. *Under the condition* $SNR \gg \frac{1}{T}$

$$\operatorname{var}\left[\widetilde{P}(\alpha)\right] \approx 0, \tag{5.43}$$

asymptotically when α *is close to* α_{opt}.

Proof. Replacing $\widetilde{\Omega}(\alpha, m) \approx P(\alpha) \approx \Omega(\alpha, m)$ in (5.18) by using Corollary 1, the proof can be concluded. ■

In summary, Corollaries 1 and 2 demonstrate that when α is close to α_{opt} and $SNR \times T \gg 1$, the contribution of noise to $\widetilde{P}(\alpha)$ is negligible and the signal dominates. As a result, the expected value of $\widetilde{P}(\alpha)$ in this region approaches $P(\alpha)$, and the variance of $\widetilde{P}(\alpha)$ asymptotically approaches zero.

The following theorem extends these findings from the mono-component case to the case of multi-component LFM signals.

Theorem 7. *In a noisy environment and when the chirp-rates of all the components of a K-component LFM noisy signal* $\widetilde{s}_K(t)$*, defined in* (2.5)*, are separated well enough, the expected value of* $\widetilde{P}_K(\alpha)$ *is*

$$E\left[\widetilde{P}_K(\alpha)\right] \approx \widetilde{\Omega}_K(\alpha; \mathbf{m}) = \sum_{k=1}^{K} \Omega(\alpha; m_k) + \sigma^2 T \csc\alpha, \tag{5.44}$$

where,

$$\widetilde{P}_K(\alpha) = \max_u \left\{ \left| \mathscr{F}^{\alpha} \left\{ \widetilde{s}_K(t) \right\}(u) \right|^2 \right\}, \tag{5.45}$$

where, $\mathbf{m} = [m_1, m_2, \cdots, m_K]^T$ *is a vector containing the actual values of K-component LFM signal chirp-rates, and* $\widetilde{\Omega}_K(\alpha; \mathbf{m})$ *is the analytical expression defined by the chirp-rates* $\mathbf{m}$ *which will be used as a model for* $\widetilde{P}_K(\alpha)$.

Proof. The function $\widetilde{P}_K(\alpha)$ for the K-component LFM signal case comprises K spikes in the α domain, and it can be expressed as follows:

$$\widetilde{P}_K(\alpha) = \max_u \left\{ \left| \sum_{k=1}^{K} S_{\alpha k}(u) + W_{\alpha}(u) \right|^2 \right\}, \tag{5.46}$$

where, $S_{\alpha k}(u)$ is the FrFT of the k—th component. We will start by considering the case of a bi-component LFM signal, and then generalize to a K component LFM signal, which will be straightforward. For a bi-component LFM signal, we can express

equation (5.46) as follows:

$$\widetilde{P}_2(\alpha) = \max_u \left\{ \left| S_{\alpha 1}(u) + S_{\alpha 2}(u) + W_\alpha(u) \right|^2 \right\}. \tag{5.47}$$

When neglecting the leakage between components, the maximum of $\Omega(\alpha; m)$ for a bi-component LFM signal can be expressed as the sum of two separate parts, corresponding to the two components. Then, the expected value of $\widetilde{P}_2(\alpha)$ can be written using the triangle inequality as follows:

$$E\left[\widetilde{P}_2(\alpha)\right] \leq E\left[\left| S_{\alpha 1}(u) + W_\alpha(u) \right|^2 \Big|_{u_{c1}+\delta u} \right] + E\left[\left| S_{\alpha 2}(u) \right|^2 \Big|_{u_{c2}+\delta u} \right]. \tag{5.48}$$

The above equation demonstrates that the expected value $E\left[\widetilde{P}_2(\alpha)\right]$ is bounded by the summation of the expected values of the spikes in the FrFT domain. However, in the limit as T tends to infinity, $\left|S_{\alpha 1}(u)\right|^2$ and $\left|S_{\alpha 2}(u)\right|^2$ converge to two Dirac deltas located at α_{opt_1} and α_{opt_2}, respectively, and the leakage between the two components approaches zero. Thus, as T becomes large, the interference between the components decreases, and the leakage between each can be neglected. As a result, we can use the results from Theorem 2 to approximate the above equation asymptotically, and obtain

$$E\left[\widetilde{P}_2(\alpha)\right] \approx \Omega(\alpha; m_1) + \Omega(\alpha; m_2) + \sigma^2 T \csc\alpha. \tag{5.49}$$

Expanding the equation above for a K component LFM signal provides the proof. ■

5.2.3 $\widetilde{P}(\alpha)$ Statistically

We will perform a statistical analysis of $\widetilde{P}(\alpha)$. We consider a noisy signal that can be represented by the random variable and matrix form $\widetilde{S} = S + W$, where $\widetilde{s}_i$ has a Gaussian distribution with the following mean and variance.

$$\widetilde{s}_i \sim N(s(i), \sigma^2). \tag{5.50}$$

As the introduced noise has a zero mean, the output obtained by processing the noisy signal $\widetilde{S}$ using FrFT is given by:

$$\mathscr{F}_s = \widetilde{S}^T \mathscr{F}. \tag{5.51}$$

Where $\widetilde{S}$ is the noisy signal with the following mean and variance

$$\widetilde{S} \sim N(\mu_s, \sigma^2 I). \tag{5.52}$$

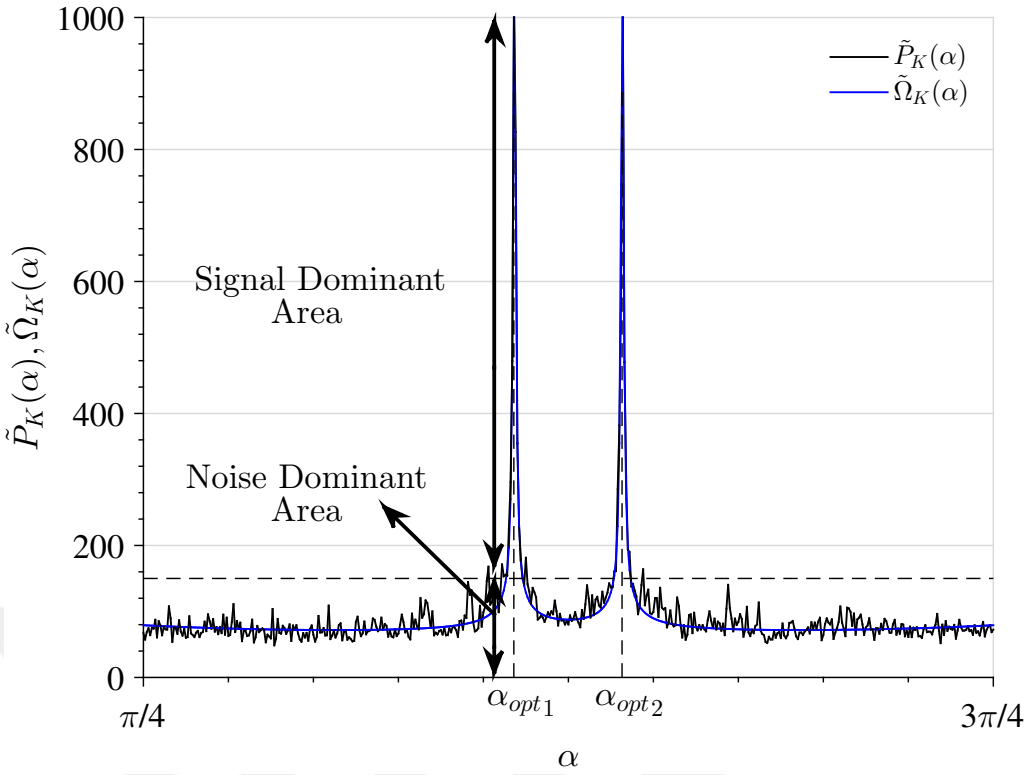

Figure 5.1 $\widetilde{P}_K(\alpha)$ and $\widetilde{\Omega}_K(\alpha;\mathbf{m})$ for a bi-component LFM signal with chirp-rates $\mathbf{m} = [-0.1, 0.1]^T$.

Where $\mu_s = [s(1), s(2), \ldots\ldots, s(N-1)]$, and $\mathscr{F}$ is FrFT operations. $\mathscr{F}_s$, the FrFT of the noisy signal, is also a complex random variable. Therefore, the distribution of $\mathscr{F}_s$ is

$$\mathscr{F}_s \sim N(\mu_s^T \mathscr{F}, \sigma^2 \mathscr{F}^2). \tag{5.53}$$

$\widetilde{P}(\alpha)$ has been defined as $\max_{\alpha\in[0,\pi]} \left\{ |\mathscr{F}^{\alpha} \{\widetilde{s}(t)\}(u)|^2 \right\}$. $\widetilde{P}(\alpha)$ can be written

$$\widetilde{P}(\alpha) = \max_{\alpha\in[0,\pi]} \left\{ \mathscr{F}_s \mathscr{F}_s^H \right\}. \tag{5.54}$$

We begin by considering the independent identically distributed (i.i.d) random variables $\widetilde{S}$, which represents the noisy signal, and $\mathscr{F}_s$, which represents the i.i.d random variables of the FrFT output signal. In the presence of noise, selecting the maximum value in the $\widetilde{P}(\alpha)$ domain can be viewed as selecting the maximum value from a set of discrete random variables in $\mathscr{F}_s$. Let us denote the maximum values of $\mathscr{F}_s$ for each α as:

$$\mathscr{F}_m \mathscr{F}_m^H = \max_{\alpha\in[0,\pi]} \left\{ \mathscr{F}_s \mathscr{F}_s^H \right\}. \tag{5.55}$$

$\mathscr{F}_m \mathscr{F}_m^H$ is the summation

$$\mathscr{F}_m \mathscr{F}_m^H = Re(\mathscr{F}_m)^2 + Im(\mathscr{F}_m)^2. \tag{5.56}$$

The distribution of $\mathscr{F}_m \mathscr{F}_m^H$ follows a noncentral chi-square distribution due to the fact that $Re(\mathscr{F}_m)$ and $Im(\mathscr{F}_m)$ are the sum of squares of independent random variables. In order to obtain a unit variance, we can perform scaling on the random variables. Equation (5.56) can be rewritten as:

$$\mathscr{F}_m \mathscr{F}_m^H = \sigma^2 \mathscr{F}^2 \left(\frac{Re(\mathscr{F}_m)^2}{\sigma^2 \mathscr{F}^2} + \frac{Im(\mathscr{F}_m)^2}{\sigma^2 \mathscr{F}^2} \right). \tag{5.57}$$

Having the above form the degrees of freedom γ and the noncentrality parameter ϵ are,

$$\gamma = 2\sigma^2 \mathscr{F}^2. \tag{5.58}$$

$$\epsilon = \mathscr{F}^2 \mu_s^2. \tag{5.59}$$

As $\mathscr{F}_m \mathscr{F}_m^H$ is a random variable having the noncentral chi-square distribution with degrees of freedom γ and noncentrality parameter ϵ, then the expected value of $\mathscr{F}_m \mathscr{F}_m^H$ is

$$E[\max_{\alpha \in [0,\pi]} \{\mathscr{F}_s \mathscr{F}_s^H\}] = E[\mathscr{F}_m \mathscr{F}_m^H] = \gamma + \epsilon = 2\sigma^2 \mathscr{F}^2 + \mathscr{F}^2 \mu_s^2. \tag{5.60}$$

Upon simple examination of the equation, it is apparent that $\mathscr{F}^2 \mu_s^2$ represents the FrFT at the maximum value, and $2\sigma^2 \mathscr{F}^2$ is the FrFT of the noise at the maximum value. Thus, the maximum magnitude sweep of the FrFT domains in the noisy case equals the maximum magnitude sweep of the FrFT domains in the noiseless case plus the effect of the noise. This confirms the accuracy of our deduction for noisy $\widetilde{P}(\alpha)$.

5.2.4 Results and Discussion

Figure 5.1 compares our proposed model $\widetilde{\Omega}(\alpha; m)$ with the actual $\widetilde{P}_K(\alpha)$ for a bi-component LFM signal with $N = 1024$ length and SNR of -5 dB. The function $\widetilde{P}_K(\alpha)$, computed at $M = N/2$ rotation angles, exhibits two peaks located at α_{opt_1} and α_{opt_2}, corresponding to chirp-rates $m_1 = -0.1$ and $m_2 = 0.1$. $\widetilde{P}_K(\alpha)$ can be divided into two regions dominated by signal and noise, respectively, with the impact of noise being negligible in the signal-dominant area. Our model $\widetilde{\Omega}(\alpha; m)$ accurately fits $\widetilde{P}_K(\alpha)$ in the signal-dominant region and aligns with the mean of $\widetilde{P}_K(\alpha)$ in the noise-dominant region. Since the signal-dominant region is located near α_{opt_1} and α_{opt_2}, our model is effective in estimating chirp-rates of multi-component LFM signals, especially when $T \times SNR \gg 1$ (as stated in Corollary 6.1).

The following conclusions can be drawn from our findings.

- Our proposed models provide close approximations for the PFM of chirp signals

across all FrFT angles, for both noiseless and noisy cases.

- These models are highly accurate approximations of $\widetilde{P}(\alpha)$ and $\widetilde{P}_k(\alpha)$.
- We have also determined the statistical properties of PFM, such as its expected value and variance.
- We derived the relationship between the PFM of a noisy and noiseless LFM signal.
- We have demonstrated that if the FrFT rotation angle is in the vicinity of the optimum angle and $SNR \times T$ is much larger than 1, the PFM is primarily influenced by the PFM of the signal, and the impact of noise can be ignored. Consequently, the statistical characteristics of PFM approach an unbiased expected value and zero variance.
- When SNR is high and T is large, the expected value of the model $\widetilde{P}(\alpha)$ is almost equal to the $P(\alpha)$ function at the vicinity of α_{opt}.
- When the SNR is high and T is large, the variance of the model $\widetilde{P}(\alpha)$ is almost equal to zero.
- The expected value of the proposed model of $\widetilde{P}(\alpha)$ is solely determined by the chirp-rate and σ^2, and is independent of the initial frequency. The model attains its maximum value of $A^2T^2\sqrt{1+m^2}$ at $\alpha = \alpha_{opt}$, and can be effectively utilized for estimating chirp-rates.
- Consequently, we have demonstrated that the expected value of the PFM can serve as an approximation for the PFM of a noisy chirp signal.
- We then extended our proposed approximate model to account for multi-component LFM signals in the presence of noise.

6
Chirp-Rates Estimation Algorithm For Multi-Component LFM Signals

6.1 Introduction

In chapters 3 and 4, we demonstrated the optimality of the FrFT domain-based estimator and presented a fast blind search algorithm based on the GSS algorithm. Both results have been published in [104, 114]. In this chapter, we introduce a coarse-to-fine FrFT-based algorithm for estimating the chirp-rates of a multi-component LFM signal. Our proposed models, which were derived in the previous chapter, are used to estimate the chirp-rates of each component coarsely. Then, a fast and accurate estimate-and-subtract strategy is applied to refine these parameters.

We will show that by using the mathematical model derived in the previous chapter to estimate the chirp-rates coarsely, we can achieve improved performance and a decreased SNR breakdown threshold.

The fast search algorithm or blind search algorithms often encounter challenges such as a high SNR breakdown threshold and the risk of converging to a local maximum. These issues arise due to nonlinearity caused by other components or high levels of noise. To address these drawbacks, the proposed algorithm utilizes an analytical model during the coarse step. This model functions as a filter, effectively identifying the peaks that correspond to the components and mitigating the aforementioned challenges. Moreover, the proposed algorithm tackles the issues of error propagation and high computational cost associated with other algorithms. This is achieved by leveraging the accurate estimation provided by the coarse estimation step, which avoids additional computational overhead. As a result, the estimate-and-subtract strategy can be employed in the fine estimation step, effectively eliminating the effects of error propagation and bias without incurring any additional computational cost.

Simulation results indicate that our proposed algorithm performs nearly at the CRLB,

eliminates the leakage effect between components, has no error propagation, and has an acceptable computational cost compared to other state-of-the-art methods. All of these outcomes have been verified by extensive computer simulations that closely resemble real-world applications, without incurring any additional computational cost.

6.2 Chirp-Rates Estimation Algorithm for Multi-Component LFM Signals

The functions $\widetilde{P}(\alpha)$ and $\widetilde{P}_K(\alpha)$, defined in (5.19) and (5.45) respectively, have been widely used for chirp-rate estimation in several studies, such as [104, 106, 114]. Although $\widetilde{P}_K(\alpha)$ has K distinct spikes that correspond to K different chirp-rates and locating their indexes provides an estimate of the chirp-rates, accurately determining the positions of these spikes is a challenging task. Therefore, in this section, we propose a novel idea to estimate the chirp-rates of multi-component LFM signals. We demonstrate that the model we derived in Theorem 7 is a potent tool for estimating the parameters of multi-component LFM signals. Our algorithm comprises coarse and fine estimation steps that employ a sequential estimate-and-subtract strategy. Our proposed algorithm consists of two steps: coarse estimation and fine estimation using a sequential estimate-and-subtract strategy. In the coarse estimation step, we estimate the chirp-rates and amplitudes of all K components of the LFM signal based on our derived models. Then, in the fine estimation step, we employ the estimate-and-subtract strategy to estimate each chirp-rate accurately, one component at a time, while removing the influence of the other pre-estimated components. This approach reduces bias and provides accurate estimations at each iteration. The estimate-and-subtract strategy is repeated Q times until the performance converges. Simulation results demonstrate that our algorithm performs close to the CRLB. The following sections will provide a detailed explanation of these two steps.

6.2.1 Coarse Estimation Step

The algorithm starts by computing an estimate of the variance by the maximum likelihood estimator [119]

$$\widehat{\sigma}^2 = \frac{1}{N}\sum_{n=0}^{N-1} |\widetilde{s}_K(n)|^2, \tag{6.1}$$

where $\widetilde{s}_K(n)$ is the discrete version of $\widetilde{s}_K(t)$ and N is the number of samples. Then, using (5.45), $\widetilde{P}_K(\alpha)$ is computed at M values of α. $\widetilde{P}_K(\alpha)$ is computed just once and will be used in all the following steps.

During the zeroth iteration, also known as the coarse estimation step, we minimize the difference between the observed $\widetilde{P}_K(\alpha)$ and our model $\widetilde{\Omega}_K(\alpha;\widehat{\mathbf{m}})$ to search for the values of chirp-rates. The following cost function can be minimized to perform this task.

$$\widehat{\mathbf{m}} = \underset{\widehat{\mathbf{m}}}{\operatorname{argmin}} \sum_{\alpha} \left(\widetilde{P}_K(\alpha) - \widetilde{\Omega}_K(\alpha;\widehat{\mathbf{m}})\right)^2, \tag{6.2}$$

where, $\widehat{\mathbf{m}} = [\widehat{m}_1, \widehat{m}_2, \cdots, \widehat{m}_K]$ is the vector containing the estimated values of chirp-rates. Searching within a K-dimensional search space, as required in the above minimization, is computationally prohibitive, particularly when K is large. To overcome this, we propose a more computationally efficient approach where we search the one-dimensional search space K times.

We estimate the coarse chirp-rate of the strongest component, which is typically the first component, by

$$\widehat{m}_1^{(0)} = \underset{m}{\operatorname{argmin}}\, \zeta_K(m), \tag{6.3}$$

where

$$\zeta_K(m) = \sum_{\alpha} \left(\widetilde{P}_K(\alpha) - \widetilde{\Omega}(\alpha;m)\right)^2. \tag{6.4}$$

To estimate the coarse chirp-rate of the first component, we compute $\zeta_K(m)$ at M different values of m. The value of m that minimizes $\zeta_K(m)$ is then taken as the coarse estimation of the first chirp-rate, denoted by $\widehat{m}_1^{(0)}$. Fig. 6.2 illustrates how the cost function $\zeta_K(m)$ is computed during the coarse estimation process. We start from m_1 and use the model $\widetilde{\Omega}(\alpha;m_1)$ with its maximum value at α_{opt_1} to obtain one point in the cost function $\zeta_K(m)$. This process is repeated for all values of m until the last value in the domain is reached. Furthermore, in Fig. 6.3, we can observe the cost function $\zeta_K(m)$ for estimating the first component. The minimum value of the cost function corresponds to the coarse estimate of the first component's chirp rate. To obtain the coarse estimation of the first component's amplitude, $\widehat{A}_1^{(0)}$, we select the maximum value of $\widetilde{P}_K(\alpha)$, denoted as $\widetilde{P}_K(\alpha,\widehat{m}_1^{(0)})$, which corresponds to the estimated chirp rate, $\widehat{m}_1^{(0)}$, in $\widetilde{P}_K(\alpha)$. Thus $\widehat{A}_1^{(0)}$ is

$$\left|\widehat{A}_1^{(0)}\right|^2 = \frac{\widetilde{P}_K(\alpha,\widehat{m}_1^{(0)}) - \widehat{\sigma}^2 T \csc(\widehat{\alpha}_1^{(0)})}{T^2\sqrt{1+\widehat{m}_1^{(0)2}}}, \tag{6.5}$$

where $\widehat{\alpha}_1^{(0)}$ is computed by (2.12). After obtaining the coarse estimations for the chirp-rate and amplitude of the first component, the model of the first component, $\Omega(\alpha;\widehat{m}_1^{(0)})$, is derived and subtracted from $\widetilde{P}_K(\alpha)$ to obtain the residual signal, denoted as $\widetilde{P}_{K-1}(\alpha)$.

$$\widetilde{P}_{K-1}(\alpha) = \widetilde{P}_K(\alpha) - \Omega(\alpha;\widehat{m}_1^{(0)}). \tag{6.6}$$

The algorithm returns to (6.4), in which $\widetilde{P}_K(\alpha)$ is replaced with $\widetilde{P}_{K-1}(\alpha)$ to obtain the cost function for estimating the second chirp-rate and amplitude.

$$\zeta_{K-1}(m) = \sum_{\alpha} \left(\widetilde{P}_{K-1}(\alpha) - \widetilde{\Omega}(\alpha; m)\right)^2. \tag{6.7}$$

The algorithm iterates until all K components' chirp-rates and amplitudes are sequentially estimated. The generalized coarse parameter estimation algorithm proceeds as follows: when estimating the parameters of the k-th component, the coarse estimation of the chirp-rate is obtained by minimizing the cost function

$$\widehat{m}_k^{(0)} = \underset{m}{\operatorname{argmin}} \sum_{\alpha} \left(\widetilde{P}_{K-k+1}(\alpha) - \widetilde{\Omega}(\alpha; m)\right)^2, \tag{6.8}$$

where

$$\widetilde{P}_{K-k}(\alpha) = \widetilde{P}_{K-k+1}(\alpha) - \Omega(\alpha; \widehat{m}_{K-k+1}^{(0)}), \tag{6.9}$$

in which

$$\left|\widehat{A}_k^{(0)}\right|^2 = \frac{\widetilde{P}_K(\alpha, \widehat{m}_k^{(0)}) - \widehat{\sigma}^2 T \csc(\widehat{\alpha}_k^{(0)})}{T^2\sqrt{1 + \widehat{m}_k^{(0)2}}}. \tag{6.10}$$

Once the coarse estimation is done for all the chirp-rates and amplitudes of the K components, the fine estimation algorithm is applied to obtain more accurate estimates. The coarse estimates are used as initial values to perform the fine estimation.

The resolution in the chirp-rate domain during the coarse estimation step is determined by the chirp search space $\mathscr{M}$, which consists of the chirp-rate values where the cost function $\zeta_K(m)$ is computed for each component. The number of chirp-rates in $\mathscr{M}$ is determined by the chirp-rate step Δm. Therefore, if $\zeta_K(m)$ is evaluated at M values of m from m_s to m_e, then Δm can be obtained by:

$$\Delta m = \frac{m_e - m_s}{M}. \tag{6.11}$$

A finer chirp-rate step in the coarse estimation step leads to more accurate estimation results.

Fig. 6.3 displays the Δm steps that determine the chirp rates at which the cost function will be evaluated. The resolution in the α domain, on the other hand, is related to the angle search space, $\mathscr{A}$, which contains the rotation angles used to numerically compute the FrFT and form $\widehat{P}_K(\alpha)$. The number of rotation angles in $\mathscr{A}$ is determined

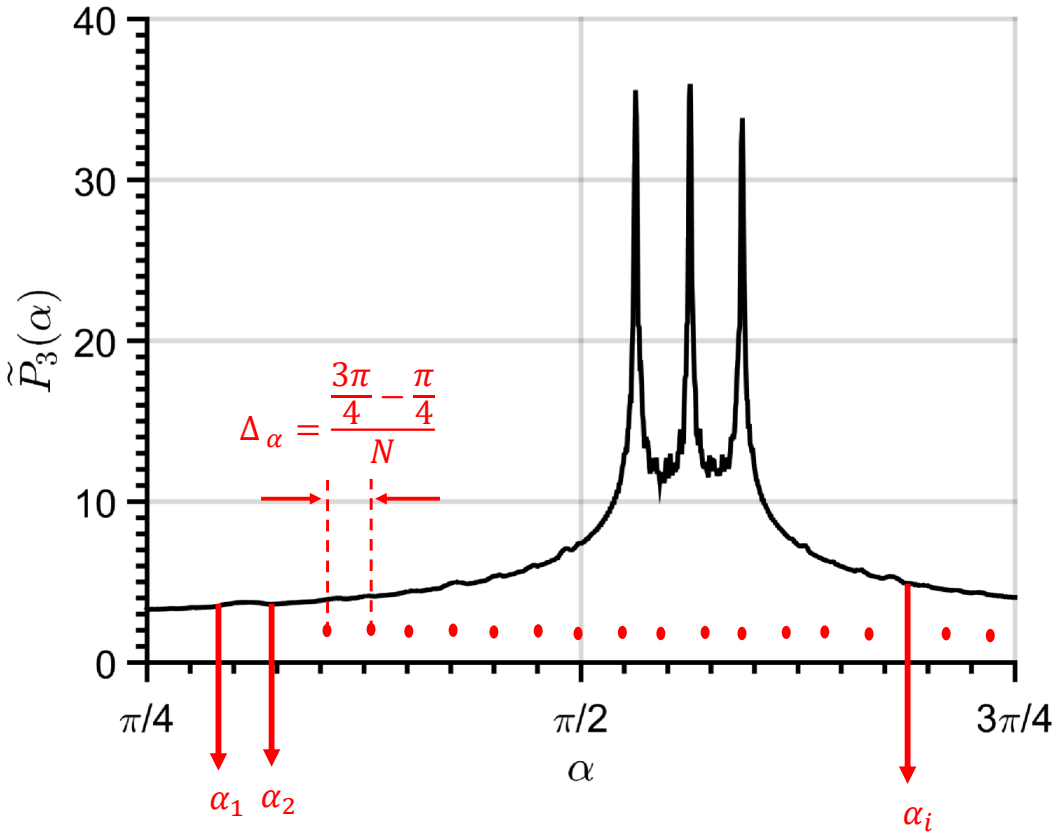

Figure 6.1 $\widetilde{P}_K(\alpha)$ for a three-component LFM signal with chirp-rates $\mathbf{m} = [0.1, 0.2, 0.3]^T$, $\widetilde{P}_3(\alpha)$, and $\Delta\alpha$.

by the rotation angle step, $\Delta\alpha$. Therefore, if $\widetilde{P}_K(\alpha)$ is computed at M values of α starting with α_s until α_e, then $\Delta\alpha$ is calculated by

$$\Delta\alpha = \frac{\alpha_e - \alpha_s}{M}. \tag{6.12}$$

A smaller step size in the angle domain results in a finer resolution and more accurate estimation in the coarse estimation step, but this also comes at the expense of increased computational cost. The coarse phase of the estimation process achieves an estimation accuracy of $O(M^{-1})$. Fig. 6.1 shows the plot of $\widetilde{P}_K(\alpha)$ for a three-component LFM signal with chirp-rates $\mathbf{m} = [0.1, 0.2, 0.3]^T$. Since $K = 3$ in this case, the function plotted is $\widetilde{P}_3(\alpha)$. The figure also displays the $\Delta\alpha$ steps, which determine the rotation angles at which the FrFT is computed to form $\widetilde{P}_3(\alpha)$. The maximum magnitude at each rotation angle is taken to obtain one point in the function $\widetilde{P}_3(\alpha)$.

6.2.2 Fine Estimation Step

The GSS algorithm was utilized in [114] for efficient and precise chirp-rate estimation. By taking advantage of the convexity property of $\widetilde{P}_K(\alpha)$ in the dominant signal region,

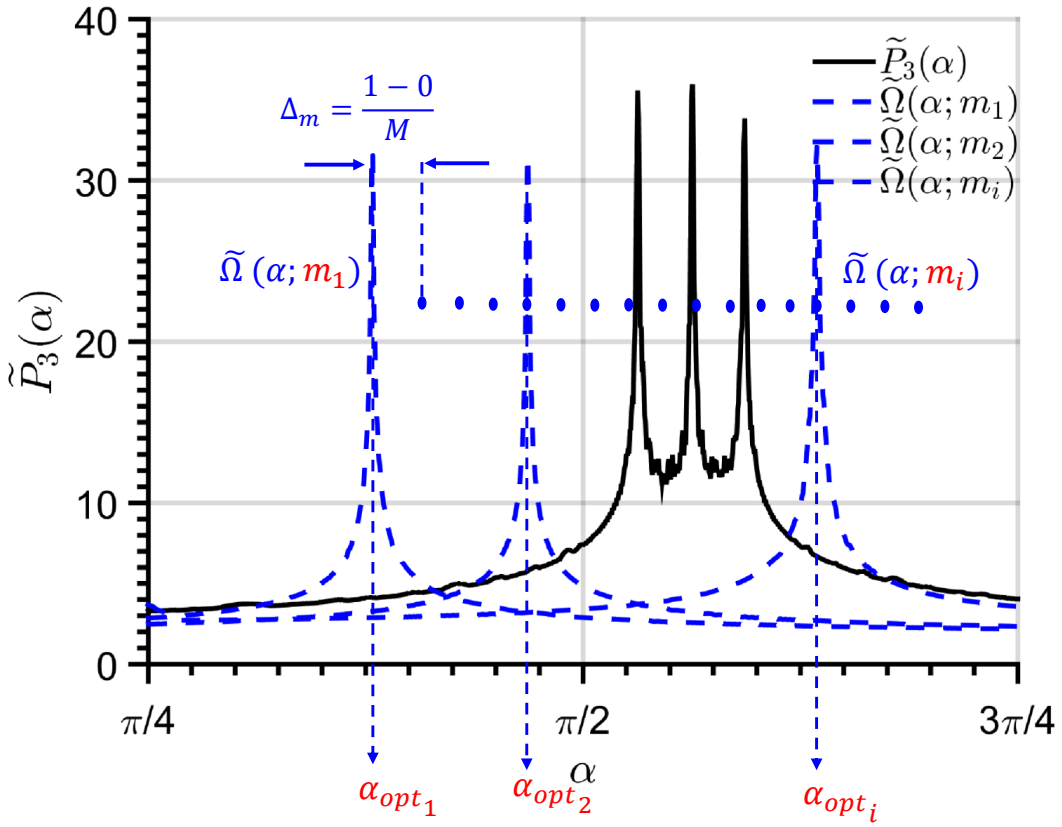

Figure 6.2 Coarse estimation algorithm.

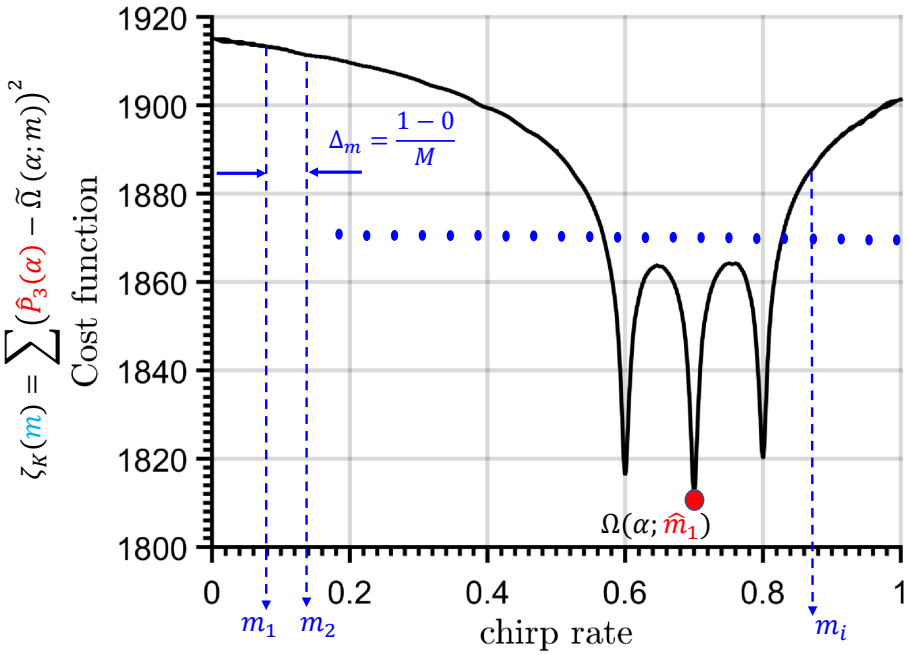

Figure 6.3 Cost Function for three-component LFM signal.

the GSS algorithm can quickly and accurately determine the maximum values with an optimized number of iterations [104]. We also utilize the GSS algorithm in the fine-estimation step to estimate the parameters of a multi-component LFM signal. Since the chirp-rates have already been estimated in the coarse estimation step, we can coarsely estimate the initial frequencies of the LFM signal one by one using a dechirping process followed by a sinusoidal frequency estimation algorithm, such as AME [124] or HAQSE [125]. For the k—th component in the LFM signal the coarse estimated initial frequency $\widehat{f}_k^{(0)}$ is

$$\widehat{f}_k^{(0)} = \text{AME}(\widetilde{s}_K(t) \times e^{-j\pi\widehat{m}_k^{(0)}t^2}). \tag{6.13}$$

We utilize the estimate-and-subtract technique, which involves estimating the chirp-rate of a single component in each iteration by eliminating all other components from the LFM signal using the coarsely estimated parameters. This allows for improved and more precise estimation of the chirp-rate of the particular component as the algorithm progresses. The resulting LFM signal, after removing all components except for the first one, is then used for the estimation of the first component's parameters.

$$\widetilde{s}(t) = \widetilde{s}_K(t) - \sum_{q=2}^{K} |\widehat{A}_q^{(0)}| e^{j\pi\left(\widehat{m}_q^{(0)}t^2 + 2\widehat{f}_q^{(0)}t\right)}. \tag{6.14}$$

Next, the fine estimation algorithm is exclusively applied to $\widetilde{s}(t)$. By doing so, the bias effect caused by the other components on the first component is minimized. By restricting the GSS search range to the neighborhood around the coarse estimated value of the first component's chirp-rate, $m_k^{(0)}$, the number of iterations required for accurate fine estimation is reduced. Therefore, only a limited number of GSS iterations are needed. The fine estimation of the first component chirp-rate is

$$m_1^{(1)} = GSS(\widetilde{s}(t), R). \tag{6.15}$$

Where R is the range of search which is equal to

$$R = \left[\widehat{\alpha}_1^{(0)} - \frac{\Delta\alpha}{2}, \widehat{\alpha}_1^{(0)} + \frac{\Delta\alpha}{2}\right], \tag{6.16}$$

and $\widehat{\alpha}_1^{(0)}$ is computed by (2.12) using $\widehat{m}_1^{(0)}$. The tuning of the range is based on the accuracy of the coarse estimation output. Once all the LFM chirp-rates are estimated, the algorithm repeats the process from the first component, following the same steps for each component. With each iteration, the bias effect between the components decreases, leading to improved estimation accuracy. The fine parameter estimation algorithm can be generalized as follows. The estimation of the k-th component

parameters at the i-th iteration starts by removing the all the components from the LFM signal except for the component k as

$$\widetilde{s}(t) = \widetilde{s}_K(t) - \sum_{\substack{q=1 \\ q \neq k}}^{K} |\widehat{A}_q^{(i-1)}| e^{j\pi\left(\widehat{m}_q^{(i-1)} t^2 + 2\widehat{f}_q^{(i-1)} t\right)}, \tag{6.17}$$

where $\widehat{A}_q^{(i-1)}$ and $\widehat{f}_q^{(i-1)}$ are computed by the following

$$\widehat{f}_q^{(i-1)} = \mathrm{AME}(\widetilde{s}_K(t) \times e^{-j\pi\widehat{m}_k^{(i-1)} t^2}). \tag{6.18}$$

$$\left|\widehat{A}_k^{(i-1)}\right|^2 = \frac{\widetilde{P}_K(\alpha, \widehat{m}_k^{(i-1)}) - \widehat{\sigma}^2 T \csc(\widehat{\alpha}_k^{(i-1)})}{T^2 \sqrt{1 + \widehat{m}_k^{(i-1)2}}}. \tag{6.19}$$

Then the chirp-rate of the k-th component at the i-th iteration is

$$m_k^{(i)} = GSS(\widetilde{s}(t), R). \tag{6.20}$$

Where R is

$$R = [\widehat{\alpha}_k^{(i-1)} - \frac{\Delta\alpha}{2}, \widehat{\alpha}_k^{(i-1)} + \frac{\Delta\alpha}{2}]. \tag{6.21}$$

The algorithm terminates once the difference between the current estimated value and the previous estimated value of any chirp-rate is smaller than a predefined threshold ϵ.

The pseudo-code for the algorithm is provided in Algorithm 3.

Our algorithm makes significant contributions to the field of chirp-rate estimation in multi-component LFM signals, particularly in the presence of noise. These contributions can be summarized as follows. Coarse estimation with derived models: We present a dual-phase approach. This is accomplished through the utilization of purpose-built models tailored to this task. Leveraging these models yields enhanced accuracy in estimations when contrasted with conventional blind search algorithms. Functioning akin to matched filters, these models identify accurate peaks within the PMF while mitigating noise interference. In the subsequent phase, rather than directly excluding components from the LFM signal, we employ the derived model to detect and subsequently eliminate peaks within the PFM. Moreover, our algorithm ensures computational efficiency, rendering it highly suitable for real-world applications. Refinement through estimate-and-subtract strategy: In the second step of our algorithm, we employ an estimate-and-subtract strategy to further refine the initial coarse estimates. This unique approach allows us to better distinguish between closely separated components and effectively eliminate error propagation and bias

Algorithm 3 The proposed algorithm for estimating the chirp-rates of a K-component chirp.

Input: $\widetilde{s}_K(n)=\widetilde{s}_K(t)|_{t=nT_s}$, $n=0,1,\cdots,N-1$,
Set:
Angle search space: $\mathscr{A}=\{\alpha_s,\alpha_s+\Delta\alpha,\cdots,\alpha_s+(M-1)\Delta\alpha\}$,
Chirp search space: $\mathscr{M}=\{m_s,m_s+\Delta m,\cdots,m_s+(M-1)\Delta m\}$,
Calculate $\widehat{\sigma}^2=\frac{1}{N}\sum_{n=0}^{N-1}|\widetilde{s}_K(n)|^2$,
Coarse Estimation of Parameters:
for each $\alpha\in\mathscr{A}$ **do**
$\widetilde{P}_K(\alpha)=\max_u\left\{|\mathscr{F}^\alpha\{\widetilde{s}_K(n)\}|^2\right\}$,
end for
for $k=1$ to K **do**
for each $m\in\mathscr{M}$ **do**
$\zeta_K(m)=\sum_{p=0}^{M-1}\left(\widetilde{P}_{K-k+1}(\alpha+p\Delta\alpha)-\widetilde{\Omega}(\alpha+p\Delta\alpha;m)\right)^2$,
end for
$\widehat{m}_k^{(0)}=\arg\min_m\zeta_K(m)$,
$\widehat{\alpha}_k^{(0)}=\arctan\left(\widehat{m}_k^{(0)}\right)+\frac{\pi}{2}$,
$\left|\widehat{A}_k^{(0)}\right|^2=\frac{\widetilde{P}_K(\alpha,\widehat{m}_k^{(0)})-\widehat{\sigma}^2NT_s\csc(\widehat{\alpha}_k^{(0)})}{N^2T_s^2\sqrt{1+\widehat{m}_k^{(0)2}}}$,
$\widetilde{P}_{K-k}(\alpha)=\widetilde{P}_{K-k+1}(\alpha)-\Omega(\alpha;\widehat{m}_k^{(0)})$,
$\widehat{f}_k^{(0)}=\mathrm{AME}(\widetilde{s}_K(n)\times e^{-j\pi\widehat{m}_k^{(0)}n^2T_s^2})/T_s$,
end for
Fine Estimation of Parameters:
Set: $i=1$
repeat
for $k=1$ to K **do**
$\widetilde{s}(n)=\widetilde{s}_K(n)-\sum_{\substack{q=1\\q\neq k}}^{K}|\widehat{A}_q^{(i-1)}|e^{j\pi\left(\widehat{m}_q^{(i-1)}n^2T_s^2+2\widehat{f}_q^{(i-1)}nT_s\right)}$,
$\widehat{\alpha}_k^{(i-1)}=\arctan\left(\widehat{m}_k^{(i-1)}\right)+\frac{\pi}{2}$,
$R=\left[\widehat{\alpha}_k^{(i-1)}-\frac{\Delta\alpha}{2},\widehat{\alpha}_k^{(i-1)}+\frac{\Delta\alpha}{2}\right]$,
$\widehat{m}_k^{(i)}=GSS(\widetilde{s}(n),R)$,
$\widehat{f}_k^{(i)}=\mathrm{AME}(\widetilde{s}_K(n)\times e^{-j\pi\widehat{m}_k^{(i)}n^2T_s^2})/T_s$,
$\left|\widehat{A}_k^{(i)}\right|^2=\frac{\widetilde{P}_K(\alpha,\widehat{m}_k^{(i)})-\widehat{\sigma}^2NT_s\csc(\widehat{\alpha}_k^{(i)})}{N^2T_s^2\sqrt{1+\widehat{m}_k^{(i)2}}}$,
end for
$i=i+1$,
until convergence
return $\widehat{m}=[\widehat{m}_1^{(i)},\widehat{m}_2^{(i)},\cdots,\widehat{m}_K^{(i)}]^T/T_s^2$

effects. By selectively removing the peaks while preserving the original signal, we achieve more accurate chirp-rate estimation.

6.3 Computational Cost

The computational complexity of the algorithm is largely determined by the number of FrFT operations required to estimate the chirp-rates of the K components in both the coarse and fine steps. In the coarse step, the computational cost to estimate the K components is proportional to $\mathcal{O}(M \times N \log N)$, where $\mathcal{O}(N \log N)$ is the computational cost of a single FrFT [101]. Since the function $\widetilde{P}_k(\alpha)$ is computed once and used for all K components, the computational cost is fixed for any number of components. In the fine step and according to [104], the computational cost for a mono-component and one iteration is

$$\left\lceil \frac{\log\left(\frac{N^{-3}}{N^{-1}}\right)}{\log(r)} \right\rceil \mathcal{O}(N \log N) = \left\lceil \frac{2 \log N}{\log(1/r)} \right\rceil \mathcal{O}(N \log N), \tag{6.22}$$

where $\lceil . \rceil$ is the ceiling function and r is the golden ratio, $r = \frac{\sqrt{5}-1}{2}$. According to our simulations, the fine phase estimator iterates between $2-3$ times. Therefore, for a K-component LFM signal, the total computational cost of the fine phase is

$$\mathcal{O}(K \times N \log^2 N). \tag{6.23}$$

The total computational cost of the proposed algorithm for a K component LFM signal is

$$\mathcal{O}(M \times N \log N) + \mathcal{O}(K \times N \log^2 N). \tag{6.24}$$

We assumed $M = N$, and in most practical applications, $K \log N \ll M$. Hence, the computational complexity of estimating all parameters is on the order of $\mathcal{O}(N^2 \log N)$. The computational complexity of the LVD algorithm is also on the order of $\mathcal{O}(N^2 \log N)$ [60]. In contrast, the computational complexity of the PHAF algorithm is $\mathcal{O}(K \times P \times N \log N)$ [126], where P is the number of lags. The PHAF algorithm may require less computational cost than our proposed algorithm and LVD algorithm, but at the expense of accuracy and performance. We will detail the performances of these algorithms in the next section. Additionally, it is useful to compare our proposed algorithm with a PFM maximum search (PFMMS)-based algorithm, which estimates the chirp-rates of a multi-component LFM signal by searching for the indices of the maximum values in $\widetilde{P}_K(\alpha)$.

6.4 Simulations

To evaluate the performance of our proposed algorithm, we conducted five different experiments comparing it with the PHAF [33] and LVD [58] algorithms, as well as a PFMMS-based algorithm. In practical scenarios, all chirp-rates are typically within the range of $[-1,1]$ after sampling [53]. Therefore, we limited α to the range $\alpha \in [\pi/4, 3\pi/4]$, with $M = N$ to ensure coarse phase estimation accuracy of $\mathcal{O}(N^{-1})$, which guarantees the fine estimator to converge to CRLB. The sampling rate was set to $T_s = \frac{1}{\sqrt{N}}$, and we chose $\epsilon = N^{-3}$ to achieve optimal accuracy for chirp rate estimation, which is on the order of $N^{-5/2}$. The MSE is

$$MSE_k = \frac{1}{C}\sum_{\nu=1}^{C}(\widehat{m}_k - m_k)^2, \tag{6.25}$$

where $C = 3000$ was taken as the number of Monte Carlo simulations for all the simulations.

6.4.1 The First Experiment: Many Components

In this experiment, we assessed the performance of our proposed algorithm for estimating an 8-component LFM signal with varying chirp-rates. All components had the same amplitude, with chirp-rates selected as $\mathbf{m} = [-0.3, -0.2, -0.1, -0.05, 0.05, 0.1, 0.2, 0.3]^T$, and initial frequencies $\mathbf{f} = [0.2, 0.1, 0, 0, 0, 0, -0.1, -0.2]^T$, and signal length $N = 1024$. As the performance of all components was similar, we plotted the performance of a single component.

Fig. 6.4 illustrates the performance of our algorithm compared to PFMMS, PHAF, and LVD algorithms. Our algorithm has a low breakdown threshold of $-9dB$, much lower than PFMMS, PHAF, and LVD. Additionally, our algorithm follows the CRLB, while there is a gap between the CRLB and the performance of PHAF and PFMMS. There are two reasons for the performance degradation in PFMMS compared to the proposed algorithm. Firstly, PFMMS searches for the first 8 maxima in $\widetilde{P}_K(\alpha)$, without any guarantee that these maxima do not contain high noise peaks. In contrast, the proposed algorithm matches the signal dominant area for each component using $\widetilde{\Omega}(\alpha; m)$, which eliminates noise. To clarify the point, Fig. 6.5 displays the $\widetilde{P}_8(\alpha)$ function for the 8-component LFM signal in the absence of noise. The figure reveals eight distinct peaks that correspond to the eight chirp rates of the LFM signal. Furthermore, Fig. .6.6 illustrates the cost function for the noiseless case, where the figure displays distinct minimums that correspond to the chirp rates. In contrast, Fig. 6.7 shows the $\widetilde{P}_8(\alpha)$ function for the 8-component LFM signal in the presence of noise. The figure indicates that there are more than one peak, which are bigger

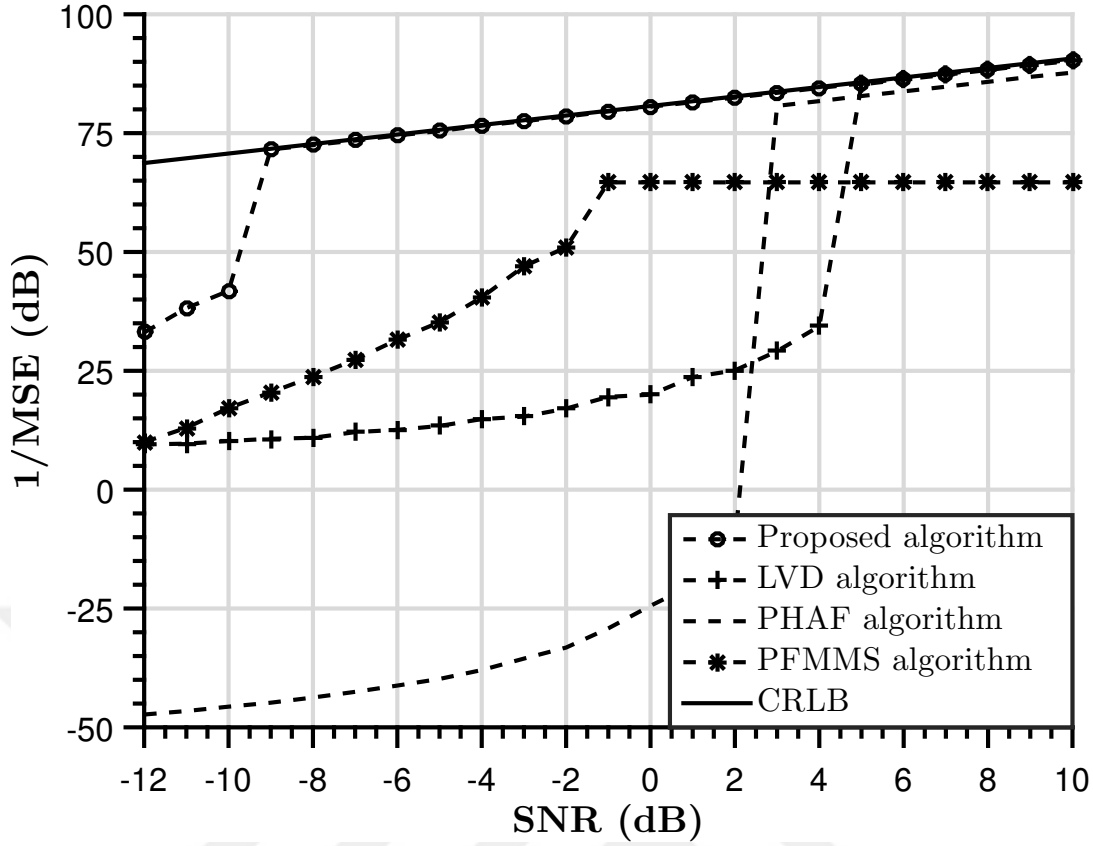

Figure 6.4 Performance comparison of our proposed algorithm with respect to SNR when the number of components is $K = 8$ and $N = 1024$.

than the peaks associated with the chirp rates. This implies that any PFMMS-based algorithm will miss at least two components in the estimation process, regardless of the considerable computational cost that these algorithms entail, as the estimate and remove terminology will result in eight times extra computational cost. However, Fig. 6.8 displays the cost function for the same case. It is evident that the same minimums corresponding to the chirp rates are still distinct, and the impact of noise has been reduced. This is because the model $\widetilde{\Omega}(\alpha; m)$ functions as a filter that allows the signal's dominant area related to each chirp rate to pass and eliminates the noise peaks. Therefore, we can conclude that the model $\widetilde{\Omega}(\alpha; m)$ operates as a matched filter for the signal dominant area corresponding to each component, and this explains the proposed algorithm's ability to eliminate noise. The second reason for the proposed algorithm's effectiveness is the terminology it employs, which allows for the reuse of $\widetilde{P}_K(\alpha)$ to eliminate the estimated component and reuse the $\widetilde{P}_K(\alpha)$.

6.4.2 The Second Experiment: Closely Separated Chirp Rates

In this particular experiment, we conducted a thorough evaluation of our algorithm's performance in a scenario involving closely separated chirp rates. To simulate

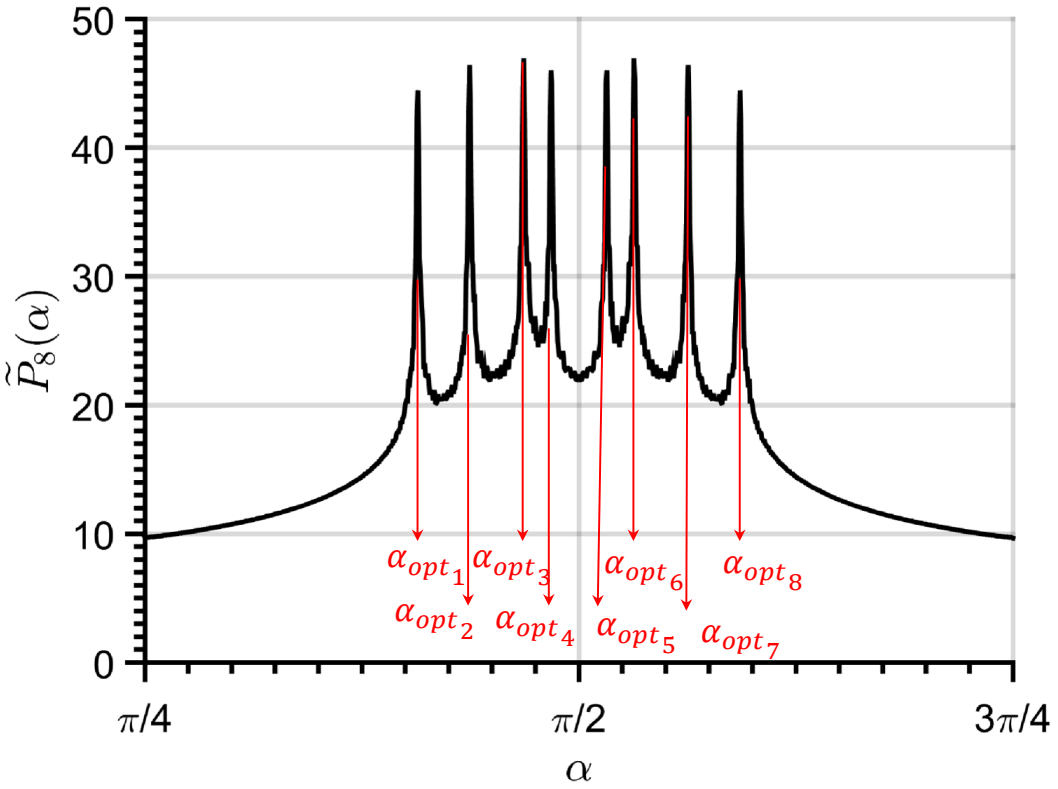

Figure 6.5 $\widetilde{P}_K(\alpha)$ for an eight-component LFM signal with chirp-rates $\mathbf{m} = [-0.3, -0.2, -0.1, -0.05, 0.05, 0.1, 0.2, 0.3]^T$, $\widetilde{P}_8(\alpha)$, in noiseless case.

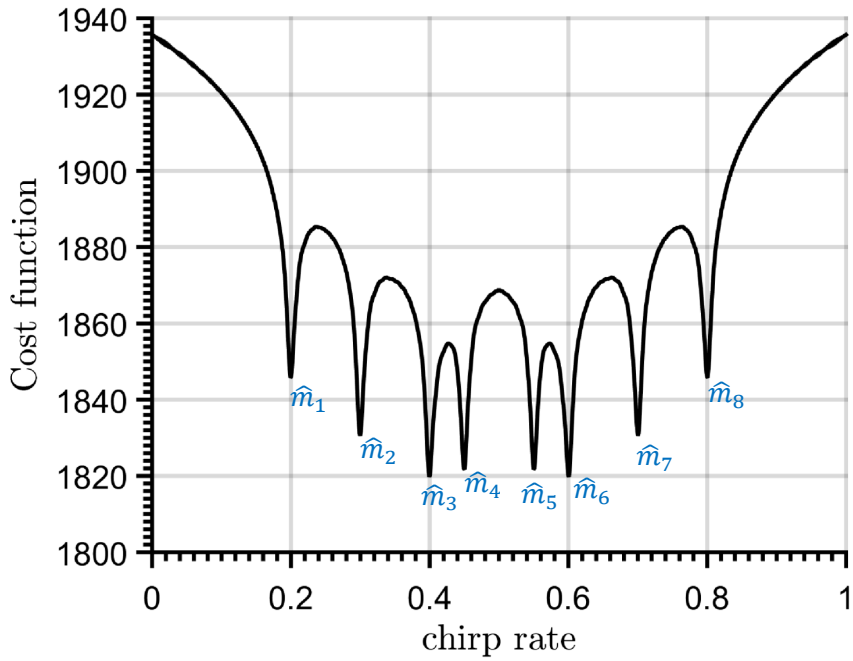

Figure 6.6 Cost function for eight-component LFM signal in noiseless case.

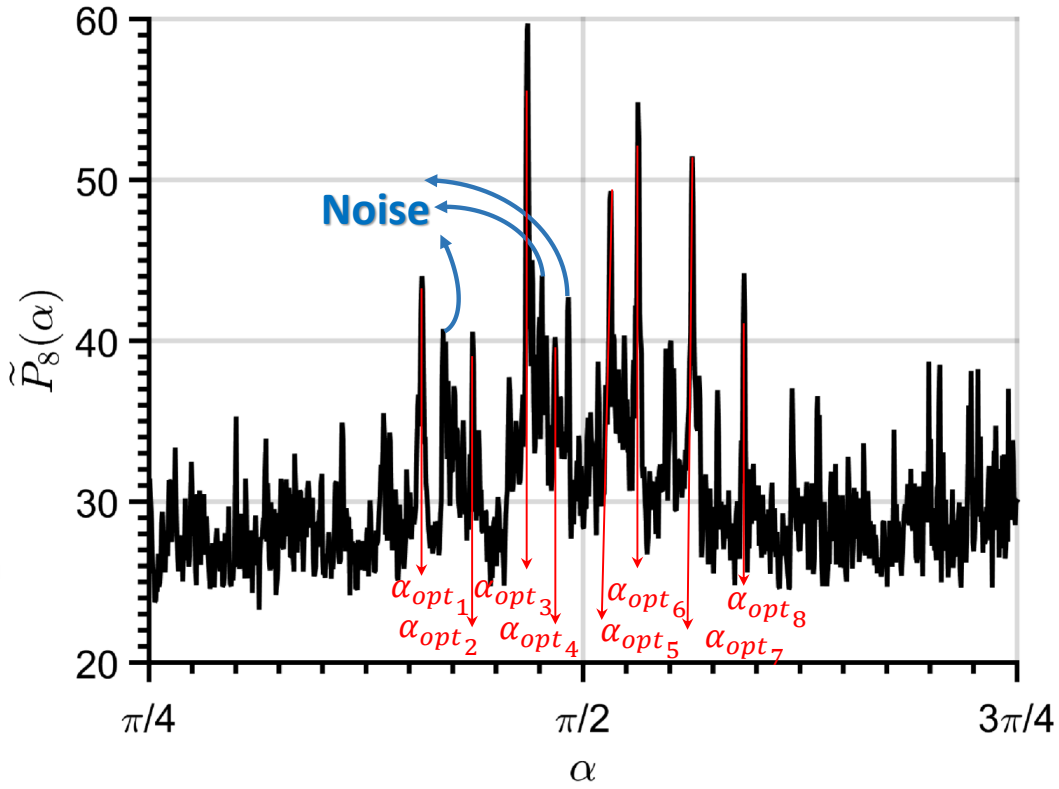

Figure 6.7 $\widetilde{P}_K(\alpha)$ for an eight-component LFM signal with chirp-rates $\mathbf{m} = [-0.3, -0.2, -0.1, -0.05, 0.05, 0.1, 0.2, 0.3]^T$, $\widetilde{P}_8(\alpha)$, in noisy case.

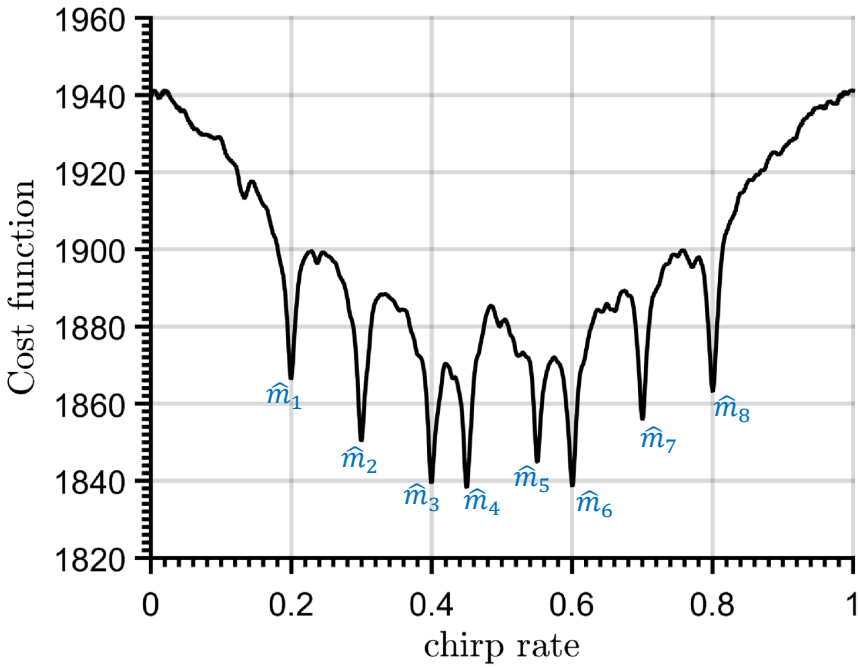

Figure 6.8 Cost function for eight-component LFM signal in noisy case.

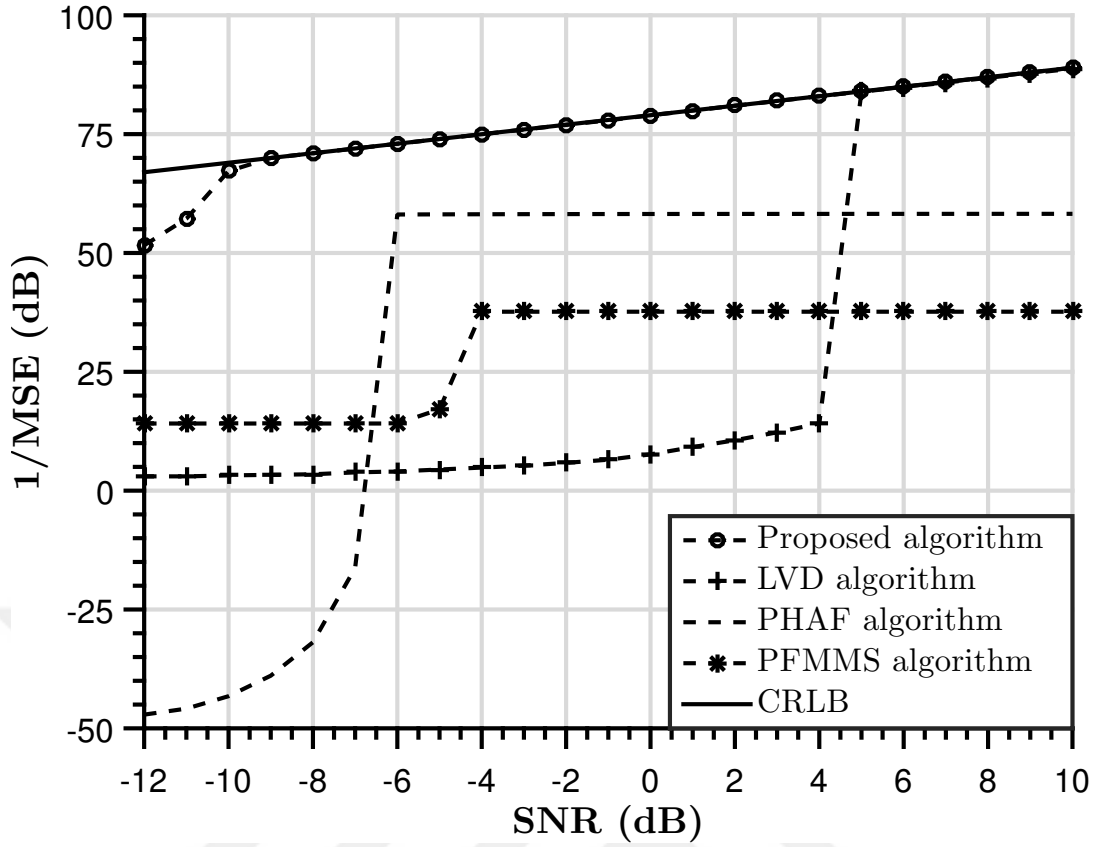

Figure 6.9 Performance comparison of our proposed algorithm with respect to SNR for a closely separated bi-component LFM signal, $N = 1024$.

this scenario, we generated a bi-component chirp signal with chirp rates $\mathbf{m} = [0.02, 0.03]^T$ and initial frequencies $\mathbf{f} = [-0.01, 0]^T$. As the chirp rates were closely spaced, we numerically calculated the CRLB by using [119, Eq. 3.33]. The results of this experiment, shown in Fig. 6.9, demonstrate the remarkable performance of our algorithm. Even at low SNR as low as −10dB, our algorithm closely follows the CRLB. In contrast, the PHAF algorithm fails to track the CRLB and exhibits a significant leakage effect in its performance beyond an SNR breakdown threshold of approximately −6dB. On the other hand, the LVD algorithm demonstrates a relatively high SNR breakdown threshold of 5dB. Notably, the PFMMS algorithm separates the two components starting from an SNR of −4dB. The high performance of our algorithm in this experiment can be attributed to two crucial properties. First, incorporating the mathematical model in the estimation process enhances the algorithm's immunity against noise. Second, the accurate estimation during the coarse steps and the utilization of the model $\Omega(\alpha; \widehat{m}^{(0)})$ for the estimated component to remove peaks in the $\widetilde{P}_K(\alpha)$ domain (instead of directly removing components from the LFM signal) significantly improves our algorithm's ability to detect and recognize the closely separated chirp rates scenario.

6.4.3 The Third Experiment: Dependence on the Number of Samples for Closely Separated Chirp Rates

We conducted an experiment to assess how our algorithm's performance depends on the signal length N when the chirp-rates are closely spaced. We varied N logarithmically between 16 and 1024, while keeping the SNR constant at 10dB. To this end, we generated a four-component LFM signal with chirp-rates $\mathbf{m} = [0.01, 0.01 + \frac{12}{N}, 0.01 + \frac{24}{N}, 0.01 + \frac{36}{N}]^T$, and all initial frequencies were set to zero with equal amplitude for all components. Because the components are closely spaced, we computed the CRLB numerically using [119, Eq. 3.33].

As shown in Fig. 6.10, our algorithm closely follows the CRLB starting from around 100 samples, which is lower than the other methods, LVD, PHAF, and PFMMS. The proposed algorithm accurately estimated the chirp-rates around $N = 100$. Notably, we can refer to the corollary 6.1 in the previous chapter. The first experiment showed that there is an SNR threshold for a constant N, and here we see that there is also an N threshold for a constant SNR.

6.4.4 The Fourth Experiment: Dependence on the Chirp Separation

In this experiment, we evaluated the performance of our proposed algorithm in terms of its ability to separate closely spaced chirp-rates. This analysis gives insight into the

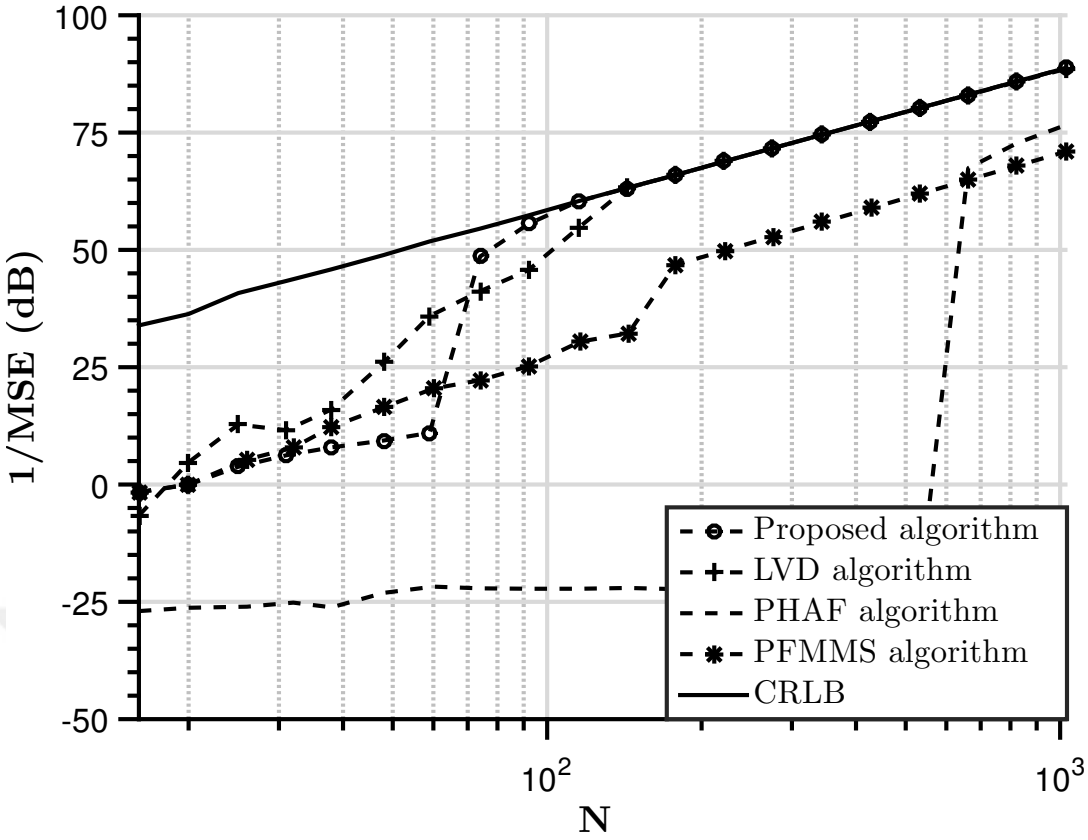

Figure 6.10 Performance comparison of our proposed algorithm with respect to N when the number of components $K = 5$ and SNR $= 10$dB.

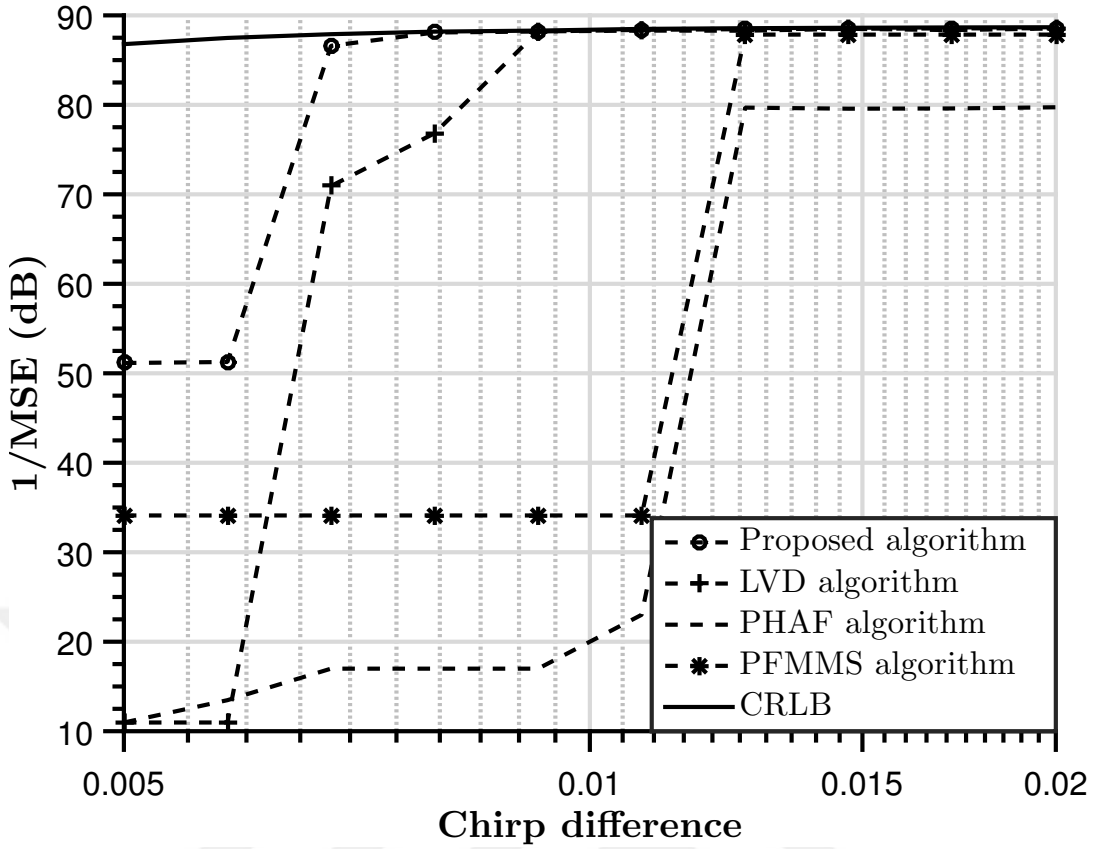

Figure 6.11 Performance comparison of our proposed algorithm for a bi-component chirp when the difference between chirp-rates is small.

separability of the proposed algorithm. We generated a bi-component LFM signal with amplitudes equal to unity and both initial frequencies set to zero. The performance of our algorithm was compared to PHAF, LVD, and PFMMS algorithms at a constant SNR of 8 dB and N = 1024, and the CRLB was computed numerically using [119, Eq.3.33] due to the closely spaced components. The results are plotted in Fig. 6.11, which shows that our proposed algorithm nearly follows the CRLB starting at a much lower chirp difference of approximately $|m_1 - m_2| = 0.007$, outperforming LVD, PHAF, and PFMMS.

The superior performance of our proposed algorithm can be attributed to its methodology. In estimate-and-subtract strategy-based algorithms, the estimated component is removed from the signal itself. Thus, in the presence of two closely spaced components, inaccurate estimation of the chirp-rate of the first component can impact the accuracy of the second component's estimation during removal. In contrast, our proposed algorithm uses the estimated chirp-rate to find the $\widetilde{\Omega}(\alpha; m)$ model, which is then used to remove the corresponding peak in $\widetilde{P}_K(\alpha)$ domain. Therefore, our algorithm has better ability to estimate the closely spaced components accurately.

6.4.5 The Fifth Experiment: Unequal Powers

In this experiment, we considered three-component LFM signals with unequal powers. The power difference between the first and second components was $5dB$, and the power difference between the first and third components was $10dB$. We selected the chirp-rates and initial frequencies as $\mathbf{m} = [-0.1, 0.1, 0.2]^T$ and $\mathbf{f} = [0, 0, -0.1]^T$. Fig. 6.12 shows the performance of our proposed algorithm compared to the PHAF, LVD, and PFMMS algorithms. Our proposed algorithm achieves the CRLB for much lower SNR breakdown thresholds. In this specific scenario, accurately estimating the weaker components becomes challenging due to the presence of stronger components that can overshadow them. However, our algorithm effectively addresses this issue by building upon the same underlying principles demonstrated in the first experiment. By integrating the mathematical model into the estimation process and employing the proposed estimate-and-subtract strategy, our algorithm excels at accurately estimating the parameters of each component, even when strong neighboring components are present. This adaptive approach enables our algorithm to account for the masking effect, accurately identifying and estimating the weaker components. As a result, our algorithm achieves improved performance and increased accuracy in this scenario. Additionally, we observe a consistent gap between the CRLB and the performance of the PHAF algorithm. Moreover, it is evident that the PFMMS algorithm struggles to

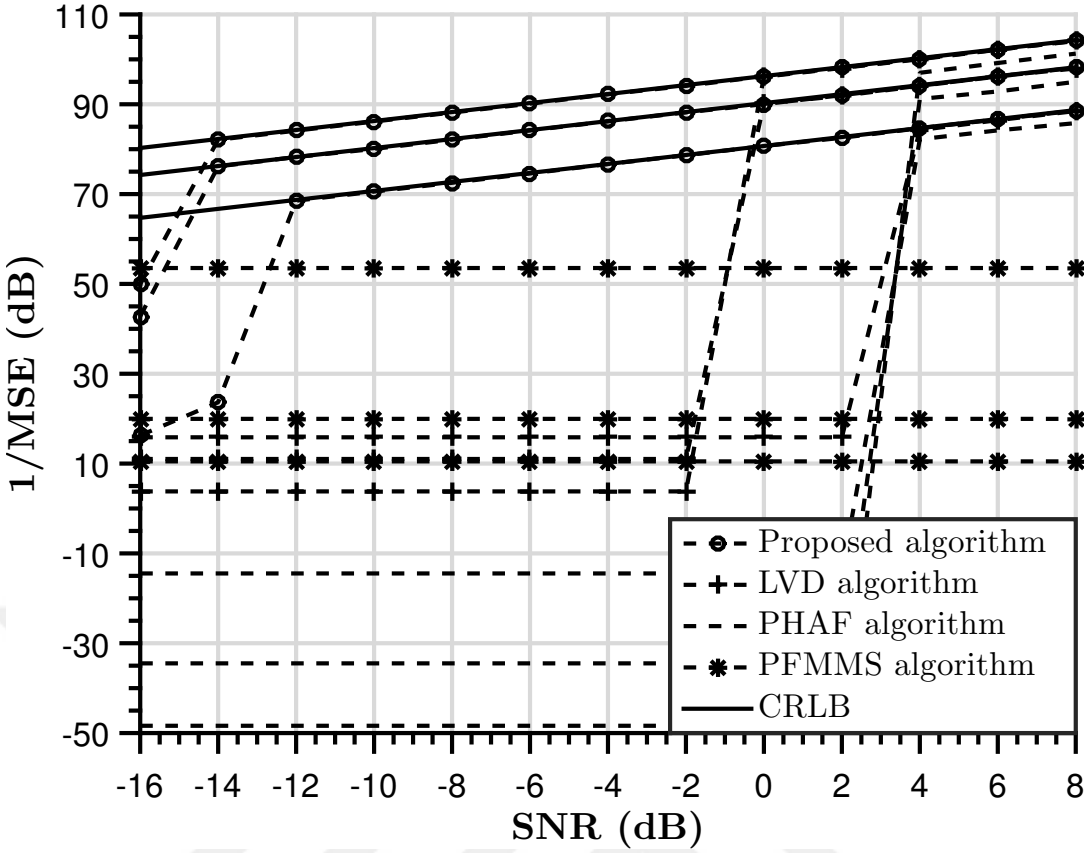

Figure 6.12 Performance comparison of our proposed algorithm for a three-component LFM signal with unequal powers.

accurately estimate the low-power components, which can be attributed to the same reasons discussed in the first experiment.

All five experiments consistently demonstrate the superior performance of the proposed algorithm compared to existing state-of-the-art methods. The algorithm exhibits several noteworthy capabilities. Firstly, it achieves the CRLB with a significantly lower SNR breakdown threshold, even in challenging scenarios involving LFM signals with multiple components. This improvement can be attributed to the fact that our search is guided by the mathematical model, as opposed to blind estimation. Additionally, the proposed algorithm excels in separating closely spaced chirp signals. This is accomplished through the incorporation of a unique and efficient removal strategy using the proposed models. Rather than removing the components directly from the LFM signal, we utilize the derived model to identify and eliminate peaks in the PFM domain. This strategic approach significantly enhances the algorithm's capability to handle challenging scenarios. Furthermore, the proposed algorithm demonstrates exceptional performance in cases where the power levels of LFM signal components vary considerably, resulting in masking effects on weaker components. This is made possible by employing the mathematical models in both phases of coarse estimation, enabling accurate parameter estimation and reducing the impact of masking. Lastly, the proposed algorithm exhibits the shortest convergence time to the CRLB among the tested methods, a topic that has been extensively discussed and supported mathematically.

6.5 Results and Discussion

We have developed a novel coarse-to-fine FrFT -based algorithm specifically for chirp-rate estimation in multi-component LFM signals. The algorithm leverages the derived mathematical models to achieve improved performance and an SNR breakdown threshold. By guiding the search process using the mathematical model, rather than relying on blind estimation, accurate estimation of the chirp-rates is achieved. To refine the estimated parameters, an efficient estimate-and-subtract strategy was incorporated into the algorithm. Instead of removing components directly from the LFM signal, the derived model is used to identify and eliminate peaks in the PFM. This unique approach enhances the algorithm's ability to handle challenging scenarios and mitigates the leakage effect between signal components, while avoiding error propagation. Simulation results show that our proposed algorithm performs nearly on the CRLB, has no error propagation, has an acceptable computational cost compared to other state-of-the-art methods, has lower SNR breakdown threshold, has better ability to estimate the chirp-rates of closely separated

components, can deal perfectly in the case of components with unequal powers mitigating the masking effect, and eliminates the leakage effect (shading) between components. Overall, this chapter contributes to the field of chirp-rate estimation in LFM signals by providing accurate models, a novel algorithm, and extensive simulation-based validation. The proposed approach offers a practical and efficient solution for real-world applications without imposing significant computational burden.

7
Chirp Rates Estimation Of Multi-component LFM Signals Using Non-Searching Fractional Fourier Transform Based Algorithm

7.1 Introduction

Our previous chapter involved the application of the suggested models for mono noisy and noiseless PFM, resulting in successful chirp rate estimations for multi-component LFM signals. These outcomes, as presented in Chapter 5 and Chapter 6, were published in [130]. In the current chapter, we introduce an innovative algorithm designed for estimating chirp rates using the proposed model for multi noisy PFM. Specifically, we integrate these expressions into a nonlinear least squares Levenberg-Marquardt (LM) algorithm, employing them as model functions to achieve precise chirp-rate estimations. This approach avoids the computational cost and error propagation issues associated with the CLEAN technique, which iteratively estimates and subtracts the parameters of the strongest component.

Simulation results demonstrate that the algorithm can handle closely separated components, as well as eliminate the shading effect between components. Overall, the proposed algorithm offers an efficient and accurate solution to the problem of estimating the chirp-rates of multi-component LFM signals.

7.2 Model Fitting Concept

The model fitting concept is a fundamental process in data analysis and involves selecting a mathematical model that can explain or predict a given set of data. The cost or error function measures the discrepancy between the data and the model, and the algorithm minimizes the cost function by adjusting the model parameters. There are different types of model fitting methods, such as linear regression and nonlinear regression, and the choice of method depends on the nature of the data and the model. The concept of model fitting involves determining the appropriate variables

of a mathematical expression to create the best model that fits a given dataset. This means selecting a particular model that uses specific variables to accurately represent the dataset. To achieve this, three key factors need to be identified: Firstly, a mathematical expression that is consistent with the dataset being analyzed. Secondly, a cost function or error function that can measure the difference between the dataset and the mathematical expression using the given parameters. Finally, an algorithm that can determine the variables that minimize the cost function [131].

We propose to use the model fitting concept to find the model which most fits $\widetilde{P}_K(\alpha)$. Regarding the mathematical expression, $\widetilde{\Omega}(\alpha;m)$ and $\widetilde{\Omega}_K(\alpha;\mathbf{m})$ are defined as the mathematical expressions of the data set. The cost function is defined by

$$\zeta(\widehat{\mathbf{m}}) = \left(\sum_{\alpha} \left(\widetilde{P}_K(\alpha) - \widetilde{\Omega}_K(\alpha;\widehat{\mathbf{m}}) \right)^l \right)^{1/l}. \tag{7.1}$$

Where, l is the order of the cost function, $\widehat{\mathbf{m}}$ is a vector contains the chirp rates of the individual components and $\widetilde{\Omega}_K(\alpha;\widehat{\mathbf{m}})$ is a vector contains noisy model samples defined by the chirp rates $\widehat{\mathbf{m}}$ for the K-component LFM signal. (7.1) represents the norm $\| \left(\widetilde{P}_K(\alpha) - \widetilde{\Omega}_K(\alpha;\widehat{\mathbf{m}}) \right) \|_l$. We should investigates the following cases

$$\begin{aligned} J_1 &: l = 1 \longrightarrow \sum_{\alpha} \left| \left(\widetilde{P}_K(\alpha) - \widetilde{\Omega}_K(\alpha;\widehat{\mathbf{m}}) \right) \right|. \\ J_2 &: l = 2 \longrightarrow \sqrt{\sum_{\alpha} \left(\widetilde{P}_K(\alpha) - \widetilde{\Omega}_K(\alpha;\widehat{\mathbf{m}}) \right)^2}. \\ J_\infty &: l \longrightarrow \infty \longrightarrow \max_{\alpha} \left| \left(\widetilde{P}_K(\alpha) - \widetilde{\Omega}_K(\alpha;\widehat{\mathbf{m}}) \right) \right|. \end{aligned} \tag{7.2}$$

Figure 7.1, Figure 7.2 and Figure 7.3 plot the three cost functions defined in the equation above for a mono component LFM signal. Where the SNR values were $10dB$, $0dB$ and $-10dB$. It is clear from the figures that the cost function J_2 is the best choice and more appropriate to be minimized.

7.3 Levenberg-Marquardt

The LM algorithm is an optimization method commonly used in curve fitting problems. It helps find the best-fit parameters for a mathematical model that minimizes the difference between the model's predictions and the actual data. The algorithm combines the benefits of two other methods: the Gauss-Newton (GN) method and the steepest descent (ST) method. It adjusts the step size during optimization to ensure stability and convergence. The GN method and ST method are two commonly used optimization algorithms for nonlinear curve fitting. The GN method is an iterative

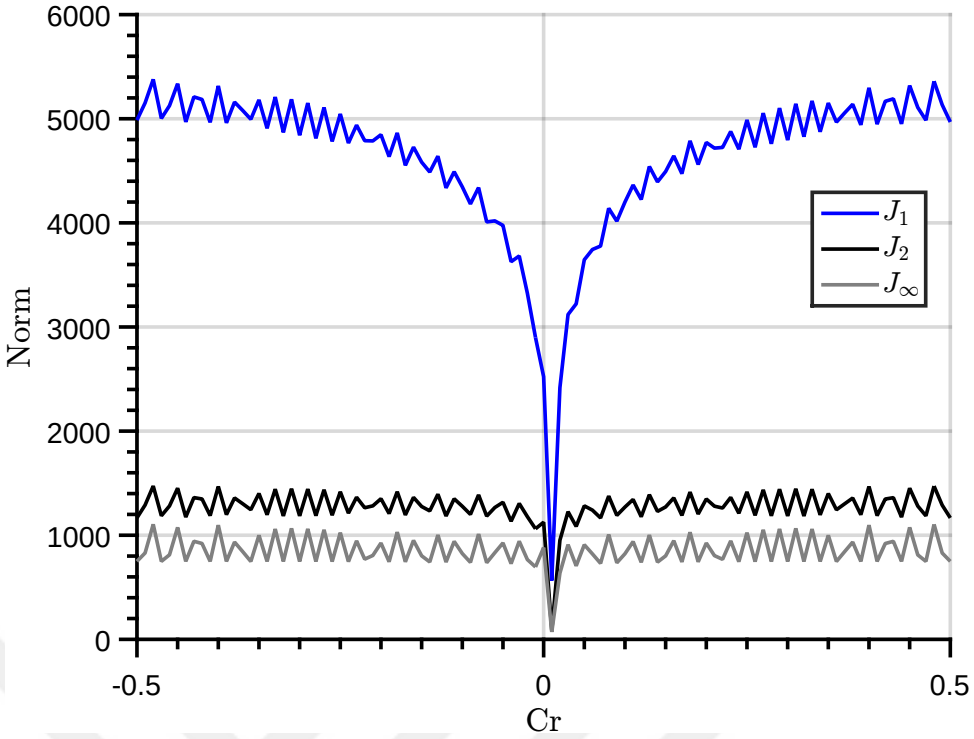

Figure 7.1 Cost functions when SNR=10dB.

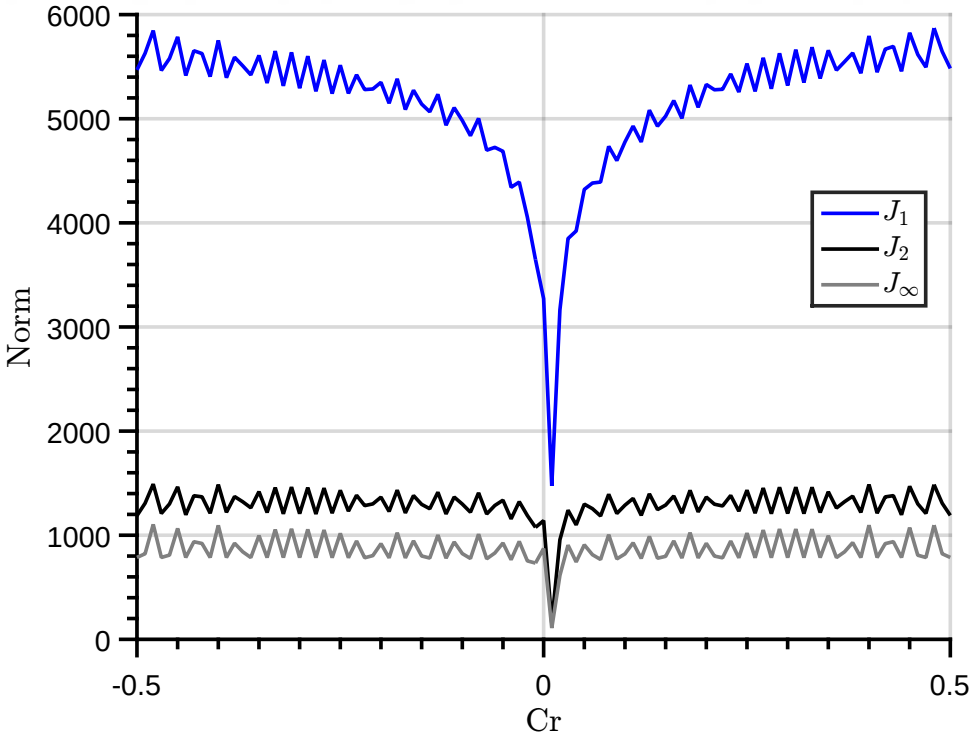

Figure 7.2 Cost functions when SNR= 0dB.

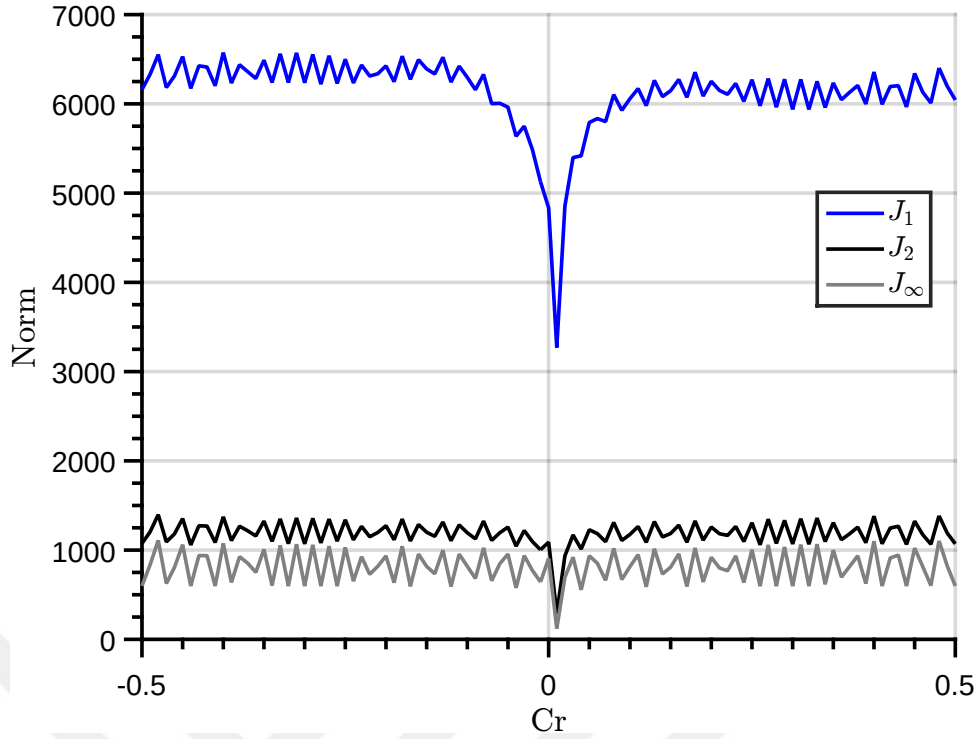

Figure 7.3 Cost functions when SNR=-10dB.

algorithm that approximates the objective function (typically the sum of squared errors between the data and the model) with a quadratic function, and then finds the minimum of this approximation. It is known for its fast convergence, but can struggle with poor initial parameter estimates and may be sensitive to local minima. On the other hand, the ST method is a first-order optimization algorithm that iteratively adjusts the parameters in the direction of the steepest descent of the objective function. It is less sensitive to the initial parameter estimates, but may converge more slowly. The LM algorithm starts with an initial guess for the model's parameters and iteratively updates them. It calculates the gradient and the Hessian matrix of the objective function, which measures the discrepancy between the model and the data. These calculations help determine the direction and magnitude of the parameter updates. The algorithm also introduces a damping factor that controls the balance between the Gauss-Newton and steepest descent steps. This factor helps the algorithm handle different levels of curvature in the optimization problem, making it more robust. By iteratively adjusting the parameters and considering the curvature of the objective function, the LM algorithm converges towards the optimal parameter values that yield the best fit between the model and the data. Therefore, the LM algorithm is a powerful tool for finding the best-fit parameters in nonlinear curve fitting problems, providing accurate and reliable results [132].

7.4 Chirp-Rates Estimation Using Model Fitting Concept

We propose an algorithm for estimating the chirp rates of noisy multi-component LFM signal using model fitting concept. Without separating the individual components of the multi-component LFM signal, the multi-component version $\widetilde{\Omega}_K(\alpha;\widehat{\mathbf{m}})$ will be used as a model function in a nonlinear least squares LM algorithm to find the model which best fits. Let us suppose $\widetilde{s}_k(t)$, a K-component LFM signal. The FrFT will be computed at M rotation angle values. At each rotation angle, the maximum magnitude of the FrFT, $\max_u \{|\mathscr{F}^\alpha\{\widetilde{s}_k(t)\}(u)|^2\}$, will be taken to constitute one value into the collection $\widetilde{P}_K(\alpha)$. The LM least squares algorithm will be used to find the model function which best fit the collection $\widetilde{P}_K(\alpha)$, which is defined by the chirp rates. As the model being fit to the $\widetilde{P}_K(\alpha)$ is non-linear function, a non linear least squares approach should be adopted here to converge to the best fit model. Assuming that the number of the multi-components are known, the least squares estimates of $\widetilde{s}_k(t)$ chirp rates will be found by minimizing the sum of the weighted squares of the errors between the collection $\widetilde{P}_K(\alpha)$ and the model function $\widetilde{\Omega}_K(\alpha;\widehat{\mathbf{m}})$. That means to minimize the following cost function

$$\zeta(\widehat{\mathbf{m}}) = \sqrt{\sum_{\alpha}\left(\widetilde{P}_K(\alpha) - \widetilde{\Omega}_K(\alpha;\widehat{\mathbf{m}})\right)^2}. \tag{7.3}$$

Where, $\widehat{\mathbf{m}}$ is a vector contains the chirp rates of the individual components.

The LM algorithm begins with an initial parameter matrix, $\widehat{\mathbf{m}}_i = [m_1, m_2, ..., mk]$, and updates it iteratively to reduce $\zeta(\widehat{\mathbf{m}})$. However, before the algorithm can be executed, two crucial details must be determined. Firstly, the initial parameters, which in this case are the initial chirp rates, must be defined. This can be achieved by setting the initial chirp rates to the indices of the peaks within $\widetilde{P}_K(\alpha)$. Secondly, the length of the $\widetilde{P}_K(\alpha)$ collection, denoted by M, must be established. M can be determined by the α step between two adjacent rotation angles, $\Delta\alpha$. The determination of M is of paramount importance, as it influences both the computational cost and accuracy.

When M increases, there is an increase in both the number of FrFT computations and the computational cost. Conversely, if M decreases below a certain threshold, it will negatively impact the accuracy. This is because the model that best fits $\widetilde{P}_K(\alpha)$ will no longer be accurate, and there is a possibility that a component may go undetected. Thus, it is crucial to choose M in a manner that does not affect accuracy or increase computational cost.

To ensure accurate detection and modeling of the signal's dominant area in $\widetilde{P}_K(\alpha)$, the signal dominant area should contain at least two values: one before and one after

α_{opt}. Otherwise, the model obtained will not be accurate. Additionally, in the case of K component chirps, there will be K peaks. If the difference between the peaks of two consecutive components is greater than the width of the signal dominant area of one of these components, the components will overlap, and the resulting model will be inaccurate. This, in turn, will cause the loss of one of the components. Therefore, the width of the signal dominant area will be concluded in the following theorem.

Theorem 8. *The signal dominant area width in the maximum magnitude sweep of the FrFT domain can be approximated by*

$$L_w \approx \frac{2}{T^2} = \frac{2}{N^2 F_s^2}, \tag{7.4}$$

where F_s is the sampling frequency.

Proof. Since the noise effect is insignificant in comparison to the signal-dominant area, we can determine the width L_w in both the noiseless and noisy cases. In the absence of noise, the value of $P(\alpha)$ is nearly constant and significantly smaller than maximum of $P(\alpha)$ when α is far from α_{opt}. As mentioned before, the value of $P(\alpha)$ at α far from α_{opt} is

$$|S_{\alpha_{far}}(u_c)|^2 = |A|^2\gamma = \frac{A^2}{\sqrt{1+m^2}}. \tag{7.5}$$

Therefore, we can write

$$\frac{|S_{\alpha_{opt}}(u_{opt})|^2}{|S_{\alpha_{far}}(u_c)|^2} = T^2(1+m^2) \gg 1. \tag{7.6}$$

Which means that the difference between the values in noisy area and the maximum value of $P(\alpha)$ is very big and of order T^2. Therefore, it is an acceptable assumption to say that

$$L = \frac{|S_{\alpha_{opt}}(u_{opt})|^2}{L_N}. \tag{7.7}$$

$$P(\alpha_i) > L \Rightarrow \alpha_i \in \textbf{the signal dominant region.} \tag{7.8}$$

Where L_N is an integer bigger than one, and L is a defined threshold in $P(\alpha)$ between the two regions the signal dominant and noise dominant regions. The width L_w can be defined by the junction between L and $P(\alpha)$, therefore it can be defined by the difference in $P(\alpha)$ between these two values of α

$$L_w = \alpha_r - \alpha_l. \tag{7.9}$$

Where

$$\alpha_r = \alpha_{opt} + \Delta\alpha, \alpha_l = \alpha_{opt} - \Delta\alpha. \tag{7.10}$$

Therefore we can write that

$$L_w = 2 \times \Delta\alpha. \tag{7.11}$$

Using the equation above, $\Delta\alpha$ can be calculated. Using the model $\Omega(\alpha; m)$, $P(\alpha_r)$ is

$$\Omega(\alpha_r; m) \approx \left|S_{\alpha_r}(u_c)\right|^2 = \frac{A^2 \csc\alpha_r}{\cot\alpha_r + m} \frac{\cosh(z) - \cos(z)}{\cosh(z) + \cos(z)}. \tag{7.12}$$

Where

$$z = T\sqrt{2(m + \cot\alpha_r)}. \tag{7.13}$$

As previously mentioned, the noise-dominant area in the noiseless case remains almost constant when α is far from α_{opt}. In Chapter 5, when discussing the properties of the noise-dominant area, it was noted that the term

$$\frac{\cosh(z) - \cos(z)}{\cosh(z) + \cos(z)} = 1. \tag{7.14}$$

holds for values of α in the noise-dominant area. Building upon this idea, we can infer that the signal dominant area commences when the aforementioned term starts to decrease below 1. Then the transition from noise-dominant area to signal-dominant area begins when the above term has a value close to 1, as

$$\frac{\cosh(z) - \cos(z)}{\cosh(z) + \cos(z)} = 0.98. \tag{7.15}$$

Solving the above equation yields the value

$$z = 1.54601. \tag{7.16}$$

To compute $\Delta\alpha$ we can use the following

$$\cot\alpha_r = \cot(\alpha_{opt} + \Delta\alpha). \tag{7.17}$$

Using

$$\cot(a + b) = \frac{\cot a \cot b - 1}{\cot b + \cot a}. \tag{7.18}$$

The value of $\cot\alpha_r$ is

$$\cot\alpha_r = \frac{-m\cot\Delta\alpha - 1}{\cot\Delta\alpha - m}, \tag{7.19}$$

and for small $\Delta\alpha$

$$\cot\alpha_r \approx \frac{m + \Delta\alpha}{m\Delta\alpha - 1}. \tag{7.20}$$

Using the above result in (7.16) and (7.13)

$$\Delta\alpha = \frac{1.1951}{T^2 \times m^2 + T^2 - 1.1951 \times m}. \tag{7.21}$$

For large values of T, we can approximate the expression as:

$$\frac{1.1951}{T^2 \times m^2 + T^2 - 1.1951 \times m} \approx \frac{1.1951}{T^2 \times m^2 + T^2} = \frac{1.1951}{T^2} \cdot \frac{1}{m^2 + 1}.$$

For small values of m, we can further approximate the expression as:

$$\frac{1.1951}{T^2} \cdot \frac{1}{m^2 + 1} \approx \frac{1.1951}{T^2} \cdot 1 = \frac{1.1951}{T^2}.$$

Therefore, the approximation for large T and small m is:

$$\Delta\alpha = \frac{1.1951}{T^2 \times m^2 + T^2 - 1.1951 \times m} \approx \frac{1}{T^2}.$$

As the width in α domain of the signal dominant area equals $2\Delta\alpha$ Consequently, the proof is concluded. ■

When dividing the search region of α with $\Delta\alpha$ step to form $\widetilde{P}_K(\alpha)$, that will ensure that any two adjacent components are resolved. The equation above tells us how small $\Delta\alpha$ should be to achieve this. As previously mentioned, $P(\alpha)$ has two areas: the signal dominant area and the noisy area. To accurately detect and model the signal dominant area, $\widetilde{P}_K(\alpha)$ should contain at least two values in the signal dominant area, one before α_{opt} and one after α_{opt}. Otherwise, the concluded $\Omega(\alpha; m)$ model will not be accurate. In the case of multi-component chirp signals, there may be more than one peak near each other. If the difference between the peaks of two consecutive components is greater than the width of the signal dominant area of one of these components, the components will overlap and the concluded model will not be accurate, causing the loss of one of the components. Therefore, the optimal value of α step is $\Delta\alpha$, which provides enough resolution to follow up the correct model of $\widetilde{P}_K(\alpha)$ and guarantees the presence of at least two rotation angles inside the signal dominant area. It is worth mentioning that the result obtained now is consistent with the case discussed in chapter 6, where the accuracy in both the α and m domains was chosen to be 1/N.

Now the algorithm is ready to go, a noisy K-component LFM signal is received. The $\widetilde{P}_K(\alpha)$ collection is formed by taking the maximum of the squared maximum magnitude of FrFT of the signal at the following range $[\pi/4 : \alpha_s : 3\pi/4]$, the initial chirp rates are chosen by taking the indexes of the peaks into $\widetilde{P}_K(\alpha)$. Then the LM algorithm iterates using $\widetilde{\Omega}_K(\alpha; \mathbf{m})$ as model function till finding the model which best

fits $\widetilde{P}_K(\alpha)$. The output result is $\widehat{\mathbf{m}} = [\widehat{m}_1, \widehat{m}_2, ..., \widehat{m}_k]$, the estimated chirp rates. It is clear from this process that the proposed algorithm has solved the following problems.

- The propagation of error which introduced in the other chirp rate estimation algorithms for multi-component LFM signals. These algorithms estimate the chirp rate of the first component, remove it then repeat this estimating process till the last component. Because of this process the error propagation will be introduced. In our proposed algorithm the chirp rate estimation is happening one time for all the components, therefore, there will not be error propagation.
- The picket fence effect because of the discretization of u. Because of the model fitting concept and terminology adopted, the picket fence effect has been solved.
- High level of accuracy needs very big computational load. Because the chirp rate estimation is happening one time, the computational cost is low compared with the other algorithms.

7.5 Computational Cost

The computational complexity depends on the total number of FrFT operations, I, needed to estimate the chirp rates of m component chirp signal. The number of FrFT operations, I is

$$I = \frac{3\pi/4 - \pi/4}{\Delta\alpha} = N. \tag{7.22}$$

The total computational cost of the proposed algorithm is

$$\text{Computational Cost} = I\mathcal{O}(N \log N). \tag{7.23}$$

Where $\mathcal{O}(N \log N)$ is the computational cost of a single FrFT . (7.23) can be rewritten

$$\text{Computational Cost} = \mathcal{O}(N^2 \log N). \tag{7.24}$$

Where $I = \mathcal{O}(N)$.

7.6 Simulations

To evaluate the performance of the proposed algorithm, we validated the theoretical results and demonstrated the accuracy of the estimator through Monte Carlo simulations. Specifically, 2000 simulations were conducted for each SNR value in the range of $[-16dB, 8dB]$ to estimate the chirp rates of a four-component LFM signal. We studied two cases:

In the first case, the chirp rates were chosen to be two close chirp rates and two chirp rates symmetric to the other two. The parameters were set to $A_1, f_1, m_1 = 1, 0, -0.08$, $A_2, f_2, m_2 = 1, 0, -0.04$, $A_3, f_3, m_3 = 1, 0, 0.04$, and $A_4, f_4, m_4 = 1, 0, 0.08$.

In the second case, the chirp rates were chosen to be far from each other and distributed from small values to large values. The parameters were set to $A_1, f_1, m_1 = 1, 0, 0.1$, $A_2, f_2, m_2 = 1, 0, 0.2$, $A_3, f_3, m_3 = 1, 0, 0.3$, and $A_4, f_4, m_4 = 1, 0, 0.4$.

To quantify the accuracy of the estimator, we computed the mean-square error (MSE) or estimation error variance, defined as:

$$MSE = \frac{1}{C}\sum_{i=1}^{C}(\widehat{m}^{(i)} - m)^2, \tag{7.25}$$

where $\widehat{m}^{(i)}$ is the estimated chirp-rate for the $i-th$ iteration of the Monte Carlo simulation and m is the actual value of the chirp-rate, for each value of the SNR. Fig. 7.4 shows the simulation results of the proposed algorithm's performance, where the calculated MSE is plotted against the SNR along with the CRLB. Based on the figures, the following conclusions can be made.

In the first case, at low SNR levels, the noise is dominant as its power is greater than the value of $P(\alpha)$ at α_{opt}. Therefore, the simulation results at low SNR values less than $-12dB$ do not agree with the CRLB, and the algorithm fails to fit to the correct model. This highlights the importance of the following condition:

$$E\left[\widetilde{P}(\alpha)\right] = P(\alpha) \times \left(1 + \frac{1}{SNR \times T}\right). \tag{7.26}$$

and see that as this condition is not valid, the model can not give accurate results and therefore the simulation results is far from CRLB. Then, as the noise level decreases, the results start to approach the CRLB, and the peak at α_{opt} in $P(\alpha)$ becomes more distinct from the noise. Therefore, there exists an SNR threshold between these two cases. Although the chirp rates are close, the algorithm manages to detect and estimate the chirp rates of the four components correctly. The components with symmetric chirp rates, $0.04, -0.04$ and $0.08, -0.08$, exhibit similar performance. Two components match the CRLB, while for the other two, the performance approaches the CRLB as close as $-10dB$, after which the increasing rate decreases, and the performance stops matching the CRLB. This is because of the bias effect, where the mutual influence between the components causes a shift in the amplitude and index of the maximum value.

In the second case, in addition to the aforementioned observations, the bias effect is

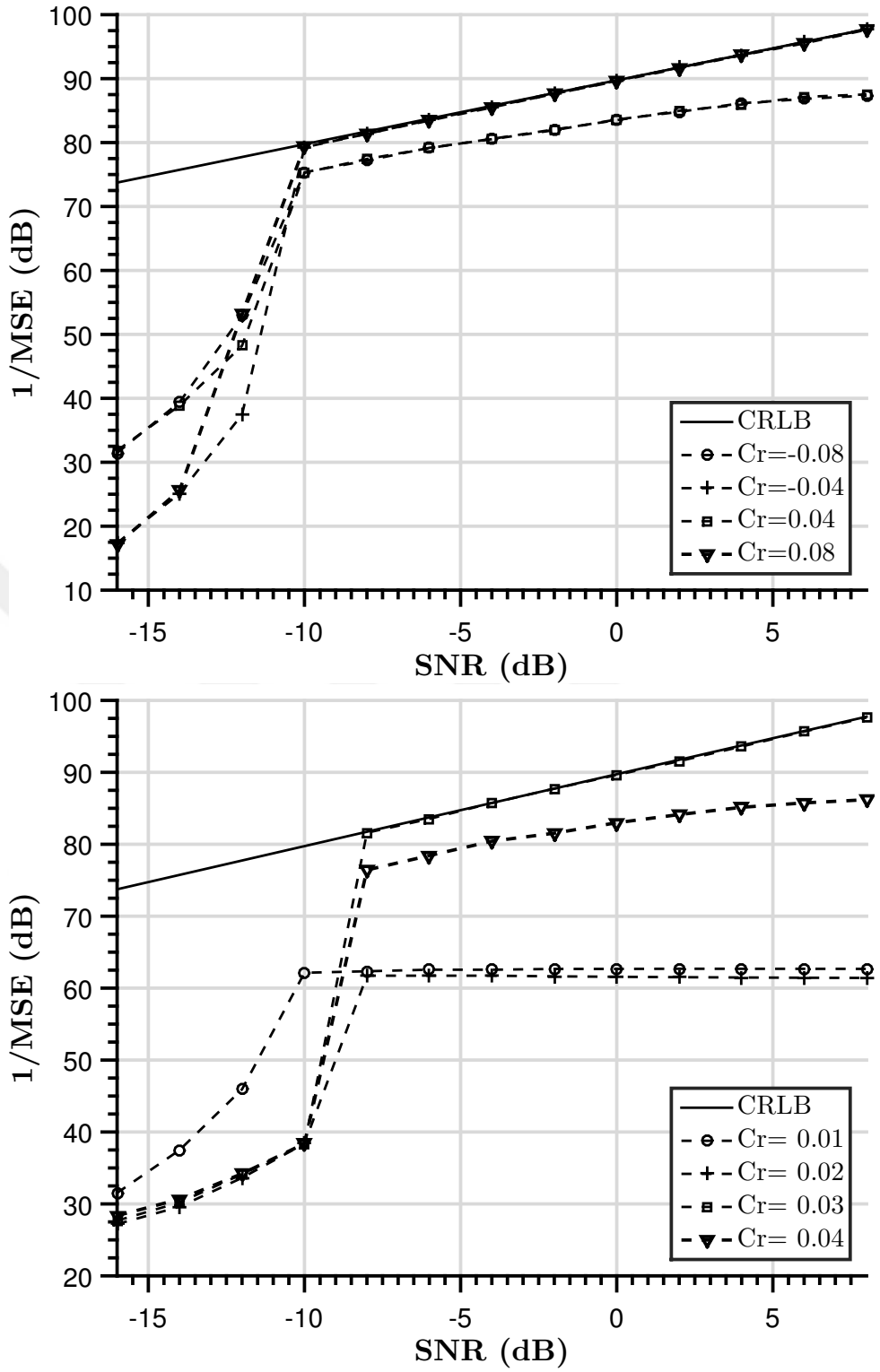

Figure 7.4 Multi-Component Chirp Rate Estimation Performance.

more pronounced, especially for small chirp rate values. To cope with this problem, a two-phase estimation algorithm can be adopted.

- In the first phase, the proposed LM based algorithm will be used in coarse phase estimation to estimate the chirp rates of the multi-component signal.
- In the second phase, the proposed algorithm is used to estimate the chirp rates, initial frequencies, and amplitudes of each component. Then, a dechirping process is applied to eliminate all but one component. The remaining component is used as input for a fast algorithm, such as the GSS algorithm, to obtain a fine estimation of its chirp rate.
- The previous step will be repeated for all the other components.
- The accuracy needed in the GSS algorithm will be $N^{-}3$. However, the range which the GSS will search in will be small,$1/N$, therefore the number of iterations would be very small.

The proposed algorithm is presented in Algorithm (4). The LM algorithm takes the noisy multi-component LFM signal, the collection $\widetilde{P}_K(\alpha)$, and the model $\widetilde{\Omega}_K(\alpha;\widehat{\mathbf{m}})$ as input to find the best fit. The AME estimator, which is a sinusoidal estimation algorithm, is used to estimate the frequency of a sinusoidal signal. The GSS algorithm takes the isolated component and its coarse estimation of the chirp rate as input. Using the coarse estimation of the chirp rate as input reduces the iteration number of the GSS algorithm since the range will be limited to $1/N$. Lastly, when the peak at

Algorithm 4 The proposed algorithm for estimating the chirp rates of a multi-component chirp signal.

Initialize:
$\widetilde{P}_K(\alpha) \leftarrow \max\left\{\left|\mathscr{F}^{\alpha}\left\{\widetilde{s_k}(t)\right\}(u)\right|^2\right\}$,
$\widehat{\mathbf{m}}_i \leftarrow \max\left\{\widetilde{P}_K(\alpha)\right\}$ *%The first k maxima*,
$\widehat{\mathbf{m}} \leftarrow LM[\widetilde{P}_K(\alpha)]$,
for $i = 1$ to K **do**
  $\widehat{f_i} \leftarrow \text{AME}[e^{-j\pi\left(\widetilde{m}_i t^2\right)} \times \widetilde{s_k}(t)]$
end for
for $i = 1$ to K **do**
  $\widetilde{y_i}(t) \leftarrow \widetilde{s_k}(t) - \sum_{n=1}^{k-1} e^{-j\pi\left(\widetilde{m}_n t^2 + 2\widehat{f}_n t\right)}$ *% :* $i \neq n$,
  $\widehat{m}_i \leftarrow GSS[\widetilde{y_i}(t), \widehat{m}_i]$,
end for
return $\widehat{m} = [\widehat{m}_1, \widehat{m}_2, \cdots, \widehat{m}_K]^T$

α_{opt} becomes dominant compared to the noise, the simulation results match with the CRLB accurately, where we can see the efficiency of the algorithm in separating the

components, estimating the chirp rate precisely and the ability to operate under noise without cross term effect.

7.7 Results and Discussion

This chapter proposes a nonlinear least squares algorithm based on the LM method to estimate the chirp rates of multi-component chirp signals. The optimal α step was determined to ensure the accurate modeling of $\widetilde{P}_K(\alpha)$ and to ensure the detection and estimation of all nearby components. By using the optimal step size, the proposed algorithm was able to accurately estimate the chirp rates of multi-component chirp signals, even under high levels of noise. Additionally, the LM curve fitting concept was adopted, and the concluded model $\widetilde{\Omega}_K(\alpha; \mathbf{m})$ was used as the model function to which the data was best fit. This algorithm can effectively solve the picket fence effect and can work under high levels of noise with an acceptable computational cost. Furthermore, as the estimation of the multi-components occurs only once, this algorithm avoids the propagation of error problem, which can be introduced in other chirp rate estimation algorithms that adopt a removal and estimating technique.

The simulations show that the proposed model and estimation algorithm can efficiently solve the chirp rate estimation problem.

8
Conclusion And Future Work

Throughout this thesis, it has been demonstrated that the FrFT is not only the most appropriate, but also the optimal tool for estimating chirp parameters. By transforming the chirp signal into an intermediate domain between time and frequency, the FrFT allows for simultaneous analysis of both time and frequency characteristics of the signal. Moreover, the FrFT exhibits a unique property that makes it particularly well-suited for analyzing chirp signals. Specifically, the FrFT of a chirp signal is also a chirp signal with a chirp rate proportional to the transform order. As a result, the FrFT can directly estimate the chirp rate of a signal, eliminating the need for additional processing steps.

The FrFT has been shown to strike an optimal balance between time and frequency resolution, making it the preferred choice for analyzing chirp signals. Compared to other transforms, the FrFT offers several advantages, including more accurate representation of chirp signals in the presence of noise, due to its ability to tune to the chirp rate of the signal and achieve higher resolution in the time-frequency domain. Furthermore, the FrFT can isolate and analyze individual components of a multi-component signal, which is critical for accurately estimating chirp parameters in such signals.

Based on the aforementioned considerations, we have chosen to utilize the FrFT as a fundamental tool for constructing chirp parameter estimation algorithms. Extensive research has demonstrated that our algorithms exhibit superior performance characteristics when compared to existing methods.

For future work, it can be mentioned that the combination of compressed sensing (CS) and FrFT has the potential to provide an advanced algorithm.

As it has been mentioned in Chapter 1, CS is a mathematical technique that allows for the efficient recovery of a signal from a small number of linear measurements or samples. The technique is particularly useful when the signal of interest has a sparse

or compressible representation in some known basis or dictionary.

In traditional signal processing, signals are often sampled uniformly at a high rate, which can result in large amounts of data that are expensive to acquire, store, and process. CS addresses this challenge by acquiring only a small number of measurements that capture the essential features of the signal, allowing for significant reductions in the amount of data that must be collected and processed.

The key idea behind CS is that a signal can be represented sparsely in a certain basis, meaning that most of the coefficients in the basis representation are zero or very small. For example, a signal consisting of a few frequencies might have a sparse representation in the Fourier basis. CS exploits this sparsity to recover the signal from a small number of linear measurements.

To do this, CS typically involves solving an optimization problem that seeks to find the sparsest or most compressible representation of the signal that is consistent with the measured data. The optimization problem is often formulated as a convex program that can be efficiently solved using a variety of numerical methods, including greedy algorithms and convex optimization solvers.

CS has applications in a wide range of fields, including signal processing, image processing, and machine learning. It has been used for tasks such as image and video compression, magnetic resonance imaging, and sparse signal recovery in high-dimensional data analysis.

By leveraging the FrFT with CS techniques, it is possible to obtain even more accurate and efficient estimates of the chirp parameters, which can have important applications in various fields such as radar, sonar, and biomedical signal processing.

CS can be used with the FrFT in the estimation of chirp parameters by exploiting the sparsity of signals in certain domains, such as the FrFT domain.

In the context of chirp parameter estimation, the FrFT can be used to transform the signal into a domain where it is sparse or compressible. The advantage of the FrFT is its sparsity-promoting property, which makes it well-suited for CS-based algorithms. The FrFT can provide a sparse representation of the signal, which can be used to reduce the number of samples needed for accurate chirp parameter estimation, leading to faster and more efficient algorithms.

Once the signal has been transformed into the FrFT domain, CS techniques can be used to estimate the chirp parameters from a subset of the coefficients. This involves solving an optimization problem that seeks to minimize the ℓ_1 norm of the coefficients

subject to the constraint that the signal reconstructed from those coefficients matches the observed data.

One approach to solving this optimization problem is through iterative algorithms such as the basis pursuit denoising algorithm or the iterative hard thresholding algorithm. These algorithms iteratively estimate the sparse coefficients until a certain convergence criterion is met.

Overall, by combining the FrFT and CS techniques, it is possible to accurately estimate the chirp parameters from a small number of measurements, making it a promising approach for applications where data acquisition is limited or expensive.

A general method for using the FrFT and CS in chirp parameter estimation:

- Acquire a set of measurements of a chirp signal corrupted by noise.
- Perform the FrFT on each measurement with different fractional orders.
- Apply CS techniques to recover sparse representations of the transformed signals.
- Extract the chirp parameters (frequency, chirp rate, initial phase) from the recovered sparse representations using appropriate algorithms.
- Combine the extracted chirp parameters from all measurements to improve the accuracy of the estimates.
- Evaluate the performance of the proposed method using simulation studies and real data experiments.

The use of CS allows us to acquire fewer measurements than what is typically required by Nyquist sampling theorem, while the FrFT can provide more information about the chirp signal and potentially improve the sparsity of the signal representation. The combination of these two techniques can lead to a more efficient and accurate chirp parameter estimation method.

REFERENCES

[1] H. L. Van Trees, K. L. Bell, Z. Tian, *Detection, Estimation, and Modulation Theory Part I: Detection, Estimation and Filtering Theory*, 2nd. Wiley, 2013.

[2] L. L. Scharf, *Statistical Signal Processing: Detection, Estimation and Time Series Analysis*. Prentice Hall, 1991.

[3] S. Kay, *Fundamentals of Statistical Signal Processing, Volume II: Detection Theory*. Prentice Hall, 1998.

[4] H. V. Poor, *An Introduction to Signal Detection and Estimation*, 2nd. Springer, 1998.

[5] T. J. Abatzoglou, "Fast maximum likelihood joint estimation of frequency and frequency rate," *IEEE Transactions on Aerospace and Electronic Systems*, vol. AES-22, no. 6, pp. 708–715, 1986.

[6] S. Peleg, B. Porat, "Linear FM signal parameter estimation from discrete-time observations," *IEEE Transactions on Aerospace and Electronic Systems*, vol. 27, no. 4, pp. 607–616, 1991.

[7] S. Golden, B. Friedlander, "Maximum likelihood estimation, analysis, and applications of exponential polynomial signals," *IEEE Transactions on Signal Processing*, vol. 47, no. 6, pp. 1493–1501, 1999.

[8] S. Saha, S. Kay, "Maximum likelihood parameter estimation of superimposed chirps using Monte Carlo importance sampling," *IEEE Transactions on Signal Processing*, vol. 50, no. 2, pp. 224–230, 2002.

[9] Y. Li, H. Fu, P. Y. Kam, "Improved, approximate, time-domain ML estimators of chirp signal parameters and their performance analysis," *IEEE Transactions on Signal Processing*, vol. 57, no. 4, pp. 1260–1272, 2009.

[10] Z. Deng, L.-m. Ye, M.-z. Fu, S.-j. Lin, Y.-x. Zhang, "Further investigation on time-domain maximum likelihood estimation of chirp signal parameters," *Signal Processing, IET*, vol. 7, pp. 444–449, Jul. 2013.

[11] R. Liang, K. Arun, "Parameter estimation for superimposed chirp signals," in *[Proceedings] ICASSP-92: 1992 IEEE International Conference on Acoustics, Speech, and Signal Processing*, vol. 5, 1992, 273–276 vol.5.

[12] J. Angeby, M. Viberg, T. Gustafsson, "Non-linear instantaneous least squares and its high SNR analysis," in *IEEE Intern. Conf. on Acoustics, Speech, and Signal Proc. (ICASSP)*, vol. 3, Phoenix, USA, Mar. 1999, pp. 1277–1280.

[13] J. Angeby, "Estimating parameters using the nonlinear instantaneous least squares approach," *IEEE Transactions on Signal Processing*, vol. 48, no. 10, pp. 2721–2731, Oct. 2000.

[14] L. Zhou, J. Yang, B. Tang, N. Li, "Signal reconstructing least-squares algorithm for chirp signal parameters estimation," in *2006 8th international Conference on Signal Processing*, vol. 4, 2006.

[15] Y. Doweck, A. Amar, I. Cohen, "Parameter estimation of harmonic linear chirps," in *2015 23rd European Signal Processing Conference (EUSIPCO)*, 2015, pp. 1476–1480.

[16] D. S. Pham, A. M. Zoubir, "Analysis of multicomponent polynomial phase signals," *IEEE Transactions on Signal Processing*, vol. 55, no. 1, pp. 56–65, 2007.

[17] E. Moradi, R. Mohseni, "Parameters estimation of linear frequency modulated signal using Kalman filter and its extended versions," *Signal Image Video Process.*, vol. 17, 2022. DOI: 10.1007/s11760-022-02260-w.

[18] R. A. Altes, "Detection, estimation, and classification with spectrograms," *Journal of the Acoustical Society of America*, vol. 67, no. 4, pp. 1232–1246, Apr. 1980.

[19] X. Li, G. Bi, S. Stankovic, A. M. Zoubir, "Local polynomial Fourier transform: A review on recent developments and applications," *Signal Processing*, vol. 91, no. 6, pp. 1370–1393, Jun. 2011.

[20] D. Fourer, F. Auger, K. Czarnecki, S. Meignen, P. Flandrin, "Chirp rate and instantaneous frequency estimation: Application to recursive vertical synchrosqueezing," *IEEE Signal Processing Letters*, vol. 24, no. 11, pp. 1724–1728, 2017.

[21] J. Wang, S. Su, Z. Chen, "Parameter estimation of chirp signal under low SNR," *Science China Information Sciences*, vol. 58, pp. 1–13, 2015.

[22] G. Boudreaux-Bartels, T. Parks, "Time-varying filtering and signal estimation using Wigner distribution synthesis techniques," *IEEE Transactions on Acoustics, Speech, and Signal Processing*, vol. 34, no. 3, pp. 442–451, Jun. 1986.

[23] S. Barbarossa, A. Farina, "Detection and imaging of moving objects with synthetic aperture radar. 2. joint time-frequency analysis by Wigner-Ville distribution," *IEE Proceedings F (Radar and Signal Processing)*, vol. 139, no. 1, pp. 89–97, Feb. 1992.

[24] B. Boashash, P. O'Shea, "Polynomial Wigner-Ville distributions and their relationship to time-varying higher order spectra," *IEEE Transactions on Signal Processing*, vol. 42, no. 1, pp. 216–220, Jan. 1994.

[25] F. G. Geroleo, M. Brandt-Pearce, "Detection and estimation of LFMCW radar signals," *IEEE Transactions on Aerospace and Electronic Systems*, vol. 48, no. 1, pp. 405–418, Jan. 2012.

[26] F. Sattar, G. Salomonsson, "The use of a filter bank and the Wigner-Ville distribution for time-frequency representation," *IEEE Transactions on Signal Processing*, vol. 47, no. 6, pp. 1776–1783, 1999.

[27] B. Boashash, *Time-Frequency Signal Analysis and Processing: A Comprehensive Reference*, 2nd ed. New York: Academic Press, 2015.

[28] M. Kirscht, "Detection and imaging of arbitrarily moving targets with single-channel SAR," in *RADAR 2002*, 2002, pp. 280–285.

[29] L. Cohen, “Time-frequency distributions- A review,” *Proceedings of the IEEE*, vol. 77, no. 7, pp. 941–981, Jul. 1989.

[30] L. Stankovic, “Highly concentrated time–frequency distributions: Pseudo quantum signal representation,” *IEEE Transactions on Signal Processing*, vol. 45, no. 3, pp. 543–551, Mar. 1997.

[31] S. Peleg, B. Friedlander, “The discrete polynomial-phase transform,” *IEEE Transactions on Signal Processing*, vol. 43, no. 8, pp. 1901–1914, 1995.

[32] S. Peleg, B. Friedlander, “Multicomponent signal analysis using the polynomial-phase transform,” *IEEE Transactions on Aerospace and Electronic Systems*, vol. 32, no. 1, pp. 378–387, 1996.

[33] S. Barbarossa, A. Scaglione, G. Giannakis, “Product high-order ambiguity function for multicomponent polynomial-phase signal modeling,” *IEEE Transactions on Signal Processing*, vol. 46, no. 3, pp. 691–708, 1998.

[34] S. Barbarossa, “Parameter estimation of multicomponent polynomial-phase signals by intersection of signal subspaces,” in *Proc. 8th Stat. Signal Processing Workshop*, 1996, pp. 452–455.

[35] Y. Wang, A. C. Abdelkader, B. Zhao, J. Wang, “ISAR imaging of maneuvering targets based on the modified discrete polynomial-phase transform,” *Sensors*, vol. 15, no. 9, pp. 22 401–22 418, 2015.

[36] G. Bai, Y. Cheng, W. Tang, S. Li, “Chirp rate estimation for LFM signal by multiple DPT and weighted combination,” *IEEE Signal Processing Letters*, vol. 26, no. 1, pp. 149–153, 2019.

[37] N. Rabiee, H. Azad, N. Parhizgar, “Enhancement DPT method in terms of estimation chirp rate and central frequency parameters of the LFM signal,” *Radioengineering*, vol. 27, pp. 230–237, 2019.

[38] N. Rabiee, H. Azad, N. Parhizgar, “Promotion of improved discrete polynomial-phase transform method for phase parameters estimation of linear frequency modulation signal,” *Journal of Communications Technology and Electronics*, vol. 64, pp. 1266–1275, Nov. 2019.

[39] T. Gu, G. Liao, Y. Li, Y. Guo, Y. Huang, “Parameter estimate of multi-component LFM signals based on GAPCK,” *Digit. Signal Process.*, vol. 100, p. 102 683, 2020. DOI: 10.1016/j.dsp.2020.102683.

[40] A. Y. Erdogan, T. O. Gulum, L. Durak-Ata, T. Yildirim, P. E. Pace, “FMCW signal detection and parameter extraction by cross Wigner–Hough transform,” *IEEE Transactions on Aerospace and Electronic Systems*, vol. 53, no. 1, pp. 334–344, 2017.

[41] T. O. Gulum, A. Y. Erdogan, L. Durak-Ata, T. Yildirim, P. E. Pace, “Enhanced LPI waveform representation by ambiguity-domain elliptical Gaussian filtering,” *IEEE Transactions on Aerospace and Electronic Systems*, vol. 53, no. 2, pp. 762–777, 2017.

[42] A. Bouchikhi, A.-O. Boudraa, J.-C. Cexus, T. Chonavel, “Analysis of multicomponent LFM signals by Teager Huang-Hough transform,” *IEEE Transactions on Aerospace and Electronic Systems*, vol. 50, no. 2, pp. 1222–1233, 2014.

[43] C. Wenwu, C. Rushan, "Multi-component LFM signal detection and parameter estimation based on Radon-HHT," *Journal of Systems Engineering and Electronics*, vol. 19, pp. 1097–1101, Dec. 2008.

[44] X. Lv, M. Xing, S. Zhang, Z. Bao, "Keystone transformation of the Wigner-Ville distribution for analysis of multicomponent LFM signals," *Signal Processing*, vol. 89, no. 5, pp. 791–806, May 2009.

[45] V. K. Nguyen, "A low complexity parameter estimation technique for LFMCW signals," *IEEE Transactions on Aerospace and Electronic Systems*, vol. 50, no. 4, pp. 2554–2563, 2014.

[46] S. Barbarossa, "Analysis of multicomponent LFM signals by a combined Wigner-Hough transform," *IEEE Transactions on Signal Processing*, vol. 43, no. 6, pp. 1511–1515, 1995.

[47] A. Lohmann, B. Soffer, "Relationships between the Radon–Wigner and fractional Fourier transforms," *Journal of the Optical Society of America*, vol. 11, no. 6, pp. 1798–1801, 1994.

[48] J. Wood, D. Barry, "Radon transformation of time-frequency distributions for analysis of multicomponent signals," *IEEE Transactions on Signal Processing*, vol. 42, no. 11, pp. 3166–3177, 1994.

[49] M. Wang, A. Chan, C. Chui, "Linear frequency-modulated signal detection using Radon-ambiguity transform," *IEEE Transactions on Signal Processing*, vol. 46, no. 3, pp. 571–586, 1998.

[50] G. Bi, X. Li, C. See, "LFM signal detection using LPP-Hough transform," *Signal Processing*, vol. 91, no. 6, pp. 1432–1443, Jun. 2011.

[51] P. O'Shea, "A fast algorithm for estimating the parameters of a quadratic FM signal," *IEEE Transactions on Signal Processing*, vol. 52, no. 2, pp. 385–393, 2004.

[52] L. Zuo, M. Li, Z. Liu, L. Ma, "A high-resolution time-frequency rate representation and the cross-term suppression," *IEEE Transactions on Signal Processing*, vol. 64, no. 10, pp. 2463–2474, 2016.

[53] P. Wang, H. Li, I. Djurović, B. Himed, "Integrated cubic phase function for linear FM signal analysis," *IEEE Transactions on Aerospace and Electronic Systems*, vol. 46, no. 3, pp. 963–977, 2010.

[54] P. Wang, J. Yang, "Multicomponent chirp signals analysis using product cubic phase function," *Digital Signal Processing*, vol. 16, no. 6, pp. 654–669, 2006.

[55] J. Su, H.-h. Tao, X. Rao, J. Xie, X.-l. Guo, "Coherently integrated cubic phase function for multiple LFM signals analysis," *Electronics Letters*, vol. 51, pp. 411–413, 2015.

[56] W. Yu, W. Su, H. Gu, "Fast method for radar maneuvering target detection and motion parameter estimation," *Multidimens. Syst. Signal Processing*, vol. 29, 2018.

[57] Y. Zhao, S. Han, J. Yang, L. Zhang, H. Xu, J. Wang, "A novel approach of slope detection combined with Lv's distribution for airborne SAR imagery of fast moving targets," *Remote Sensing*, vol. 10, no. 5, 2018.

[58] X. Lv, G. Bi, C. Wan, M. Xing, "Lv's distribution: Principle, implementation, properties, and performance," *IEEE Transactions on Signal Processing*, vol. 59, no. 8, pp. 3576–3591, 2011.

[59] Y. Wang, K. Wang, F. Jing, X. Lan, Y. Zou, L. Wan, "LFM signal analysis based on improved Lv distribution," *IEEE Access*, vol. 7, pp. 169 038–169 046, 2019.

[60] J. Zheng, H. Liu, Q. H. Liu, "Parameterized centroid frequency-chirp rate distribution for LFM signal analysis and mechanisms of constant delay introduction," *IEEE Transactions on Signal Processing*, vol. 65, no. 24, pp. 6435–6447, 2017.

[61] C. Wang-zong, "DOA estimation of LFM signals based on compressed sensing," *Application Research of Computers*, 2009.

[62] B. Liu, P. Fu, C. Xu, J. Gai, "Parameter estimation of LFM signal with compressive measurements," *Journal of Convergence Information Technology*, vol. 6, pp. 303–310, Mar. 2011.

[63] K. Wang, W. Ye, G. Lao, Y. Wang, "Fast algorithm on parameter estimation of wideband LFM signal based on down-chirp and CS," in *2014 IEEE International Conference on Signal Processing, Communications and Computing (ICSPCC)*, 2014, pp. 133–136.

[64] H. Yan, C. Dong, G. Zhao, "Parameter estimation of LFM signal based on compressed sensing," *Dianbo Kexue Xuebao/Chinese Journal of Radio Science*, vol. 30, pp. 449–456, Jun. 2015.

[65] J. Guo, H. Zou, X. Yang, G. Liu, "Parameter estimation of multicomponent chirp signals via sparse representation," *IEEE Transactions on Aerospace and Electronic Systems*, vol. 47, no. 3, pp. 2261–2268, Jul. 2011.

[66] G. Lopez-Risueno, J. Grajal, "Multiple signal detection and estimation using atomic decomposition and EM," *IEEE Transactions on Aerospace and Electronic Systems*, vol. 42, no. 1, pp. 84–102, Jan. 2006.

[67] P. Yang, L. Zheng, W.-L. Jiang, "Parameter estimation of multi-component chirp signals based on discrete chirp Fourier transform and population monte carlo," *Signal, Image and Video Processing*, vol. 9, Jul. 2013.

[68] Y. Meyer, *Oscillating Patterns in Image Processing and Nonlinear Evolution Equations* (The fifteenth Dean Jacqueline B. Lewis memorial lectures). American Mathematical Society (AMS), 2001.

[69] M. Skolnik, *Introduction to Radar Systems*. New York: McGraw-Hill, 1962.

[70] P. E. Pace, *Detecting and classifying low probability of intercept radar*. Artech House, 2009.

[71] M. Richards, *Fundamentals of radar signal processing*. 2nd Ed. McGraw-Hill Education, 2014.

[72] E. Buer, "Characterization of modulated chirp signals," M.S. thesis, Norwegian University of Science and Technology, 2020.

[73] M. Vespe, G. Jones, C. J. Baker, "Lessons for radar," *IEEE Signal Processing Magazine*, vol. 26, no. 1, pp. 65–75, 2009.

[74] Y. Kopsinis, E. Aboutanios, D. A. Waters, S. McLaughlin, "Time-frequency and advanced frequency estimation techniques for the investigation of bat echolocation calls," *The Journal of the Acoustical Society of America*, vol. 127, no. 2, pp. 1124–1134, Feb. 2010.

[75] M. Bozek-Juzmicki, D. Colella, G. Jacyna, "Feature-based epileptic seizure detection and prediction from ecog recordings," in *Proceedings of IEEE-SP International Symposium on Time- Frequency and Time-Scale Analysis*, 1994, pp. 564–567.

[76] D. Devedeux, J. Duchene, "Comparison of various time/frequency distributions (classical and signal-dependent) applied to synthetic uterine EMG signals," in *Proceedings of IEEE-SP International Symposium on Time-Frequency and Time-Scale Analysis*, 1994, pp. 572–575.

[77] M. Bennett, S. McLauglin, T. Anderson, N. McDicken, "Filtering of chirped ultrasound echo signals with the fractional Fourier transform," in *IEEE Ultrasonics Symposium, 2004*, vol. 3, 2004, 2036–2040 Vol.3.

[78] A. G. Stove, "Linear FMCW radar techniques," *IEE Proceedings F (Radar and Signal Processing)*, vol. 139, no. 5, pp. 343–350, Oct. 1992.

[79] P. R. Atkins, T. Collins, K. G. Foote, "Transmit-signal design and processing strategies for sonar target phase measurement," *IEEE Journal of Selected Topics in Signal Processing*, vol. 1, no. 1, pp. 91–104, Jun. 2007.

[80] J. Munoz-Ferreras, F. Perez-Martinez, M. Burgos-Garcia, "Helicopter classification with a high resolution LFMCW radar," *IEEE Transactions on Aerospace and Electronic Systems*, vol. 45, no. 4, pp. 1373–1384, Oct. 2009.

[81] T. Misaridis, J. A. Jensen, "Use of modulated excitation signals in medical ultrasound. Part I: basic concepts and expected benefits," *IEEE Transactions on Ultrasonics, Ferroelectrics, and Frequency Control*, vol. 52, no. 2, pp. 177–191, Feb. 2005.

[82] J. C. Curlander, R. N. McDonough, *Synthetic Aperture Radar System and Signal Processing*. New York: Wiley, 1991.

[83] M. Martone, "A multicarrier system based on the fractional Fourier transform for time-frequency-selective channels," *IEEE Transactions on Communications*, vol. 49, no. 6, pp. 1011–1020, Jun. 2001.

[84] H. Wang, X. Fan, Y. Chen, Y. Yang, "Wigner-Hough transform based on slice's entropy and its application to multi-LFM signal detection," *J. Syst. Eng.*, vol. 28, no. 4, pp. 634–642, 2017.

[85] X. Chen, J. Guan, Z. Bao, Y. He, "Detection and extraction of target with micromotion in spiky sea clutter via short-time fractional Fourier transform," *IEEE Transactions on Geoscience and Remote Sensing*, vol. 52, no. 2, pp. 1002–1018, 2014.

[86] X. Yu, X. Chen, Y. Huang, L. Zhang, J. Guan, Y. He, "Radar moving target detection in clutter background via adaptive dual-threshold sparse Fourier transform," *IEEE Access*, vol. 7, pp. 58 200–58 211, 2019.

[87] D. H. Lee, J. W. Shin, D. W. Do, S. M. Choi, H. N. Kim, "Robust LFM target detection in wideband sonar systems," *IEEE Transactions on Aerospace and Electronic Systems*, vol. 53, no. 5, pp. 2399–2412, 2017.

[88] A. W. Rihaczek, *Principles of high-resolution radar*, English. McGraw-Hill New York, 1969, xii, 498 p. ISBN: 0754321069.

[89] B. Porat, *Digital processing of random signals: Theory and methods*. Prentice-Hall, Inc., 1994, ISBN: 0130637513.

[90] L. He, K. He, L. Fan, X. Lei, A. Nallanathan, G. K. Karagiannidis, "Toward optimally efficient search with deep learning for large-scale mimo systems," *IEEE Transactions on Communications*, vol. 70, no. 5, pp. 3157–3168, 2022.

[91] K. He, L. He, L. Fan, X. Lei, Y. Deng, G. K. Karagiannidis, "Efficient memory-bounded optimal detection for GSM-MIMO systems," *IEEE Transactions on Communications*, vol. 70, no. 7, pp. 4359–4372, 2022.

[92] F. Engels, P. Heidenreich, A. M. Zoubir, F. K. Jondral, M. Wintermantel, "Advances in automotive radar: A framework on computationally efficient high-resolution frequency estimation," *IEEE Workshop on Multimedia Signal Processing*, vol. 34, no. 2, pp. 36–46, Mar. 2017.

[93] S. M. Patole, M. Torlak, D. Wang, M. Ali, "Automotive radars: A review of signal processing techniques," *IEEE Workshop on Multimedia Signal Processing*, vol. 34, no. 2, pp. 22–35, Mar. 2017.

[94] V. Namias, "The fractional order Fourier transform and its application to quantum mechanics," *IMA J. Appl. Math.*, vol. 25, pp. 241–265, 1980.

[95] A. C. McBride, F. H. Kerr, "On Namias's fractional Fourier transforms," *IMA J. Appl. Math.*, vol. 39, no. 2, pp. 159–175, 1987.

[96] H. M. Ozaktas, Z. Zalevski, M. A. Kutay, *The fractional Fourier transform with applications in optics and signal processing*. Wiley&Sons, 2001.

[97] J. Fonollosa, C. Nikias, "A new positive time-frequency distribution," in *Proc. IEEE Int. Conf. Acoust., Speech, Signal Process.*, 1994, IV/301–IV/304 vol.4.

[98] H. M. Ozaktas, D. Mendlovic, "Fractional Fourier optics," *Journal of the Optical Society of America A*, vol. 12, no. 4, pp. 743–751, 1995.

[99] I. Samil Yetik, A. Nehorai, "Beamforming using the fractional Fourier transform," *IEEE Transactions on Signal Processing*, vol. 51, no. 6, pp. 1663–1668, 2003.

[100] R. Tao, Y.-L. Li, Y. Wang, "Short-time fractional Fourier transform and its applications," *IEEE Transactions on Signal Processing*, vol. 58, no. 5, pp. 2568–2580, 2010.

[101] H. Ozaktas, O. Arikan, M. Kutay, G. Bozdagi, "Digital computation of the fractional Fourier transform," *IEEE Transactions on Signal Processing*, vol. 44, no. 9, pp. 2141–2150, 1996.

[102] L. Qi, R. Tao, S. Zhou, Y. Wang, "Detection and parameter estimation of multicomponent LFM signal based on the fractional Fourier transform," *Sci. China Inf. Sci*, vol. 47, pp. 184–198, 2004.

[103] A. Serbes, L. Durak-Ata, "Optimum signal and image recovery by the method of alternating projections in fractional Fourier domains," *Commun. Nonlinear Sci. Numer. Simul.*, vol. 15, pp. 675–689, 2010.

[104] O. Aldimashki, A. Serbes, "Performance of chirp parameter estimation in the fractional Fourier domains and an algorithm for fast chirp-rate estimation," *IEEE Transactions on Aerospace and Electronic Systems*, vol. 56, no. 5, pp. 3685–3700, 2020.

[105] L. Zheng, D. Shi, "Maximum amplitude method for estimating compact fractional Fourier domain," *IEEE Signal Processing Letters*, vol. 17, no. 3, pp. 293–296, 2010.

[106] A. Serbes, "On the estimation of LFM signal parameters: Analytical formulation," *IEEE Transactions on Aerospace and Electronic Systems*, vol. 54, no. 2, pp. 848–860, 2018.

[107] R. Tao, X. M. Li, Y. L. Li, Y. Wang, "Time-delay estimation of chirp signals in the fractional Fourier domain," *IEEE Transactions on Signal Processing*, vol. 57, no. 7, pp. 2852–2855, 2009.

[108] W. Wang, Y. Qiao, A. Yang, P. Guo, "A novel noise-insensitive chromatic dispersion estimation method based on fractional Fourier transform of LFM signals," *IEEE Photonics J.*, vol. 9, no. 1, pp. 1–12, 2017.

[109] X. Liu, B. Xiao, C. Wang, "Optimal target function for the fractional fourier transform of LFM signals," *Circuits, Syst. Signal Process.*, vol. 41, no. 7, pp. 4160–4173, 2022. DOI: 10.1007/s00034-022-01977-w.

[110] Z. Lu, S. Liu, J. Qiu, Q. Huang, C. Yang, "An efficient method for parameter estimation and separation of multi-component LFM signals," *Signal Process.*, vol. 207, p. 108 964, 2023. DOI: 10.1016/j.sigpro.2023.108964.

[111] S. S. Moghadasian, "A fast and accurate method for parameter estimation of multi-component LFM signals," *IEEE Signal Process. Lett.*, vol. 29, pp. 1719–1723, 2022. DOI: 10.1109/LSP.2022.3195118.

[112] B. Deng, R. Tao, C.-W. Qu, "Analysis of the shading between multicomponent chirp signals in the fractional Fourier domain," *Tien Tzu Hsueh Pao/Acta Electronica Sinica*, vol. 35, pp. 1094–1098, 2007.

[113] J. Song, Y. Wang, Y. Liu, "Iterative interpolation for parameter estimation of LFM signal based on fractional Fourier transform," *Circuits, Syst. Signal Processing*, vol. 32, pp. 1489–1499, 2013.

[114] A. Serbes, O. Aldimashki, "A fast and accurate chirp rate estimation algorithm based on the fractional Fourier transform," in *Proc. 25th Eur. Signal Processing Conf. (EUSIPCO)*, 2017, pp. 1105–1109.

[115] B. Ristic, B. Boashash, "Comments on "the Cramer-Rao lower bound for signals with constant amplitude and polynomial phase," *IEEE Transactions on Signal Processing*, vol. 46, no. 6, pp. 1708–1709, 1998.

[116] S. Peleg, B. Porat, "The Cramer-Rao lower bound for signals with constant amplitude and polynomial phase," *IEEE Transactions on Signal Processing*, vol. 39, pp. 749–752, Mar. 1991.

[117] C. C. Y. Rzhanov, L. Linett, "The analysis of multiple linear chirp signals," Proc. IEE Symposium on Time-Scale, Time-Frequency Analysis, and Applications, vol. 4, Feb. 2000, pp. 1–7.

[118] C. Capus, K. Brown, "Fractional Fourier transform of the Gaussian and fractional domain signal support," *IEE Proc. Vis. Image Signal Processing*, vol. 150, no. 2, pp. 99–106, Apr. 2003.

[119] S. M. Kay, *Fundamentals of statistical signal processing: Estimation theory*. Prentice Hall, 1997.

[120] B. Porat, *Digital Processing of Random Signals: Theory and Methods*. New Jersey: Prentice-Hall, 1993, pp. 421–428.

[121] K. H. Lloyd, "On the implementation of noise in the discrete simulation of continuous systems," *Tech. Rep. (DTIC Document)*, 1982.

[122] W. Cheney, D. Kincaid, *Numerical Mathematics and Computing*, 3rd ed. Brooks/Cole Publishing Company, 1994.

[123] W. Cheney, D. Kincaid, *Numerical Mathematics and Computing*, 3rd ed. Brooks: Cole Publishing Company, 1994.

[124] E. Aboutanios, B. Mulgrew, "Iterative frequency estimation by interpolation on Fourier coefficients," *IEEE Transactions on Signal Processing*, vol. 53, no. 4, pp. 1237–1242, 2005.

[125] A. Serbes, "Fast and efficient sinusoidal frequency estimation by using the DFT coefficients," *IEEE Transactions on Communications*, vol. 67, no. 3, pp. 2333–2342, 2019.

[126] I. Djurović, M. Simeunović, P. Wang, "Cubic phase function: A simple solution to polynomial phase signal analysis," *Signal Processing*, vol. 135, pp. 48–66, 2017.

[127] I. S. Gradshteyn, I. M. Ryzhik, *Table of integrals, series, and products*, Seventh. Elsevier/Academic Press, 2007, pp. xlviii+1171.

[128] H. Vazquez-Leal, R. Castañeda-Sheissa, U. Filobello-Nino, A. Sarmiento-Reyes, J. Sanchez-Orea, "High accurate simple approximation of normal distribution integral," *Mathematical Problems in Engineering*, vol. 2012, 2012.

[129] M. Abramowitz, I. A. Stegun, *Handbook of Mathematical Functions with Formulas, Graphs, and Mathematical Tables*, ninth. Dover, 1964.

[130] O. Aldimashki, A. Serbes, "LFM signal parameter estimation in the fractional Fourier domains: Analytical models and a high-performance algorithm," *Signal Processing*, vol. 214, p. 109 224, 2024, ISSN: 0165-1684. DOI: doi.org/10.1016/j.sigpro.2023.109224.

[131] C. M. Bishop, *Pattern Recognition and Machine Learning (Information Science and Statistics)*. Springer, 2007.

[132] J. Nocedal, S. J. Wright, *Numerical Optimization*, 2e. New York, NY, USA: Springer, 2006.

PUBLICATIONS FROM THE THESIS

Contact Information: aserbes@yildiz.edu.tr, omair@dleaf.com

Papers

1. O. Aldimashki, A. Serbes, "Performance of chirp parameter estimation in the fractional Fourier domains and an algorithm for fast chirp-rate estimation", *IEEE Transactions on Aerospace and Electronic Systems*, vol. 56, no. 5, pp. 3685-3700, Oct. 2020, doi: 10.1109/TAES.2020.2981268.

2. O. Aldimashki, A. Serbes, “LFM signal parameter estimation in the fractional Fourier domains: Analytical models and a high-performance algorithm,” *Signal Processing*, vol. 214, p. 109 224, 2024, ISSN: 0165-1684. DOI: doi.org/10.1016/j.sigpro.2023.109224.

Conference Papers

1. A. Serbes, O. Aldimashki, "A fast and accurate chirp rate estimation algorithm based on the fractional Fourier transform," *2017 25th European Signal Processing Conference (EUSIPCO)*, Kos, Greece, 2017, pp. 1105-1109, doi: 10.23919/EUSIPCO.2017.8081379.